Federal University of São Carlos
Center for Exact Sciences and Technology
Department of Physics
Physics Graduate Program
Superconductivity and Magnetism Group

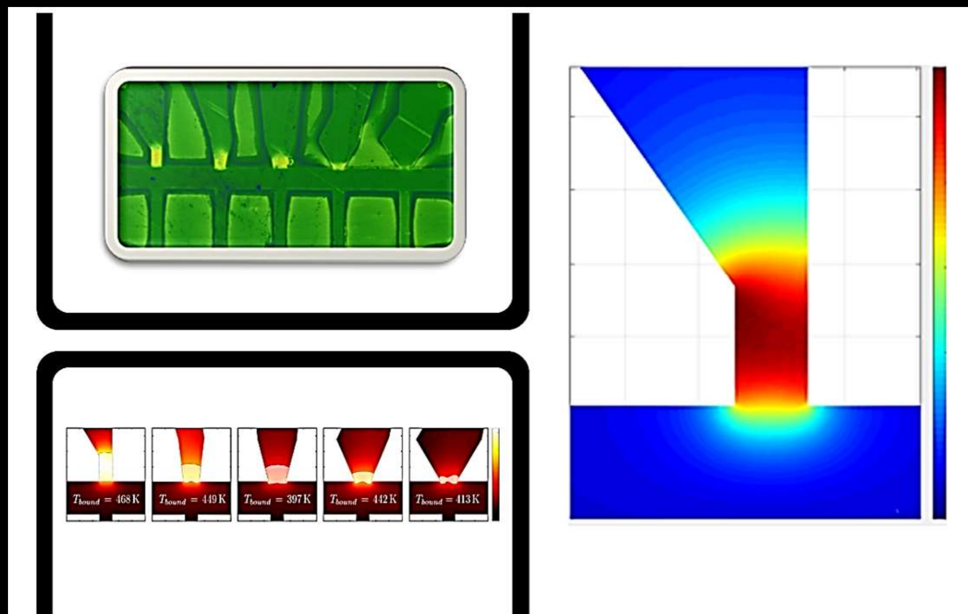

Electromigration of multiterminal transport bridges

Elijah Anertey Abbey

São Carlos, SP, Brazil
2023

Federal University of São Carlos - UFSCar
Center for Exact Sciences and Technology - CCET
Department of Physics - DF
Physics Graduate Program - PPGF
Superconductivity and Magnetism Group - GSM

Electromigration of multiterminal transport bridges

Eletromigração de pontes de transporte multiterminal

Elijah Anertey Abbey

São Carlos, SP, Brazil
2023

Elijah Anertey Abbey

Electromigration of multiterminal transport bridges

Eletromigração de pontes de transporte multiterminal

Thesis presented to the Graduate Program in Physics at the Federal University of São Carlos, as part of the requirements for obtaining the degree of Doctor of Science with emphasis in Physics.

Tese apresentada ao Programa de Pós-Graduação em Física da Universidade Federal de São Carlos, como parte das exigências para a obtenção do título de Doutor em Ciências com ênfase em Física.

Advisor/Orientador: Prof. Dr. Maycon Motta
Co-Advisor/Co-orientador: Prof. Dr. Wilson Aires Ortiz
Co-Advisor Abroad: Prof. Dr. Alejandro V. Silhanek

São Carlos, SP, Brazil
2023

Abbey, Elijah Anertey

Electromigration of multiterminal transport bridges /
Elijah Anertey Abbey -- 2023.
120f.

Tese de Doutorado - Universidade Federal de São Carlos,
campus São Carlos, São Carlos
Orientador (a): Maycon Motta
Banca Examinadora: Maycon Motta, Pedro Schio de
Noronha Muniz, Rafael Zadorosny, Alexandre José
Gualdi, Danusa do Carmo
Bibliografia

1. Electromigration. 2. Electrical properties. 3. Finite-
element method. I. Abbey, Elijah Anertey. II. Título.

Ficha catalográfica desenvolvida pela Secretaria Geral de Informática
(SIn)

DADOS FORNECIDOS PELO AUTOR

Bibliotecário responsável: Ronildo Santos Prado - CRB/8 7325

UNIVERSIDADE FEDERAL DE SÃO CARLOS

Centro de Ciências Exatas e de Tecnologia
Programa de Pós-Graduação em Física

Folha de Aprovação

Defesa de Tese de Doutorado do candidato Elijah Anertey Abbey, realizada em 09/03/2023.

Comissão Julgadora:

Prof. Dr. Maycon Motta (UFSCar)

Prof. Dr. Pedro Schio de Noronha Muniz (CNPEM)

Prof. Dr. Rafael Zadorosny (UNESP)

Prof. Dr. Alexandre José Gualdi (UFSCar)

Profa. Dra. Danusa do Carmo (CNPEM)

O Relatório de Defesa assinado pelos membros da Comissão Julgadora encontra-se arquivado junto ao Programa de Pós-Graduação em Física.

In loving memory of my father, Mankata Aban Abbey

A beloved husband, father, and friend

Gone but never forgotten.

Acknowledgments

The success of my thesis has been largely due to the dedicated work and efforts of many individuals, and as such, as with all research that culminates in a thesis of any kind, it is necessary to acknowledge every unsung hero who contributed in some way to its success.

To begin with, I would like to express my sincere gratitude to my supervisors, Prof. Dr. Maycon Motta and Prof. Dr. Wilson Aires Ortiz, for their invaluable advice, continuous support, and patience throughout my PhD research. Their vast expertise and wealth of experience have inspired me throughout my academic studies and daily life.

I would like to extend my deepest gratitude to Prof. Dr. Alejandro V. Silhanek for welcoming me to the EPNM (Experimental Physics of Nanostructured Materials), University of Liège, and for allowing me to pursue my research during my doctoral sandwich program, which provided me with the research data necessary to develop this thesis. He gave me the chance to enter the vast world of electromigration. For all this, I am very grateful to him and thank him sincerely. It is also important that I extend my appreciation to the members of EPNM, starting work in a new setting is always challenging, which is why I would like to express my gratitude to Stefan Marinković for his patience while training me, as well as Simon Collienne for his support.

I extend my sincere thanks to my friends and colleagues in the GSM (Superconductivity and Magnetism Group): Lincoln Pinheiro, Davi Chaves and Italo Moreira. Thank you Lincoln, for everything you taught me during our long periods of dedication to the experimental works at the GSM.

I am grateful for the unending support from my family, especially my mother, Mary Ofoley Yarboi. You have always stood behind me, and this was no exception. I appreciate you taking the time to call me numerous times, for calming me down, and for continually reminding me of the goal. Thank you to my sister, Ruth Queeny Abbey, for always being there for me and providing assistance and support during my years of study. I would like to thank my brothers, Nunya and Mawunyega, for serving as an endless source of inspiration.

Above all, I want to thank my wife, Diléia Aparecida Martins, who has been incredibly supportive of me and made several sacrifices to help me reach to this point. Most of all, I want to thank you for being my best friend. Together with her, I want to thank my son, Elliot Nii Abe Abbey, who has given me more strength, happiness, and fulfillment than I could have ever dreamed. To the moon and back, I adore you.

Without the constant encouragement of my pals, Adamu, Ebenezer, Stephen, Solomon, and Patrick, I would never have progressed this far. I appreciate everything. A very special thanks goes to Lloyd; I am fortunate to have a trustworthy friend like you.

This work was made possible thanks to the support of the Coordenação de Aperfeiçoamento de Pessoal de Nível Superior, Brazil (CAPES), Finance Code 001, which provided funding for the scholarship, as well as the Sandwich PhD Program Abroad (PDSE), Grant No. 88881.624496/2021-01.

Abstract

With the continued miniaturization of integrated circuits (ICs), the case of metallic tracks subjected to stress caused by transport currents has become a matter of increasing concern, as it puts at risk the reliability of electronic devices. Because they are minuscule, on-chip interconnects in ICs are extremely prone to Electromigration (EM), which is a well-known cause of failure in semiconductor ICs, and through time, researchers have discovered ways to first control the wearout issue and then ultimately master it. However, the EM control reliability scenario is significantly changing in the current interconnect technologies, and a number of important issues need to be addressed.

This work is devoted to the investigation of current-induced modifications in micro-scale junctions and constrictions of superconducting and metallic materials.

In the first part of our experimental results, we investigate the targeted and localized material modifications produced by electropulsing on Al capped Nb microbridges with multiterminal configuration. The affected regions on the Nb/Al bilayer terminals are revealed by an in-lens secondary electrons detector in a scanning electron microscope as well as by Kelvin-probe Force Microscopy, both suggesting a decrease of the work function in the modified areas. In contrast to that, the affected areas are neither apparent through an Everhart-Thornley secondary electrons detector nor through Atomic Force Microscopy, which indicates little morphological changes on the microstructure. In addition, we demonstrate that the extension of the electroannealed regions is strongly influenced by the terminal geometry. These results are captured by complementary finite element modelling which permits us to estimate a threshold temperature of (435 ± 35) K needed to induce material modifications. These findings provide further insights on the subtle modifications produced by gentle electroannealing of Nb/Al microstructures and represent a step forward towards mastering this emerging nanofabrication technique.

In the last experimental chapter of this thesis, we report on results concerning the structural modification of Al and Ni microconstrictions induced by elecropulsing by monitoring the resistance of the constrictions during EM in order to prevent permanent damages and preserve the junction for multiple trials. We applied current pulses to locally change the physical properties of the constrictions. Scanning Electron Microscopy inspection showed that the voids and hillocks found in EM of Al are noticeably missing in EM of Ni. The EM process in Ni occurs in a fairly well defined area, as one could predict in view of the occurrence of current crowding and local heating. EM in Al, on the other hand, appears to occur more randomly, possibly due to less transparent grain boundaries.

Keywords: electromigration, superconductivity, electropulses, scanning electron microscope, atomic force microscope, Kelvin probe force microscope.

Resumo

Com a contínua miniaturização de circuitos integrados (CIs), o caso de trilhas metálicas submetidas a estresse causado por correntes de transporte tornou-se motivo de crescente preocupação, pois coloca em risco a confiabilidade de dispositivos eletrônicos. Por serem minúsculas, as interconexões em CIs são extremamente propensas à eletromigração (EM), que é uma causa bem conhecida de falha em CIs de semicondutores e, ao longo do tempo, foram descobertas maneiras de controlar esse problema de desgaste e, em último caso, dominá-lo. No entanto, o cenário de confiabilidade no controle de EM tem mudado significativamente nas tecnologias de interconexão atuais e várias questões importantes precisam ser abordadas.

Este trabalho é dedicado à investigação de modificações induzidas por corrente em junções e constrições em escala microscópica de materiais supercondutores e metálicos.

Na primeira parte de nossos resultados experimentais, investigamos as modificações de material direcionadas e localizadas produzidas por eletropulsação em micropontes de Nb revestidas com Al com configuração multiterminal. As regiões afetadas nos terminais da bicamada de Nb/Al são reveladas por um detector de elétrons secundários do tipo *in-lens* em um microscópio eletrônico de varredura, bem como por Microscopia de Força por Sonda Kelvin, ambos sugerindo uma diminuição da função de trabalho nas áreas modificadas. Por outro lado, as áreas afetadas não são aparentes por um detector de elétrons secundários do tipo Everhart-Thornley nem por Microscopia de Força Atômica, o que indica poucas mudanças morfológicas na microestrutura. Além disso, demonstramos que a extensão das regiões recozidas pelo aquecimento devido às correntes é fortemente influenciada pela geometria dos terminais. Esses resultados são amparados por modelagem complementar, baseada em elementos finitos, que nos permite estimar uma temperatura limite de (435 ± 35) K necessária para induzir modificações no material. Essas descobertas fornecem mais informações sobre as modificações sutis produzidas pelo recozimento suave de microestruturas de Nb/Al e representam um passo à frente para dominar essa técnica emergente de nanofabricação.

No último capítulo desta tese, relatamos resultados relativos à modificação estrutural de microconstrições de Al e Ni induzidas por eletropulsação, monitorando a resistência das constrições durante EM, a fim de evitar danos permanentes e preservar a junção para múltiplas corridas. Para isso, aplicamos pulsos de corrente para alterar localmente as propriedades físicas das constrições. A inspeção via Microscopia Eletrônica de Varredura mostrou que os vazios e montes encontrados em razão de EM em amostras de Al estão visivelmente ausentes nos dispositivos de Ni. O processo de EM no Ni ocorre em uma área razoavelmente bem definida, como era previsível, em vista da ocorrência de aglomerações de corrente e pelo aquecimento local. EM em Al, por outro lado, parece ocorrer de forma mais aleatória, possivelmente devido ao fato de que os contornos de grão são menos transparentes.

Palavras-chave: eletromigração, supercondutividade, eletropulsos, microscopia eletrônica de varredura, microscópio de força atômica, microscopia Kelvin.

List of Figures

2.1 Basic properties of the superconducting state 26
2.2 Vortex structure. 27
2.3 The interface between normal and superconducting states for type-I and type-II superconductors. 28
2.4 Various types of structures where the Josephson effect can take place. . . . 29
2.5 Schematic representation of a Josephson junction. 30
2.6 Modulation of critical current with magnetic flux (Fraunhofer pattern) in a short Josephson junction. 34

3.1 Portion of crystalline lattice exhibiting defects: atom vacancies, interstitial impurities and grain boundaries. 37
3.2 Forces acting on an atom in an EM process. 39
3.3 Formation of hillocks and voids in a polycrystalline line of metal. 39
3.4 Atomic diffusion in solids: interaction of different causes. 44
3.5 The effect of junction width on EM compared to average grain size. 49
3.6 Characteristic of a uncontrolled EM. 50

4.1 Overview of the investigated sample. 53
4.2 Schematic of the triple constriction. 54
4.3 Process flow of the e-beam lithographic procedure. 57
4.4 Scalable fabrication of constrictions based on regular metal layer (lift-off) and by stepping-up contacts for wire bonding via lift-off. Scale bar: 500 μm. 59
4.5 Scalable fabrication of constrictions based on nanoholey layers. 60
4.6 Scalable fabrication of constrictions based on nanoholey Al layers by dry etching followed by photolithography and lift-off to step up the contacts for wire bonding. 61
4.7 Diagram showing the major components of the SEM as well as an illustration of the sample-electron beam interaction during SEM experiment. 63
4.8 Overview of the main parts of the system of the EPNM facility at ULiège . 65
4.9 Overview of the main parts of the experimental setup for EM 67
4.10 Sample holder and bonding platform. 68
4.11 Measurement protocol for controlled electromigration. 69
4.12 Graphical User Interface for EM experiments. 69

5.1 SEM image of a Nb multiterminal transport bridges. 73
5.2 AFM image showing cross-sectional profile of junction 1. 74
5.3 Resistance measured during and after current pulses. 76
5.4 AFM inspection carried out after electropulsing. 77
5.5 Microscopy inspection of a Nb/Al device after the electropulsing procedure shown in Figure 5.3. 78
5.6 Comparison between measured resistance during electropulsing and simulation with and without thermal resistance. 80

5.7 Simulation results for the five junctions of the same sample. 81
5.8 R(T) curves for the addressed junctions. 82
5.9 Critical current versus magnetic field applied perpendicular to the plane of the film at a temperature of 1.8K. 83
5.10 SEM and KPFM images for Device B 84

6.1 Sample layout and measurement protocol. 89
6.2 Evolution of R_{max} and R_{min} as a function of I_{PLS} 90
6.3 Estimation of the temperature at the constriction. 91
6.4 High-resolution SEM images of electropulsed sample. 92
6.5 SEM images of the Ni sample investigated. 95
6.6 AFM and MFM images of the Ni device post EM. 96
6.7 Mesh and current boundary conditions used for FEM modelling. 99
6.8 Simulated current density and temperature distribution of Ni sample for an applied field 26 mA. 100
6.9 Formation of nanogap. 101
6.10 The resistance-current characteristic curves for SEM image depicted in Figure 6.9 102

A.1 SEM images of constrictions based on Nanoholey Al layer generated by photolithography and wet etching. 118
A.2 SEM images of before (a) and after electromigration captured with inlens (b) and Everhart-Thonley (c) lens. 119
A.3 The evolution of resistance as a function of current during the electromigration process is recorded for all EM runs. 120

List of Tables

3.1 Activation energies for different diffusion in different metals 48

4.1 Summary of the fabrication for triple constriction patterning. 62

List of symbols

Roman

A magnetic vector potential
B magnetic induction
C concentration of vacancies
D_a diffusion coefficient
D diffusion constant
E (applied) electric field
E_a activation energy
e electron charge
e^* condensed electron charge
f_n normal free energy density
h Planck constant
$\hbar$ reduced Planck constant
H magnetic field
H_c thermodynamic critical field
H_{c1} first critical field
H_{c2} second critical field
H_{c3} third critical field
I electromigration current
I_{EM} electric current
I_c critical current
J current density
J_c critical current density
k_B Boltzmann constant
L length
m^* condensed electron mass
n density of charge electrons
n_n normal electrons density
n_s superconducting electrons density
P power
q^* effective charge

Greek

α thermal coefficient
Θ_m mass flux
Θ_v vacancy flux
$\Delta\Phi$ work function
κ Ginzburg-Landau parameter
λ penetration depth
ξ coherence length
ρ resistivity
σ conductivity
σ_{ns} surface energy at normal-superconducting
γ heat transfer coefficient
φ superconducting phase
Φ_B magnetic flux
Φ_0 magnetic flux quantum
μ_0 permeability of free space
ψ wavefunction

t thickness

T temperature

T_c critical temperature

V voltage

w width

Z^* effective valence

List of Acronyms

E_a	activation energy
T_c	critical temperature
AFM	atomic force microscopy
Al	Aluminum
BCS	Bardeen-Cooper-Schrieffer
BSE	Backscattered electrons
CD	critical dimension
DC	Direct Current
DIW	deionized water
EBL	electron beam lithography
EM	Electromigration
ESD	electrostatic discharge
ET	Everhart-Thornley
EXAFS	Extended X-ray absorption fine structure
GL	Ginzburg-Landau
HMDS	hexamethyldisilazane
IC	Integrated Circuits
IPA	isopropyl alcohol
KPFM	Kelvin-probe force microscopy
MFM	Magnetic Force Microscopy
MIBK	methyl isobutyl ketone
Nb	Niobium
Ni	Nickel
NMP	1-Methyl-2-pyrrolidone
PCB	printed circuit board

PMMA	polymethyl metacrylate
PMMA/MA	copolymer methyl metacrylate
PVD	physical vapor deposition
SE	Secondary electrons
SEM	Scanning Electron Microscope
SPM	scanning probe microscopy
TEM	Transmission Electron Microscopy
TM	Thermal migration

Contents

1 Introduction **20**

2 Superconductivity **23**
- 2.1 Discovery of Superconductivity . . . 24
- 2.2 Superconducting State . . . 25
  - 2.2.1 Surface energy in Type-I and Type-II Superconductors . . . 26
- 2.3 Weak links and Josephson Effect . . . 28
  - 2.3.1 Josephson effect . . . 30
  - 2.3.2 Junction under a magnetic field . . . 33

3 Electromigration in metals **35**
- 3.1 Introduction . . . 36
- 3.2 Electromigration: Physical Background . . . 37
  - 3.2.1 Mass flux . . . 39
  - 3.2.2 Empirical point of view : Black's model . . . 42
- 3.3 Mechanisms related to atomic diffusion . . . 43
  - 3.3.1 Chemical diffusion . . . 44
  - 3.3.2 Stress migration . . . 44
  - 3.3.3 Thermal migration . . . 45
  - 3.3.4 The resultant diffusion flux . . . 47
- 3.4 Effects of microstructure . . . 48
- 3.5 Electromigration control process . . . 49

4 Experimental techniques **52**
- 4.1 Sample layout . . . 53
- 4.2 The art of lithography . . . 55
  - 4.2.1 Electron Beam Lithography . . . 55
  - 4.2.2 Photolithography . . . 55
- 4.3 Fabrication processes . . . 56
  - 4.3.1 Nb multiterminal . . . 56
  - 4.3.2 Al and Ni constriction (plain layers) . . . 57
  - 4.3.3 Al constriction fabricated on nanoholey layers . . . 59
- 4.4 Imaging and sample characterization . . . 62
  - 4.4.1 Scanning Electron Microscopy . . . 62
  - 4.4.2 Atomic Force Microscopy . . . 64
  - 4.4.3 Kelvin Probe Force Microscopy . . . 65
- 4.5 Experimental Electromigration Set-up . . . 66
  - 4.5.1 Sample Handling . . . 67
  - 4.5.2 Controlled Electromigration Software . . . 68

5 Current-induced modifications of superconducting Nb multiterminal transport bridges **71**
5.1 Introduction . . . 72
5.2 Sample and experimental details . . . 73
5.3 Electropulsing protocol and methodology . . . 75
5.4 Visualization of the induced junction's modification . . . 76
5.5 Finite element modelling . . . 78
5.6 Superconducting properties after electropulsing . . . 82
5.7 Reproducibility: KPFM and SEM . . . 84
5.8 Conclusions . . . 85

6 Structural modifications of Al and Ni multiterminal bridges **86**
6.1 Introduction . . . 87
6.2 Experimental details . . . 88
6.3 Electromigration properties . . . 89
6.4 Microstructural effects due to EM . . . 92
6.4.1 Finite element modelling of the temperature distribution . . . 99
6.5 Nanogap formation . . . 101
6.6 Conclusions . . . 102

7 Conclusions and perspectives **104**

Bibliography **106**

Appendix A **118**
A.1 Modification of nanoholey Al films by electropulsing . . . 118
A.2 Post electropulsing . . . 119

Chapter 1

Introduction

As Integrated Circuits (IC) continue to be miniaturized, the relevance of metallic structures under current stress becomes a major source of concern for the reliability of electronic devices. A number of notable aspects fall into this category. To begin with, the problem is related to the appearance of voids and other material defects that arise on operational devices after they have been in operation for a period of several days, weeks, or months. In addition, there are concerns regarding the presumed integrity of the interconnects at the atomic level. The mechanisms underlying these concerns are not new. It is a fact that these potential problems have always existed in these devices, however, the IC designs implemented using earlier technologies were comparatively robust for these unpredictable defects generated. According to current and planned IC structure scales, material defects can result in dramatic damage or change in resistance, leading to failure and/or incorrect operation of the IC.

Throughout the history of microelectronics, defects in metallic interconnects have been attributed to electromigration (EM), the phenomenon of current-induced atomic migration in solids. This is partly due to the huge current densities that can eventually lead to atomic depletion at certain sites in the metal. These high current densities produce a lot of scattered electrons which act like a breeze on the ions, causing them to drift in the structure. In such context, EM is a well-known cause of failure in semiconductor integrated circuits, and over the years, researchers have discovered ways to first control the wearout issue and then ultimately master it.

It has been proven that the use of different materials, especially their hybrids, as well as their reduction in size, together with technological adaptations, dramatically impacts chip characteristics. Among many other things, the advent of nanotechnology strongly

impacted numerous fields of research, and superconductors as well as magnetic materials were no exception. In recent times, quantum computation based on superconducting electronic circuits has emerged as a serious contender to replace current electronics due to the fact that systems based on qubits significantly enhance processing capacity.

In view of the growing scientific and economic role of nanoscale metal structures subjected to electric current, in this thesis we present a number of studies aimed at improving our understanding of the EM phenomenon in metals such as Nb, Al, and Ni. Since two of them are superconductors and thus candidates for nanoscale devices, e.g., superconducting qubits, this manuscript introduces aspects of both superconductivity and EM that are relevant to the thesis as a whole. The first part of this work is to determine, in multiterminal Nb bridges, the influence of the junction geometry on the extension of the area affected by EM. To that end, we resort to several microscopy inspection techniques, including atomic force microscopy (AFM), scanning electron microscopy (SEM), and Kelvin probe force microscopy (KPFM). The second part is to electromigrate two independent samples, one of Al and the other of Ni, with identical geometries and layouts and capture with SEM, AFM, and Magnetic Force Microscopy (MFM), their responses to EM.

The thesis is organized as follows:

In **Chapter** 2, a concise overview of fundamental principles of superconductivity is provided, followed by an explanation of some aspects related to weak-link physics. Additionally, a model of Josephson junctions is introduced, and its characteristics and limits are discussed.

Chapter 3 introduces the theoretical background of atomic migration under an electron wind, commonly known as EM. In this chapter, we illustrate the physics of the process and explain its triggering factors. The next step is to focus on how it is possible to control this phenomenon through the use of current pulses.

The **Chapter 4** of this thesis describes some of the experimental aspects and the development of this research. We describe the necessary tools for lithography and visualization as well as how EM was implemented at the probe station. Controlled EM and the software that enables it are also described.

Chapter 5 presents the results of EM on niobium multiterminal with different angles and demonstrate that this inherently stochastic phenomenon is controlled to a high level, enabling us to modify the material properties accordingly. The affected regions on the terminals are revealed by an in-lens secondary electrons detector in a scanning electron microscope as well as by Kelvin-probe force microscopy, both suggesting a decrease of the

work function in the modified areas. The changes are interpreted to be the result of the high temperatures at the junctions. Model simulations are also presented to demonstrate good agreement with experimental results.

Chapter 6 presents the preliminary results of structural modifications of Al and Ni microconstrictions induced by electropulsing. SEM images of Al after electropulsing demonstrate that voids had formed on the cathode side of the constriction. Additionally, hillocks were also formed at the end of the bridge and near certain voids. This portion of the bridge is very significant with respect to the temperature gradient. SEM images of Ni, however, show an annealing effect, which differs from the classical effect of EM, i.e., grain-boundary diffusion, stress gradients, and void formation. This is supported by the observation from the numerical simulations that the temperature rise is not uniform between the voltage contacts.

Chapter 7 finalizes this thesis by presenting the key findings and conclusions. It offers an overview of the research outcomes and their implications. Additionally, this chapter provides a perspective of upcoming experimental studies planned at GSM-UFSCar*.

*Grupo de Supercondutividade e Magnetismo - Universidade Federal de São Carlos

Chapter 2

Superconductivity

Considering that we investigated the superconducting characteristics of Nb in Chapter 5, this chapter seeks to give the reader with an overview of basic principles in the field of superconductivity. To comprehend the superconductive state, it is required to quickly describe the two most important aspects: the absence of electric resistance and the exceptional diamagnetic reaction. We also go through the ideas of critical temperature, critical current density, and critical magnetic field. The introduction of weak link and Josephson effect concludes the section on superconductivity.

2.1 Discovery of Superconductivity

The study and application of superconducting materials in the most diverse areas of knowledge have demonstrated their significant potential impact on society [1]. It goes without saying that superconductivity is considered one of the most revolutionary scientific discoveries of the 20th century [2]. It has a unique property that causes certain materials, at specific temperatures, to lose all resistance to the flow of electricity. Considering the property of zero resistance, one might imagine that if we were to feed current through a superconducting loop, it would continue to flow for eternity. This zero resistance regime allows a range of innovative technological applications. The discovery of superconductivity and its unique property of zero resistance owes its origins to the pioneering work of Heike Kamerling Onnes in the field of cryogenic systems and low temperature physics, which paved the way for the study and application of these materials.

Heike Kamerling Onnes, who worked in Leiden (The Netherlands) with cryogenic systems, liquefied helium in 1908, achieving temperatures as low as 3 K and opening a novel chapter in low temperature physics. Following the successful realization of this goal, the next stage required developing control apparatuses which provided the essential tools for studying materials at low temperatures. After three years, in 1911, he and his team investigated the effect of impurities on the electrical resistance of metals at low temperatures [3]. They found that the resistivity of pure mercury suddenly decreased by more than four orders of magnitude in a narrow temperature range around 4.2 K, which was called the critical temperature (T_c). A fascinating property of this material, *perfect conductivity*, has been recognized as being useful for applications such as coils used to generate high magnetic fields [4]. Two decades later, in 1933, Walter Meissner and Robert Ochsenfeld observed another striking characteristic of superconducting materials. Lead and tin cylinders encased in an external magnetic field excluded magnetic flux below their T_c of 7.2 K and 3.7 K, respectively, regardless of their magnetic history, i.e., regardless of whether they were first cooled and then exposed to a magnetic field or vice-versa [5, 6]. The phenomenon was originally called *perfect diamagnetism* or Meissner-Ochsenfeld effect, but it is nowadays called Meissner effect.

2.2 Superconducting State

Following these discoveries, it was established that, below a certain T_c, some materials experience a transition into the superconducting state, which is characterized by two distinctive properties. Firstly, zero resistivity (perfect conductivity), i.e., when resistance falls to zero, a current is able to run through the material without any form of dissipation of energy. However, when submitted to a current higher than the critical current density, J_c, the superconducting state disappears. Secondly, the superconductor exhibits another property in addition to the perfect conductivity. It expels the magnetic field from its interior, which is known as the Meissner effect [5]. Based on their magnetic characteristics, superconductors are classified two types.

Type-I superconductors completely expel magnetic flux until some critical field H_c, showing perfect diamagnetism. The superconducting state gets destroyed above this field and the resistivity state is restored allowing the applied field to penetrate the material. The perfect diamagnetism occurs due to the screening currents near the surface that produces a magnetization to cancel the magnetic induction inside the material when it is in an applied magnetic field. However since the surface current cannot be infinitely large, the magnetic field does penetrates a bit into the superconductor but eventually falls off exponentially with a characteristic length known as the penetration depth λ, proposed by the London brothers [7]. The magnetic flux density inside the sample can be expressed as

$$\vec{B}(x) = \vec{B}_0 e^{-x/\lambda} \tag{2.1}$$

where $\vec{B}_0$ is the value of the magnetic field at the surface and x is the distance from the surface to some interior point.

For type-II superconductors, there exist two critical fields, the lower critical field (H_{c1}) and the upper critical field (H_{c2}). For fields less than H_{c1}, it behaves like a Type-I superconductor below H_c. For fields above H_{c1} the flux partially penetrates into the material until H_{c2} is reached. Above H_{c2} the material returns to the normal state as depicted in Figure 2.1. Between H_{c1} and H_{c2} the material is said to be in the **mixed state** decribed by Abrikosov [8]. This state is also called **vortex state**, since the magnetic flux that partially penetrates the superconductor is quantized in the form of "vortices", each

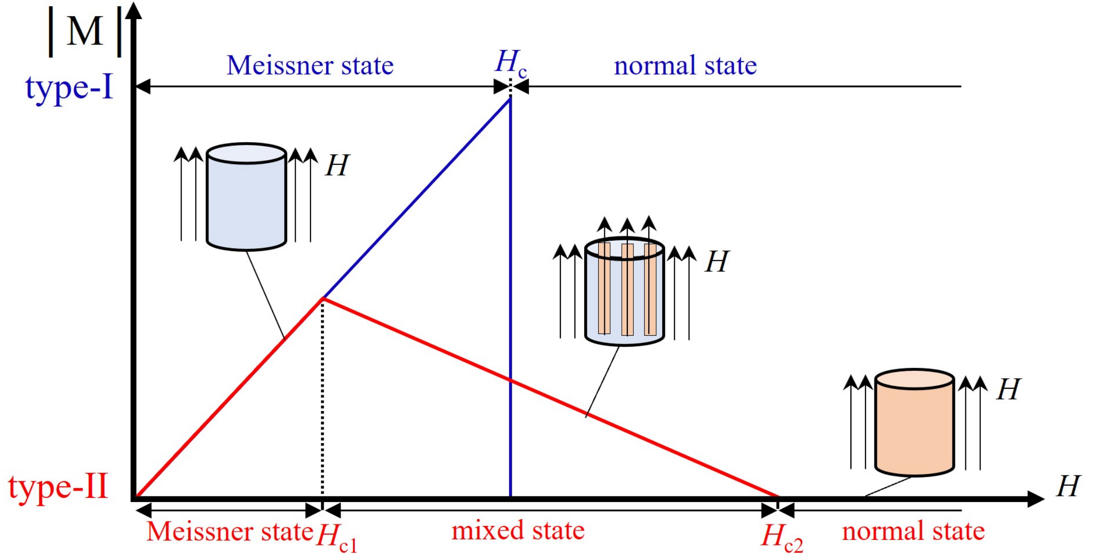

Figure 2.1: **Basic properties of the superconducting state.** Magnetization M of a superconductor as a function of the applied magnetic field H, illustrating the fundamental difference in behavior between type-I and type-II superconductors. While superconductivity disappears suddenly at the critical field H_c in type-I superconductors, it survives between the lower and upper critical fields, H_{c1} and H_{c2}, in type-II superconductors, where field is allowed inside the superconductor. The insets represent, from left to right, the Meissner state, the mixed state and the normal state. Superconducting regions are colored in blue, while normal regions are in orange.

carrying one quantum of magnetic flux

$$\Phi_0 = \frac{h}{2e} = 2.07 \times 10^{-15}\,\text{Weber}, \tag{2.2}$$

where h is the Planck constant and e is the charge of the electron. The vortex can be described as a cylinder of diameter 2ξ, where ξ is the coherence length related to the typical size of the Cooper pairs*, having concentric superconducting currents that shield the field in a radius λ as shown in Figure 2.2.

2.2.1 Surface energy in Type-I and Type-II Superconductors

Considering the well-known Ginzburg-Landau (GL) theory [11], one can estimate the sign of the surface energy σ_{ns} associated with the interface between normal and superconducting regions. It allows us to differentiate between Type-I and Type-II superconductors. Then one can obtain the surface energy based on the difference between the Gibbs free energy per unit area of a homogeneous phase (normal or superconducting) and a mixed

*As described by Bardeen, Cooper and Schrieffer [9], who proposed the Bardeen-Cooper-Schrieffer (BCS) theory, the electrons mediated by phonons condense in pairs to form the so-called Cooper pairs during the transition to the superconducting state.

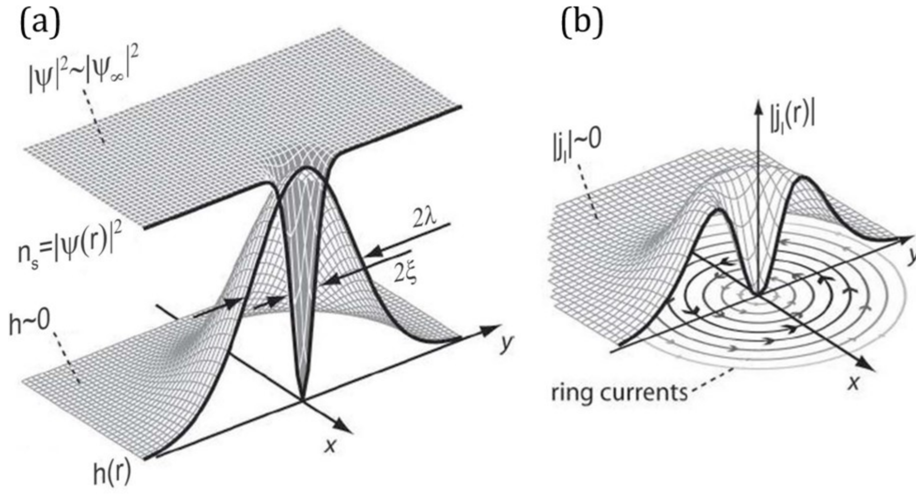

Figure 2.2: **Vortex structure.** (a) Local magnetic field and density of superconducting electrons distributions around the normal core. (b) The superconducting currents around the center of the vortex as a function of the radial distance r. Figure adapted from [10].

phase (where superconductivity is still incompletely established, $\mathbf{B} \neq 0$)[12]. As a result, the surface energy is:

$$\sigma_{\text{ns}} \approx (\xi - \lambda)\frac{\mu_0 H_c^2}{2} \tag{2.3}$$

where H_c is the critical magnetic field.

It should be noted that, if $\sigma_{\text{ns}} > 0$, then creating such interfaces is energetically unfavorable and the material is a type-I superconductor. In the event that, $\sigma_{\text{ns}} < 0$ the state of lower energy corresponds to the situation in which some normal regions where flux has penetrated are allowed within the superconductor (formation of normal regions with magnetic flux within the superconducting state). In practice, the boundary between these two regimes is assessed by computing the Ginzburg-Landau parameter, i.e., the ratio of the magnetic penetration depth λ and the coherence length ξ

$$\kappa = \frac{\lambda}{\xi}. \tag{2.4}$$

Figure 2.3 illustrates their spatial extension at the interface with a normal phase. This surface energy alters its sign depending on the value of κ and for a given field H. The exact critical value of κ that distinguishes type-I from type-II superconductors is $1\sqrt{2}$ (~ 0.7). In the case $\xi > \lambda$ ($\kappa < 1/\sqrt{2}$), the surface energy will be positive, which does not favor the appearance of a superconducting-normal interface. As long as the critical field H_c is not reached, the superconductor remains in the Meissner state. Conversely if,

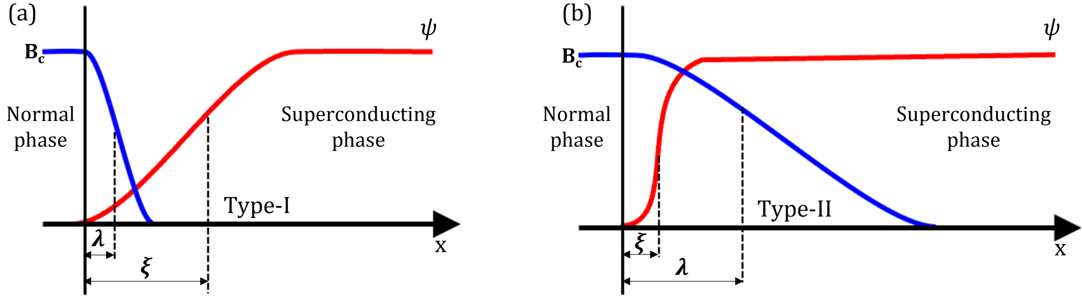

Figure 2.3: **The interface between normal and superconducting states for type-I and type-II superconductors.** Type-I superconductors have a penetration length, smaller the than coherence length ($\kappa < 1/\sqrt{2}$). Type-II superconductors have a penetration length larger than the coherence length ($\kappa > 1/\sqrt{2}$).

$\xi < \lambda$ ($\kappa > 1/\sqrt{2}$), this energy is negative above a certain value H_{c1} given by

$$H_{c1}(T) = \frac{\Phi_0}{4\pi\mu_0\lambda^2(T)}\text{In}\kappa \tag{2.5}$$

and the creation of normal-superconductor interfaces becomes energetically favorable, permitting the magnetic field to penetrate the material. The penetration of the field is in the form of vortices, each carrying one quantum magnetic of flux Φ_0 (Equation 2.2). When H_{c1} is reached, superconductivity no longer vanishes suddenly with increasing magnetic field but instead gradually disappears until H_{c2} is reached, given by

$$H_{c2}(T) = \frac{\Phi_0}{2\pi\mu_0\xi^2(T)} \tag{2.6}$$

It would be fair to say that the GL theory accomplished an important feat when it distinguished between two types of superconductors. In addition, this theory offers an overview of the superconducting vortex, from the flux quantization to its interaction with neighbor vortices, leading to the formation of the Abrikosov lattice [8].

2.3 Weak links and Josephson Effect

It has been our goal so far to describe the key elements of the macroscopic model of superconductivity. The Josephson effect is another macroscopic quantum phenomenon that is peculiar to superconductors. In his proposal, in 1962 [13], Josephson considered two superconductors weakly coupled by a thin insulating barrier that allowed quantum tunneling of Cooper pairs, as long as the barrier thickness would be less than - or comparable to - the coherence length ξ. According to him, there would be some unusual phenomena

in this situation, in particular, a tunneling current at zero bias voltage that would be re-entrant under applied magnetic fields. Shortly thereafter, Anderson and Rowell confirmed this prediction experimentally [14], leading to Josephson and Anderson receiving the 1973 Nobel Prize. The concept of Josephson junctions or weak links refers to structures that exhibit these properties (of which the tunnel junction described is the simplest example). There are also weak links that can be formed between regions of superconducting materials of low T_c by means of a point contact [15] or a constriction [16]. It is also possible to use a metallic or semiconducting barrier, either in a sandwich configuration [17, 18] or in a variable-thickness bridge configuration [19]. High T_c materials have extremely short coherence lengths, and merely the presence of a grain boundary is sufficient to create a junction [20]. A collection of weak links with various geometries is presented in Figure 2.4.

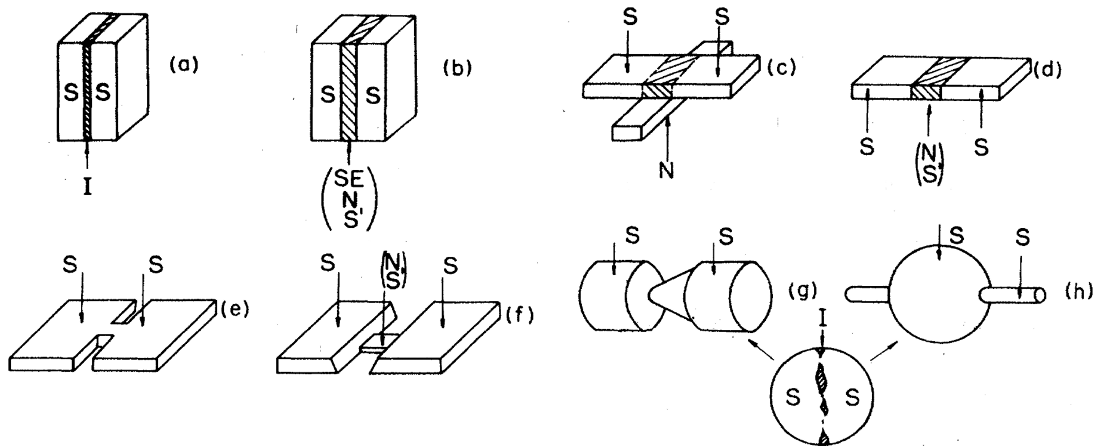

Figure 2.4: **Various types of structures where the Josephson effect can take place.** (a) tunnel junction considered in Feynman's derivation, with S a superconductor and I an insulator. The junctions from (b) to (f) have direct (non-tunnel) conductivity: (b) sandwich, (c) proximity effect bridge (d) ion implanted bridge, (e) Dayem bridge, (f) variable thickness bridge, (g) point contact and finally, (h) blob type contact. S stands for superconductor, S for the superconductor with reduced critical parameters, N for normal metal or alloy, SE for semiconductor, and I for insulator. Figure taken from [21].

Generally, Josephson effects are predicted in systems with macroscopic phase coherence, and have recently been reported for superfluid ^{3}He [22, 23] and Bose-Einstein condensates [24]. Arrays of weak links formed by pressed pellets of superconducting grains have also been demonstrated [25] to respond as Josephson junctions. In our case, we electromigrated Nb bridges prepared with different angles and investigated the typical signatures of Josephson junctions in the weak links generated by the EM process. These signatures will be discussed in the following sections.

2.3.1 Josephson effect

The Josephson effect is typically depicted as the flow of a supercurrent through a barrier separating two superconductors. This barrier is typically of the order of a few nanometers. An example of such a device, known as the Josephson junction, can be found in Figure 2.5. As a first step, we assume that the supercurrent is uniform across the entire junction and that the superconducting electrodes represent Cooper pair reservoirs. A phase correlation between the two superconductors can be realized in this distance, as Cooper pairs can flow through the device without any voltage drop. As a matter of fact, the nature of this phase correlation is entirely quantum, but at the same time it is something considerably more complex. Actually, the phase difference between the two superconductors of the junction is a macroscopic variable regulated by the Josephson equations we will present briefly.

Using an example set forth by Josephson in his original paper[13], we analyze the simpler case of a junction between two superconductors. However, we do not follow Josephson's approach for reasons of mathematical simplicity. Instead, we use the two-state picture proposed by Feynman [26]. It should be noted that this approach is considered without taking the field into account.

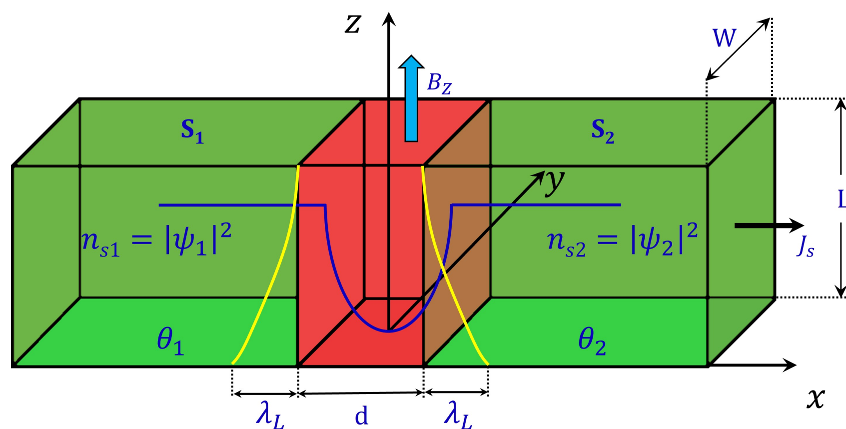

Figure 2.5: **Schematic representation of a Josephson junction.** The superconductors are depicted in green labelled S_1 and S_2, respectively, accompanied by their density of Cooper pairs ψ_1 and ψ_2. In the case of the supercurrent J_s, it flows in the x direction. An insulator with a thickness of d is represented by the red region.

Consider two superconductors separated by an insulator of length d as depicted in Figure 2.5. Let then ψ_1 (ψ_2) be the macroscopic wavefunction of the S_1 (S_2) superconducting electrons characterized by a particular phase θ_1 (θ_2). In the absence of interactions between

the superconductors, the evolution is described through ordinary Schrödinger equations:

$$i\hbar\frac{\partial\psi_1}{\partial t} = \mathbf{H}_1\psi_1 \tag{2.7a}$$

$$i\hbar\frac{\partial\psi_2}{\partial t} = \mathbf{H}_2\psi_2. \tag{2.7b}$$

If K is the coupling constant that couples the two superconductors across the barrier as they are brought towards each other, then the coupled Schrödinger equations for a Josephson junction are

$$i\hbar\frac{\partial\psi_1}{\partial t} = E_1\psi_1 + K\psi_2 \tag{2.8a}$$

$$i\hbar\frac{\partial\psi_2}{\partial t} = E_2\psi_2 + K\psi_1. \tag{2.8b}$$

A finite value of the coupling amplitude K allows tunneling from one side to the other. Assuming both sides are identical, then $\mathbf{H}_1$ equals $\mathbf{H}_2$. However, if a voltage bias is applied across the junction then $\mathbf{H}_1 - \mathbf{H}_2 = 2eV$. Defining the zero of energy halfway in between the insulator layer, the two equations become:

$$i\hbar\frac{\partial\psi_1}{\partial t} = eV\psi_1 + K\psi_2 \tag{2.9a}$$

$$i\hbar\frac{\partial\psi_2}{\partial t} = -eV\psi_2 + K\psi_1. \tag{2.9b}$$

Using the general form of the macroscopic wavefunction ($\psi(\boldsymbol{r}) = |\psi(\boldsymbol{r})|\, e^{-i\theta(\boldsymbol{r})}$ and $\phi = \theta_2 - \theta_1$), we obtain the following set of equations:

$$\frac{\partial n_{s,1}}{\partial t} = \frac{2K}{\hbar}\sqrt{n_{s,1}n_{s,2}}\sin\varphi \tag{2.10a}$$

$$\frac{\partial n_{s,2}}{\partial t} = -\frac{2K}{\hbar}\sqrt{n_{s,1}n_{s,2}}\sin\varphi \tag{2.10b}$$

$$\frac{\partial \theta_1}{\partial t} = -\frac{K}{\hbar}\sqrt{\frac{n_{s,2}}{n_{s,1}}}\cos\varphi - \frac{eV}{\hbar} \tag{2.10c}$$

$$\frac{\partial \theta_2}{\partial t} = -\frac{K}{\hbar}\sqrt{\frac{n_{s,1}}{n_{s,2}}}\cos\varphi + \frac{eV}{\hbar}. \tag{2.10d}$$

As long as we have equivalent superconductors on either side of the junction, we can set $n_{s,1} = n_{s,2} = n_s$, which is the local density of superconducting electrons defined as $n_s = |\psi(\boldsymbol{r})|^2$. It is also assumed that as a result of the interaction, the electron density does not significantly deviate from its equilibrium value. The current density is just given

by $J_s = 2e\partial n_s/\partial t$, thus we find:

$$J_s = \frac{4eK}{\hbar}\sqrt{n_s^2}\sin\varphi = \frac{4eK}{\hbar}n_s\sin\varphi. \tag{2.11}$$

Defining $J_c = \frac{4eK}{\hbar}\sqrt{n_{s,1}n_{s,2}}$ and inserting it into the above equation leads us to the *first Josephson equation*:

$$J_s = J_c\sin\varphi \qquad \textbf{(DC Josephson effect)} \tag{2.12}$$

where J_c is the *critical current density* and φ is the phase difference between the two superconducting order parameters. The φ across the junction is assumed as a constant in the y direction i.e., in the absence of external bias voltage, a current of Cooper pairs flows through the junction and therefore the gauge invariant phase difference has to be considered. The total current flowing through the junction can be calculated integrating Equation 2.12, and the Josephson equation in Equation 2.12 is now:

$$I_s = I_c\sin\gamma \tag{2.13}$$

where

$$\gamma = \varphi - \frac{2\pi}{\Phi_0}\int_{-d/2}^{d/2}\boldsymbol{A}\cdot d\boldsymbol{l} \tag{2.14}$$

is the gauge invariant phase difference and $\boldsymbol{A}$ is the vector potential.

Josephson's second prediction related the time evolution of the phase difference with the bias voltage V. Subtracting Equation 2.10c from 2.10d leads us to *second Josephson equation*:

$$\frac{\partial\varphi}{\partial t} = \frac{2e}{\hbar}V. \qquad \textbf{(AC Josephson effect)} \tag{2.15}$$

Even though Josephson's theory was subject to controversy at the time, it was quickly accepted after Anderson and Rowell confirmed that the modulation of the I_c can be observed in the presence of an external magnetic field [14]. We conclude that:

- the *first Josephson equation* correlates the phase difference at the Josephson contact with the current of the Cooper pairs over this contact;
- the *second Josephson equation* shows that the phase difference γ changes linearly with time in case of a potential difference between both superconductors.

2.3.2 Junction under a magnetic field

So far, we have only examined the behavior of a Josephson junction in the absence of magnetic fields. Continuing with the same type of Josephson junction that is shown in Figure 2.5, let us now consider it immersed in a magnetic field perpendicular to the direction in which the current is flowing.

An external magnetic field can have a significant impact on the critical current of a junction, by modulating it in response to that field. An example of the simplest case is that of a short junction, where the redistribution of current under the influence of the self-field can be ignored. As long as there is no applied magnetic field, the phase difference between the superconducting electrodes is uniform. Therefore, the DC Josephson relation holds, and the current distribution across the junction is uniform. However, when a Josephson junction is subjected to a magnetic field B_z, the field penetrates not only the junction (thickness d), but also the superconducting electrodes up to the penetration depth λ. The flux Φ threading through the junction depends on the effective length penetrated by the magnetic field $l_{eff} = \lambda_1 + \lambda_2 + d$. The gauge invariant phase difference then varies linearly with distance along the junction:

$$\frac{\partial \varphi}{\partial x} = \frac{2\pi}{\Phi_0} B_z l_{eff}. \tag{2.16}$$

Integrating this equation and inserting it into Equation 2.12 leads us to:

$$J_s = J_c \sin\left(\frac{2}{\Phi_0} B_z l_{eff} x + \varphi_0\right). \tag{2.17}$$

It follows that the supercurrent is influenced by the spatial variations of the gauge invariant phase difference as a result of the applied field. The critical current I_c is then obtained by maximizing I with respect to the constant of integration φ_0. For a uniform critical current density J_c, the amplitude of the supercurrent through the junction is,

$$I_s^{Max}(\Phi) = I_c \left| \frac{\sin\left(\frac{\pi\Phi}{\Phi_0}\right)}{\frac{\pi\Phi}{\Phi_0}} \right|. \tag{2.18}$$

Thus the amplitude of the supercurrent through the junction varies as the modulus of a sinc function. This is analogous to the Fraunhofer pattern in a single slit optical diffraction experiment.

As the junction becomes longer, and the current distribution is no longer uniform, $I_s^{Max}(\Phi)$ deviates from the Fraunhofer pattern. The $I_s^{Max}(\Phi)$ of long junctions eventually enters a regime of a multivalued function due to self-field effects [27]. The length scale over which self-field effects arise is the Josephson penetration depth, λ_J:

$$\lambda_J = \sqrt{\frac{\Phi_0}{2\pi\mu_0 l_{eff} J_c}} \tag{2.19}$$

Those junctions with a width $w \gg \lambda_J$ are classified as long junctions (since λ is

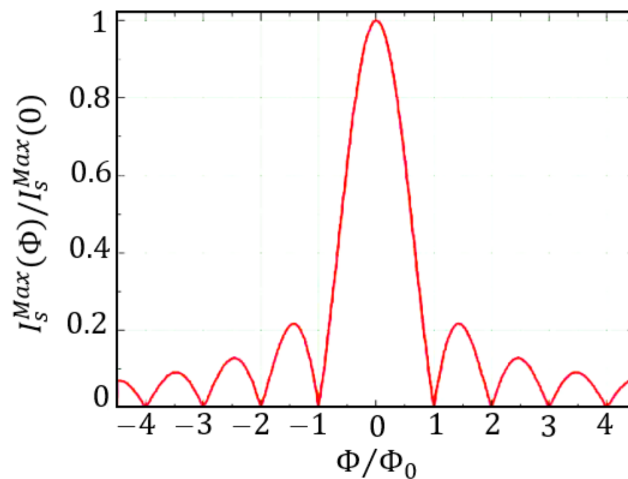

Figure 2.6: **Typical Fraunhofer pattern.** Modulation of critical current with magnetic flux (Fraunhofer pattern) in a short Josephson junction.

temperature-dependent, a short junction can become long as the temperature decreases.) The critical current is no longer proportional to the junction area as current flow becomes confined to the edges of the junction. Depending on the applied magnetic field value, there may be various possible solutions for the critical current, corresponding to different numbers of flux vortices trapped in the junction. It should be noted that when self-field effects are involved, the geometry of the current input also plays an important role in determining the overall shape of $I_s^{Max}(\Phi)$ whose short junction limit is shown in Figure 2.6.

Chapter 3

Electromigration in metals

This chapter presents an overview of the basic knowledge regarding the process of atomic migration induced by an electron wind, a phenomenon which is generally referred to as electromigration (EM). As part of this overview, we will examine the main theory that describes this phenomenon in order to comprehend the pertinent elements necessary to understand its physics. Last but not least, we describe the technique we have developed in order to obtain some control over this stochastic phenomenon so as to induce structural and physical changes in multiterminal transport bridges

3.1 Introduction

In the design of integrated circuits, reliability is an essential factor, as users expect the product to have long flawless lifetimes. It is, however, likely that failure rates will increase as chip structures become smaller and smaller, resulting in a gradual shrinkage of the interconnect cross-sections while supply voltages slowly rise, leading to higher current densities and temperatures [28]. These factors led to increased migration issues, especially EM, within the interconnects, which reduced the product's service life. EM can cause several types of reliability issues in electronic devices, including: interconnect failures, transistor failures, and circuit degradation.

As a whole, the industry experienced a great deal of shock in the late 60's. In general, the operation time was of the order of several weeks, and once the device failed, it was challenging to determine the cause of the failure. This was because the traditional analytical techniques, such as optical microscopes, could not provide the necessary resolution to identify the root cause of the failure. It was during this time that a relatively novel research tool called Scanning Electron Microscope (SEM) became available, enabling the ultimate cause of breakdown to be discovered. SEM facilitated the capture of high-resolution imaging of a sample's surface and allowed researchers to see details that were previously invisible under a traditional microscope. The failure sites were identified as tiny cracks, voids, and hillocks in the metallic tracks, sometimes measuring only a few nanometers wide, thereby escaping optical microscopy examination. The development of SEM significantly impacted the semiconductor industry, allowing companies to improve the quality and reliability of their products. By identifying the root cause of deterioriation, manufacturers could make changes to their manufacturing processes and materials to reduce the occurrence of failures in the future. Then it led to increased confidence in the reliability of ICs, which in turn helped to drive the growth of the electronics industry.

As a result of this discovery, many more research activities have been conducted in the study of EM in thin film conductors. The majority of studies conducted in the late 60's and 70's focused on the practical issue of conductor line failure, or the 'cracked stripe' problem in microelectronics integrated circuits with the objective to extend the lifespan of consumer electronics. However, in recent years, the focus has shifted to learning the physical principles underlying the phenomenon and how to master it. Controlling the EM process can yield several benefits as demonstrated by numerous studies. As an example, EM has been productively harnessed for applications such as resistive switches

[29–31], nanoheaters [32], plasmonic nanoantennas [33], nanogap biosensors [34] and, more commonly, single molecule nanogap junctions [35–39]. Currently, controlled EM has the advantage of being extremely easy to achieve due to the fact that it can be accomplished using rather unsophisticated software and conventional electronics [40–42].

3.2 Electromigration: Physical Background

Electromigration is a mass transport process operating in metal films when subjected to electrical current [43]. When atoms come together to form a metal, the electrons from the outer atomic shell become delocalized. These electrons are free to move through the lattice of positive ions. A perfect lattice cannot exist above absolute zero due to missing (vacancies) or self-interstitial atoms, interstitial or substitutional atoms (impurities), boundaries between crystals of different orientation (grain boundaries), lower coordination of surface atoms, and regions of discontinuity in the crystalline lattice (dislocations). Some of these defects are illustrated in Figure 3.1.

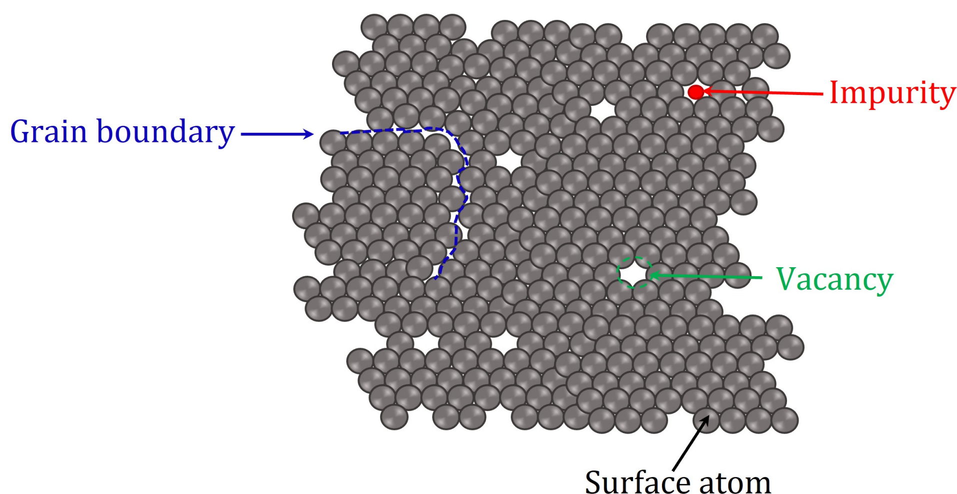

Figure 3.1: **Portion of crystalline lattice exhibiting defects**: atom vacancies, impurities and grain boundaries.

In this list, vacancies and grain boundaries are particularly important to allow ions to move from their fixed position in the lattice. This process is known as diffusion or migration.

In the absence of a net electrical current, the electron scattering and the associated momentum transfer have no privilege direction. During their movement, electrons collide with the lattice ions, which is crucial to understanding thermal equilibrium. The average velocity due to thermal energy is zero. Applying an eletric field, one can affect this free

motion of electrons. In the presence of a current, electron scattering transmits momentum in a preferential direction. The atomic transport is a result of momentum transfer between conduction electrons and lattice atoms as a result of collisions in the ohmic conduction regime. Nonetheless, atom displacement cannot be caused by just one electron scattering. In fact, a single electron traveling in a conductor between two scattering events will gain an average amount of energy expressed as:

$$E_{e-} = \rho e J l \tag{3.1}$$

where ρ is the resistivity, e is the unit charge, J is current density, and l is the electron mean free path. Typically, base metals have a resistivity of 10^{-6} Ωcm and a mean free path of tens or hundreds of nanometers, so from Equation 3.1, the energy gained by an electron is about 10^{-4} eV. This is quite small in comparison to the activation energy (E_a) of an atom, which is usually around 1 eV [44]. Hence, in order to equalize the diffusion energy of the atoms, very high current densities J (of the order of $10^4 - 10^7$ A/cm^2) are required. It is therefore essential that EM must be viewed as a collective action involving high current density sufficient to ensure that electrons within the lattice are scattered on a large scale. In addition, the scattering effect is further accentuated in metals due to the Joule heating effect, which increases their thermal vibrations.

Individual metal ions in a conductor are exposed to two forces when current flows through them, the first being an electrostatic force, F_E, created by the electric field strength. The second force, F_{wind}, is connected with the momentum transfer between conduction electrons and metal ions in the crystal structure. This force associated with the momentum transfer is also known as “electron wind force”. Considering that the positive metal ions are shielded to some extent by the negative electrons in the conductor, it is possible to neglect the force exerted by the electric field (quite small). Consequently, the dominant force is the electron wind. The concept of this electron wind is illustrated in Figure 3.2. If the resulting force in the direction of the electron wind (which also corresponds to the energy transmitted to the ions) exceeds E_a, a directed diffusion process starts. The resulting material transport takes place in the direction of the electron motion. A result of this displacement of atoms is that regions of the structure become depleted of atoms, which are referred to as voids, and the displaced atoms accumulate in other regions, eventually forming overgrowths called hillocks or extrusions, as illustrated in Figure 3.3.

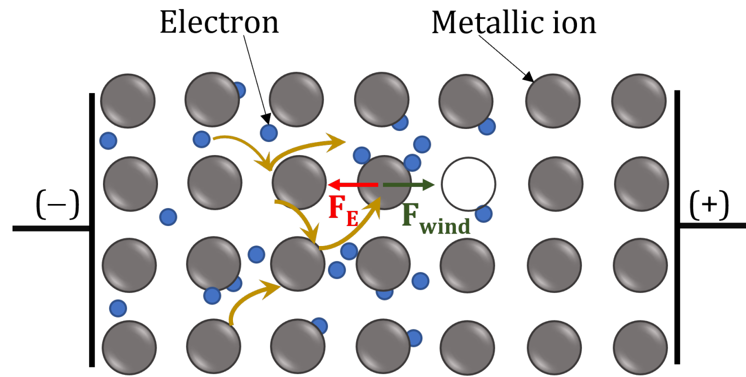

Figure 3.2: **Forces acting on an atom in an EM process.** F_E indicates the force on the positive ion exerted by the electric field and F_{wind} corresponds to the average force produced by the momentum transfer of the electron-ion collision.

The formation of voids reduces the effective cross-section of metal lines and increases current density. There is no doubt that the production of a void along a conducting strip will lead to current crowding and substantial Joule heating. Consequently, EM occurs at an accelerated rate, resulting in open circuits. Conversely, hillocks can cause an electrical short circuit to nearby conductors. As a result, EM has been widely investigated, and a number of reviews on the subject have been published [43–47].

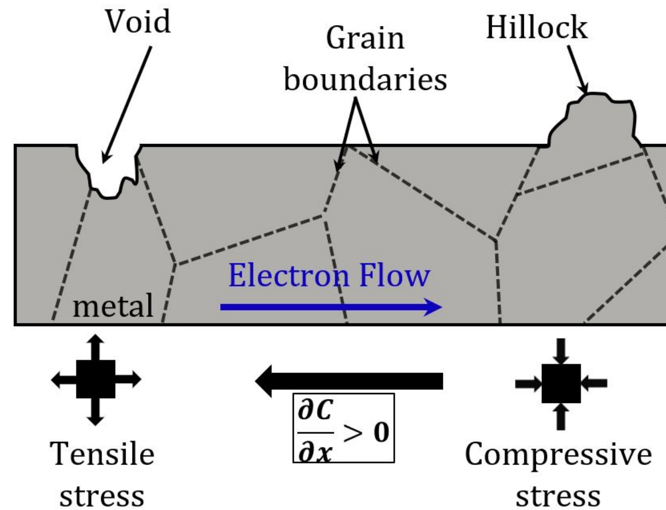

Figure 3.3: **Formation of hillocks and voids in a polycrystalline line of metal.** Voids and hillocks form as a consequence of concentration/stress gradients.

3.2.1 Mass flux

As mentioned earlier, electromigration damage occurs primarily through the momentum transfer between conducting electrons and lattice ions, resulting in a mass flux in the direction of electron flow. Essentially, mass flux results from a combination of two

phenomena: thermal diffusion of ions, which can be considered isotropic at the lattice level, as well as directional drift caused by the electron wind, which is superimposed to diffusion and defines a preferred direction. The concept of the electron wind driving force was first formulated by Fiks in 1959 [48] and followed by Huntington and Grone in 1961 [49]. They independently employed a *ballistic* approach to treat the collision of the moving atom with the charge carriers.

As shown in Figure 3.2, the direct electrostatic force on the ion and the electron wind force are proportional to the applied electric field, therefore the total EM driving force can be written as [48–52],

$$F = F_{wind} - qE = q^*E \tag{3.2}$$

where q^* is the effective charge and E is the applied electric field. Using ohm's law $E = \rho J$ and taking $q^* = Z^*e$ we have the total EM force to be

$$F = Z^*e\rho J \tag{3.3}$$

where e is the elemental charge, ρ the resistivity, J the current density. Z^* is a quantity referred to as effective valence or effective charge. It is actually neither, but is a term that represents the magnitude and direction of the momentum exchange [53], given as

$$Z^* = \frac{1}{2}\frac{\rho_d N}{\rho N_d}\frac{m^*}{|m^*|} \tag{3.4}$$

where ρ_d is the specific defect resistivity defined as $\rho_d = |m^*|/ne^2\tau_d$ where n is the electron density and τ_d representing their relaxation time after momentum transfer with a point defect [49]. ρ is the resistivity of the metal, N the metal ion density, N_d is the density of defects and m^* is the effective mass of the carriers participating in the momentum exchange. The sign of Z^* determines the nature of the transport mechanism. Negative value of Z^* means the transport direction is consistent with the electron flow. A key topic in the study of EM has been the measurement of Z^* for different types of metals [54]. According to Gupta *et al.* [55], the electron-wind force, which is responsible for EM, is determined by an integral over the Fermi surface, which is rather complicated and essentially holelike in Nb and Ni, i.e. $Z^* > 0$. This is in contrast to Al, for which $Z^* < 0$ [54].

Generally, it can be considered that electrons are particles moving in a lattice that is overdamped due to collisions, which explains why the force is not proportional to

acceleration but rather to velocity. From this perspective, we then define the mobility μ as the ratio of the drift velocity υ_d to the force F, i.e.

$$\mu = \frac{\upsilon_d}{F} \tag{3.5}$$

Hence, this allows us to express the drift velocity of atoms due to the EM force, υ_{EM}, as

$$\upsilon_{EM} = \mu Z^* e\rho J. \tag{3.6}$$

In order to account for thermal diffusive processes, we use Einstein diffusion relation $D = \mu k_B T$ so that Equation 3.6 becomes

$$\upsilon_{EM} = D\frac{Z^* e\rho J}{k_B T}. \tag{3.7}$$

Equivalently one may view the mass flux as a vacancy flux in the opposite direction. With this equivalence, the vacancy flux due to EM, Θ_v can be easily expressed by

$$\Theta_v = -C\upsilon_{EM} = -CD\frac{Z^* e\rho J}{k_B T} \tag{3.8}$$

where C is the concentration of vacancies. The mass flux caused by thermal diffusion and EM-induced drift velocity is not sufficient to cause failure. For instance, in order to create a void, less mass must enter a particular region than exit. As shown in Figure 3.3, a situation in which there is less mass leaving than arriving leads to hillocks. These specific regions are identified as flux divergence points [45]. In particular, contact points and electrode surfaces are favorable positions for EM damage. In order to explain flux divergences, it is important to recognize that mass transport is not solely controlled by the EM driving force (Equation 3.3) but also by other processes including **chemical diffusion**, **thermal migration** and **stress migration** which are caused by the concentration and thermal gradients and mechanical stress, respectively. In Section 3.3, these processes will be discussed.

Nevertheless, as a mean of accounting for the total mass flux, the vacancy concentration gradient ($\frac{\partial C}{\partial x}$) is taken into consideration and the mass transport Θ_m can be expressed as,

$$\Theta_m = D\left(\frac{\partial C}{\partial x} - C\frac{Z^* e\rho J}{k_B T}\right) \tag{3.9}$$

with time dependent behavior given by the continuity equation,

$$\frac{\partial C}{\partial t} = \frac{\partial \Theta_m}{\partial x}. \tag{3.10}$$

Typically, EM lifetime experiments are conducted under accelerated conditions where test samples are subjected to high levels of accelerating variables such as temperature and current density. Based on the results of the tests, predictions about the lifetime during actual use conditions are made using the acceleration factor derived from the parameters. In order for the whole procedure to be valid, it is essential to use a physical or failure model that is accurate. A number of propositions have been made ranging from the empirical, such as Black's original equation [56], to the semi-empirical, such as the reference provided by Hu and co-workers [57], to the more quantitative continuum descriptions including drift-diffusion model [58–60] and stress evolution model [61, 62].

3.2.2 Empirical point of view : Black's model

James Black was the first to introduce an expression for the mean time to failure of a metal line subjected to EM [56]. He considered that the mean time to failure, $t_{\frac{1}{2}}$, is inversely proportional to the momentum transfer between thermally activated ions and conducting electrons:

$$t_{\frac{1}{2}} \propto \frac{1}{d_e \Delta p D_a} \tag{3.11}$$

where d_e is the density of conducting electrons, Δp is the momentum transferred from an electron to an ion, and D_a is the diffusion coefficient which is thermally activated process. He also assumed that both electron density and momentum are proportional to the current density ($d_e \propto J$ and $\Delta_p \propto J$), and that the diffusion is governed by Arrhenius' law as

$$D_a = D_o \exp\left(\frac{-E_a}{k_B T}\right) \tag{3.12}$$

where T is the absolute temperature, and k_B is the Boltzmann's constant. Hence, the equation of the mean time to failure introduced by Black is:

$$t_{\frac{1}{2}} = \frac{A}{J^2} \exp\left(\frac{E_a}{k_B T}\right) \tag{3.13}$$

where A is a constant depending on the geometry of the device. To allow the model to be applied to different types of dominant failure mechanisms, the constant exponent 2 of

J has been replaced by a variable n, generating a great debate about the value of this exponent. Lloyd has pointed out that although the model is fairly well accepted, it is not in agreement with solid state physics which indicates that the driving force for EM should have a n exponent of 1 [63]. Additionally, he mentioned other arguments that relate the J^2 dependence to Joule heating. According to him, Joule heating can result in different and unbounded values for n. If failure is to occur, flux divergence must occur, which may result from the temperature gradient produced by Joule heating. With an increase in J, not only will the temperature and flux increase exponentially, but also the flux divergence will increase. In this regard, he argued that n would rise without bound and would be very sensitive to changes in applied current. Therefore it would be very difficult, if not impossible, to make extrapolations to other conditions such as a flux divergence caused by structural defects. Based on empirical studies that fit this model, the value of n has generally been found to range from 1 to 3 [43]. Several studies have demonstrated that the variation in n value reflects the relative contribution of void nucleation and void growth stages to the total failure time [64].

3.3 Mechanisms related to atomic diffusion

EM is merely one of the factors that lead to atomic diffusion in metals, as was already mentioned. There are also three other causes to consider: **chemical diffusion**, **stress migration** and **thermal migration**. Atoms diffuse along interfaces, grain boundaries, and through lattices due to several driving forces: the electron wind, an entropic diffusion force driven by thermal gradients, an entropic diffusion force driven by atomic concentration gradients, and a mechanical stress force driven by mass density gradients or thermal expansion mismatches. As can be seen, the physical nature is different. Nevertheless, they cannot be considered independent. A schematic diagram of this situation is depicted in Figure 3.4, and the relationships between each element are discussed in the following subsections.

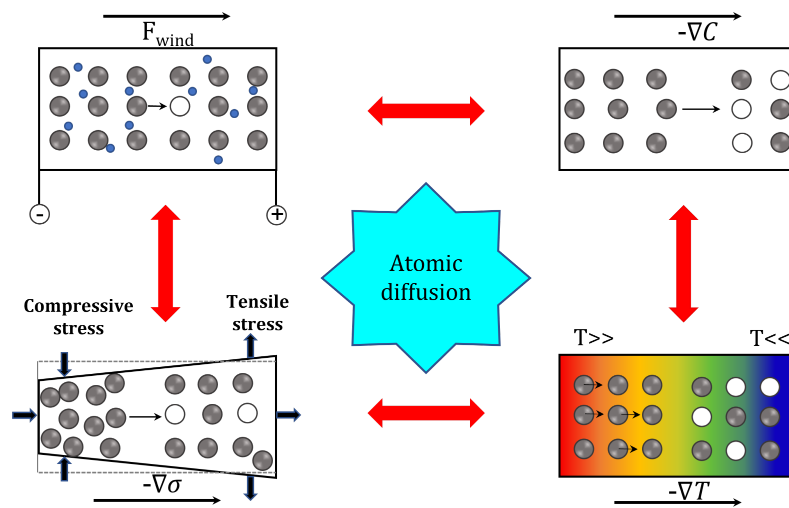

Figure 3.4: **Atomic diffusion in solids: interaction of different causes.** Interaction and coupling between electromigration (top-left corner), concentration gradient (top-right corner), mechanical stress (bottom-left corner), and temperature gradient (bottom-right corner), through their driving forces. They are closely coupled processes as their driving forces are linked with each other and with the net migration change (red double arrow). Reproduced from [65]

3.3.1 Chemical diffusion

In the presence of a concentration (or chemical potential) gradient, chemical diffusion occurs, causing a net mass transport as well. The diffusion process is always a nonequilibrium process. It raises the system's entropy* and provides a means of bringing the system closer to equilibrium. Out of equilibrium, the system will consequently have a tendency to relax over time, and the effects that the EM had previously caused may gradually be healed. Occasionally, migration processes can reach an equilibrium state in which another type of migration serves as a limiting (or counteracting) process. The studies published by Blech and Herring [66] and Blech [67] shows that the concentration gradient and stress result in a threshold product of current density below which EM halts at equilibrium. Based on this observation, it was suggested that a reverse Al flow created by concentration gradients and back stress balances the forward EM flow, thereby preventing any net flow from occurring.

3.3.2 Stress migration

Essentially, Stress Migration is characterized by diffusion-controlled processes where mechanical stress gradients act as the driving force for the transport of materials. Metal

*Entropy is a measure of a system's "disorder." As a result, the lower the entropy of a system, the more "ordered" or "organized" it is.

atoms move out of regions under compressive stress whereas there is a net atomic flow into regions where tensile forces are at work. This causes diffusion in the direction of the negative mechanical tension gradient, just like thermal migration does. The vacancy concentration is thereby balanced to be equal with the mechanical stress. Mechanical stress plays a significant role in interconnect electromigration. Based on Ref [66, 68], the stress caused by atomic density gradients leads to a backward diffusion flux that opposes the EM. In the event that voids or hillocks cannot relieve the stress, then the back flow flux can completely balance the wind force flux. Under certain critical lengths, blocking conditions at the end of the interconnect can create fully counterbalanced stress gradients prior to any void nucleation, almost eliminating the presence of EM effects.

Also, as indicated by Lloyd [69], mechanical stress plays three important roles in EM failure:

(i) Stress gradients act as a driving force for metal atom motion just like EM and the concentration gradient;

(ii) A film is likely to fail once it reaches critical stress due to the formation of extrusions or voids, depending on whether the stress is compressive or tensile;

(iii) The action of stress directly affects the diffusion of atoms through their concentration gradient. Tensile stress makes diffusion easier and compressive stress makes diffusion more difficult.

3.3.3 Thermal migration

Thermal migration (TM), also known as thermomigration, occurs as a result of temperature gradients. By virtue of the various thermal absorption and conduction characteristics of materials, the temperature distribution under a current flow or an external temperature load may not be uniform. Due to the increase in temperature brought about by Joule heating, the vibration of each atom becomes more intense, reaching their activation energy and allowing them to diffuse in the lattice. In this case, high temperatures increase the average speed of atomic motion. It is generally accepted that TM is a byproduct of EM due to the imbalance of Joule heating generated at interconnections, and most studies have documented the fact that the impact of TM cannot be identified independently from EM [38, 70, 71]. A direct relationship between EM-induced mass flow and diffusion constant D can be seen from Equation 3.8. Because diffusion is a thermally activated process characterized by the Arrhenius relation, atoms at higher temperatures are more

likely to dislocate than at lower temperatures. A visual representation of this fact can be seen in Figure 3.4 at the bottom-right corner. The presence of a temperature gradient will generate mass flux from hot regions, where atoms are active, towards cold regions, where ions have lower kinetic energy. Depending on the geometry of the structure, the temperature gradient can be in the same or opposite direction as electron flow.

When a void is generated along a conducting strip, there will be current crowding and substantial Joule heating. In turn, the localized hot spot will generate a temperature profile which will decay within a few microns to the bath temperature. Therefore, it is possible to achieve temperature gradients as high as 10^4 to 10^7°C/cm [72]. It is necessary to include the flux divergences generated by temperature gradients in Equation 3.10 as follows:

$$\frac{\partial C}{\partial t} = \left.\frac{\partial \Theta_m}{\partial x}\right|_T + \left.\frac{\partial \Theta_m}{\partial T}\right|_x \frac{\partial T}{\partial x}. \tag{3.14}$$

It can be seen from the continuity equation that the effects of temperature gradients are just as important as the effects of concentration gradients within the material. In the case where $\frac{\partial T}{\partial x} \gg \frac{\partial \Theta_m}{\partial x}$, the second term on the right hand side of Equation 3.14 dominates and the system failure will occur at the point where the temperature gradient is the greatest.

The Joule heating effect

Joule heating is the process by which the energy of an electric current is converted into heat as it flows through a conductor due to electron scattering processes. As previously stated, the formation of a void along a conducting strip causes current crowding and significant Joule heating due to the electrical current that causes EM. Since resistivity is temperature dependent, passing current through a metallic conductor induces Joule heating and thus alters its resistance. An empirical relation to describe the evolution of resistivity ρ with temperature is given by

$$\rho = \rho_0[1 + \alpha(T - T_0)] \tag{3.15}$$

where ρ_0 is the reference resistivity at temperature T_0 and α is a temperature coefficient. Equation 3.15 can be written in terms of the resistance as

$$R = R_0(1 + \alpha \Delta T) \tag{3.16}$$

where R_0 is the resistance at the reference temperature T_0 and $\Delta T = T - T_0$. By using a solution of the Fourier law, $\Delta T = R_\theta P$, with R_θ being the thermal resistance and $P = R(T)I^2$ the dissipated electrical power, the above equation can be rewritten as

$$R(T) = \frac{R_0}{1 - \gamma R_0 I^2} \tag{3.17}$$

where $\gamma = \alpha R_\theta$ is a constant that is affected by specific heat, thermal conductivity, heat transfer to the substrate and the sample geometry. Based on Equation 3.17, we can calculate the resistance value of a self-heated metallic conductor by using a current as the driving force. Thus, the resistivity of a metallic conductor will therefore increase with the electrical current, until the activation energy of the ions is reached, and they are able to diffuse.

3.3.4 The resultant diffusion flux

The various atomic fluxes at any point can be expressed mathematically as independent expressions (although in the end, they are coupled in time, since e.g. a wind-force driven flux of atoms into a region results in a mechanical stress). As a result, the total vacancy flux can be generally written as [73]

$$\Theta_v = -D\left(\nabla C - \frac{Z^* e}{k_B T} C\rho J - \frac{Q}{k_B T^2} C\nabla T + \frac{f\Omega}{k_B T} C\nabla\sigma\right) \tag{3.18}$$

The terms are, from left to right, diffusion induced by the gradient of the vacancies ∇C, next the EM term itself, and lastly the driving forces due to gradients of temperature ∇T and mechanical stress gradients $\nabla\sigma$, where f represents the relaxation factor of vacancies and Ω represents atomic volume, respectively. The complexity of this equation, which can only be solved numerically, demonstrates how difficult it is to predict with accuracy the effects of large electrical currents on metallic nanostructures, and on interconnections. However, from a research standpoint, it is established that the first location where atoms will migrate from is the narrowest constrictions we can create in a device (which will also have the highest temperature gradients). This enables accurate experimental designs to investigate the impact in further detail in applications involving particular materials.

3.4 Effects of microstructure

It is possible for metallic materials to have different structures in the micrometric range. A polycrystalline, fine-grained structure is the most common type of microstructure in metallic interconnects. Based upon the ratio between grain size and interconnect dimensions, polycrystalline interconnects composed of few grains can also exist, as can bamboo-like structures, monocrystal structures, and amorphous structures. For analyzing the causes and effects of EM, these categories for micrometric structures are particularly helpful since there are several paths through which the ion can diffuse in the lattice, each corresponding to its own diffusivity constant. As stated above, the diffusion coefficient D is a measure of the magnitude of the atomic flux. In addition to temperature and pressure, it is a physical constant that depends on the atomic size and other characteristics of the diffusing substance. The diffusion coefficient is calculated in the case of the combined grain-boundary and bulk diffusion as follows [74]:

$$D = D_v + \delta \frac{D_b}{d} \tag{3.19}$$

where D_v is the diffusion coefficient for the bulk (volume) diffusion and D_b the diffusion coefficient along the grain boundaries of width δ and grain size d. Diffusivity is typically high at the surface and along grain boundaries. In these locations, the binding energy of the ion is lower than in bulk, so they are more easily excited by thermal fluctuations and subsequently carried away by the wind force. As shown in Table 3.1, different diffusion paths are distinguished by different activation energies E_a.

Table 3.1: Activation energies for different diffusion in different metals

Metals	Melting (K)	Activation energy E_a (eV/atom)	
		self diffusion boundary	self diffusion volume
Pb	601	0.66	1.09
Nb	2742	2.7	3.3
Al	933	0.84	1.42
Ni	1726	1.15	2.84

Generally, thin films have a small grain size and grain boundary diffusion predominates over volume diffusion [74]. It is therefore more likely that atomic depletion will occur in highly granular structures than in single crystals, and consequently, failures will develop more quickly in polycrystalline structures (i.e. the more grain boundaries present, the more atoms can be transported along them, and the shorter the failure time). Nevertheless,

if the width of a granular stripe is smaller than the average grain size, EM failures cannot occur. This situation is depicted in Figure 3.5, the structure's width w is larger than the average grain size, allowing triple-points†, to develop at grain boundaries, thereby encouraging atom diffusion. Compared to this, when the width is reduced the structure

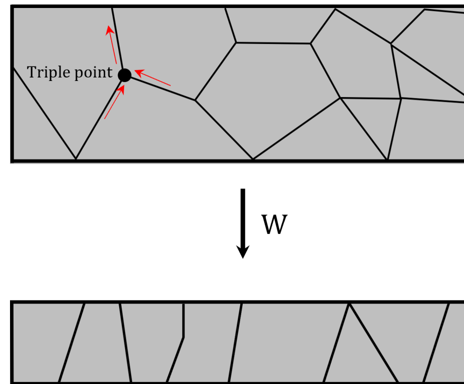

Figure 3.5: **The effect of junction width on EM compared to average grain size.** When the width of the junction is greater than the average grain size, the presence of triple points facilitates atomic diffusion, allowing a net flux along the junction. However, when the grain width is reduced, the grain boundaries tend to be in the opposite direction of the current flow, impeding the EM process.

behaves as near-bamboo or bamboo-type structures thereby have fewer grain boundaries which tends not to be in the direction of the current flow, thereby impeding EM process. Several effects of the internal microstructure have been investigated by several researchers, as presented in Refs. [75] and [76], being a very important feature which may also be taken into account for understanding the atomic diffusion.

3.5 Electromigration control process

Control process might be challenging due to the stochastic character of the EM. It is difficult to maintain appropriate current densities throughout the operation and frequently software-controlled feedback loops and incremental adjustments are required. The last decade have seen a rapid shift from studies that first concentrated on EM prevention to those that seek to control and make use of this phenomenon [44]. Regardless of the desired outcome, the majority of reports mention relatively similar types of sample layouts and EM control techniques. It is evident that EM depends on current density, as shown in Equation 3.8 and by the Black law (3.13). In order to trigger EM, we propose to introduce a constriction where current crowding will greatly favor it and ensure that it will be

†Triple points are locations where grain boundaries split, allowing one grain boundary to travel in one direction as two do in the opposite direction, or vice-versa.

likely triggered in its vicinity. It is for this reason that most layouts include geometrically constrained partitions such as bow-ties, Dayem bridges and similar structures [36, 37, 77, 78].

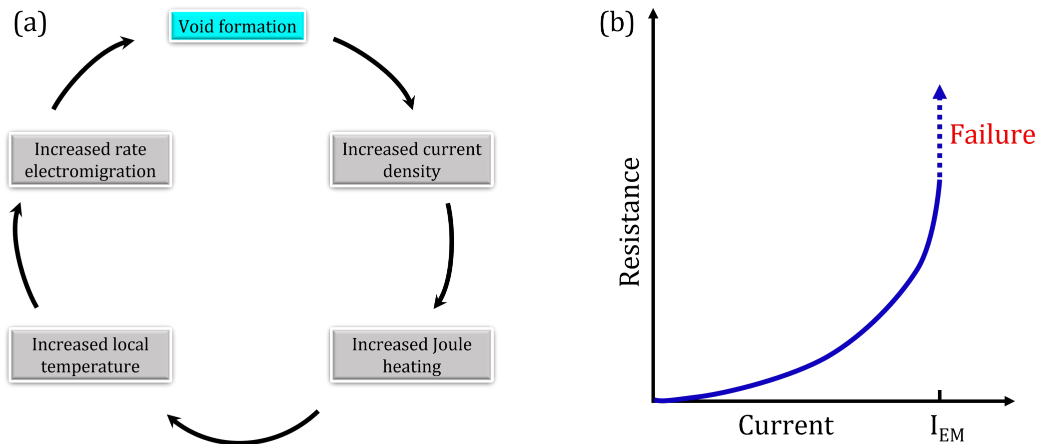

Figure 3.6: **Characteristic of uncontrolled EM.** (a) A schematic representation of the feedback loop in EM: void growth increases current density, which in turn rises the metal temperature due to Joule heating, which further accelerates diffusion and void formation. (b) Typical evolution of the resistance with the applied current: as a result of the Joule heating effect, the resistance grows nearly quadratically until electromigration is triggered at a critical current I_{EM}. Thereafter, the resistance rises very rapidly, indicating failure.

If we merely take the diffusion brought on by EM into account, the emergence of a void is the first step in a series of processes that will ultimately result in the junction failing. Depletion of atoms in a metallic stripe does, in fact, imply a local reduction in the cross-section of the stripe. The local resistance increases as a result, leading to more Joule heating. In addition to this, the local current density increases as well. Thus, all prerequisites for the emergence of fresh voids are satisfied. EM's damaging nature is mostly caused by this positive feedback loop, which is depicted by the black arrows in Figure 3.6, and it needs to be stopped. Establishing a critical conductance value at which the process is to be stopped is one strategy that has been implemented and used over the years. The core of this controlled EM process is a home-made piece of software that teams at Nanoscale Superconductivity and Magnetism group (NSM, KULeuven, Belgium) and Experimental Physics of Nanostructured Materials (EPNM, ULiège, Belgium) have been working on for years. A joint publication was made of the most complete version [40]. An alternative method for controlling EM is by electropulsing, which eliminates the need for expensive and complicated feedback loops. This method entails applying voltage pulses of magnitude similar to that needed to reach the critical current density of the virgin structure during a short period of time. As part of this controlled EM procedure, Stefan

Marinkovic (member of EPNM) developed a software package, which is employed in the experimental sections of this thesis and will be discussed in more detail in the following chapter.

Chapter 4

Experimental techniques

This chapter provides an overview of all relevant samples studied in this thesis as well as the description of the major experimental techniques that were employed to prepare and characterize the samples. Nb samples were fabricated using facilities at the EPNM, ULiege, Belgium, whereas the Al and Ni samples were fabricated in the facilities available to Dr Melinte's group at ICTEAM*, UCLouvain, Belgium. The samples were patterned using electron beam lithography (EBL) and photolithography, and the subsequent deposition was carried out using the physical vapor deposition (PVD) procedure (RF-magnetron sputtering and/or electron beam evaporation). Experimental data were obtained either in the facilities of EPNM, (single- and multi-terminal transport, Atomic Force Microscopy, Scanning Electron Microscopy) and at KULeuven, Belgium (Kelvin-probe force microscopy).

*Institute of Information and Communication Technologies, Electronics and Applied Mathematics at Université Catholique de Louvain.

4.1 Sample layout

The samples used in this work were made of Niobium (Nb), Aluminum (Al), and Nickel (Ni). For the Nb, resist patterns consisting of a double copolymer methyl metacrylate (PMMA/MA) and polymethyl metacrylate (PMMA) layers were prepared by electron beam lithography on a Si/SiO_2 substrate using the nanofabrication system Pioneer 2 from Raith GmbH. More information about the system will be provided later in the chapter. Figure 4.1 depicts the sample layout in which a central transport bridge 2 μm wide is linked by 10 terminals symmetrically placed with respect to the central axis of the bridge. All 10 terminals are (1.25 $\pm$ 0.05) μm wide at the point of contact with the bridge and since this is the narrowest point along the current path they can therefore be regarded as junctions. The upper row of junctions (labelled from 1 to 5) form different angles from the central axis of the bridge.

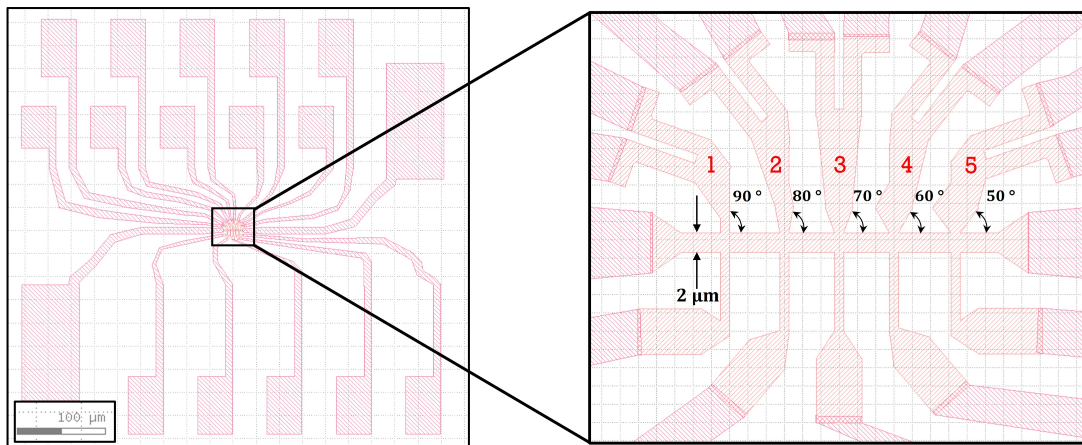

Figure 4.1: **Overview of the investigated sample.** Illustration of the complete sample layout of Nb multiterminal transport bridge.

The Al and Ni layout consists of three constrictions connected in series where the central bridge has a width of 2 μm whereas the outer ones have 4 μm. All constrictions are accessible from both sides with contact pads (eight pads with 200 μm $\times$ 275 μm, and two pads with 340 μm $\times$ 780 μm). A complete layout of this device is shown in Figure 4.2. The films are patterned by conventional photolithography and lift-off procedure using both negative (for constrictions) and positive (contact pads) photoresist onto a Si/SiO_2 wafer. Subsequently, Al or Ni thin films are deposited using electron-beam evaporation. EM is reliant on current density, as we have already observed from Equations 3.8 and 3.13. Taking this into account, we attempt to introduce a constriction where current crowding (i.e., large current densities) will substantially favor EM and ensure that it will be likely

triggered in its vicinity. For this reason, the majority of layouts include geometrically constricted partitions such as bow-ties, Dayem bridges or similar structures [79–82].

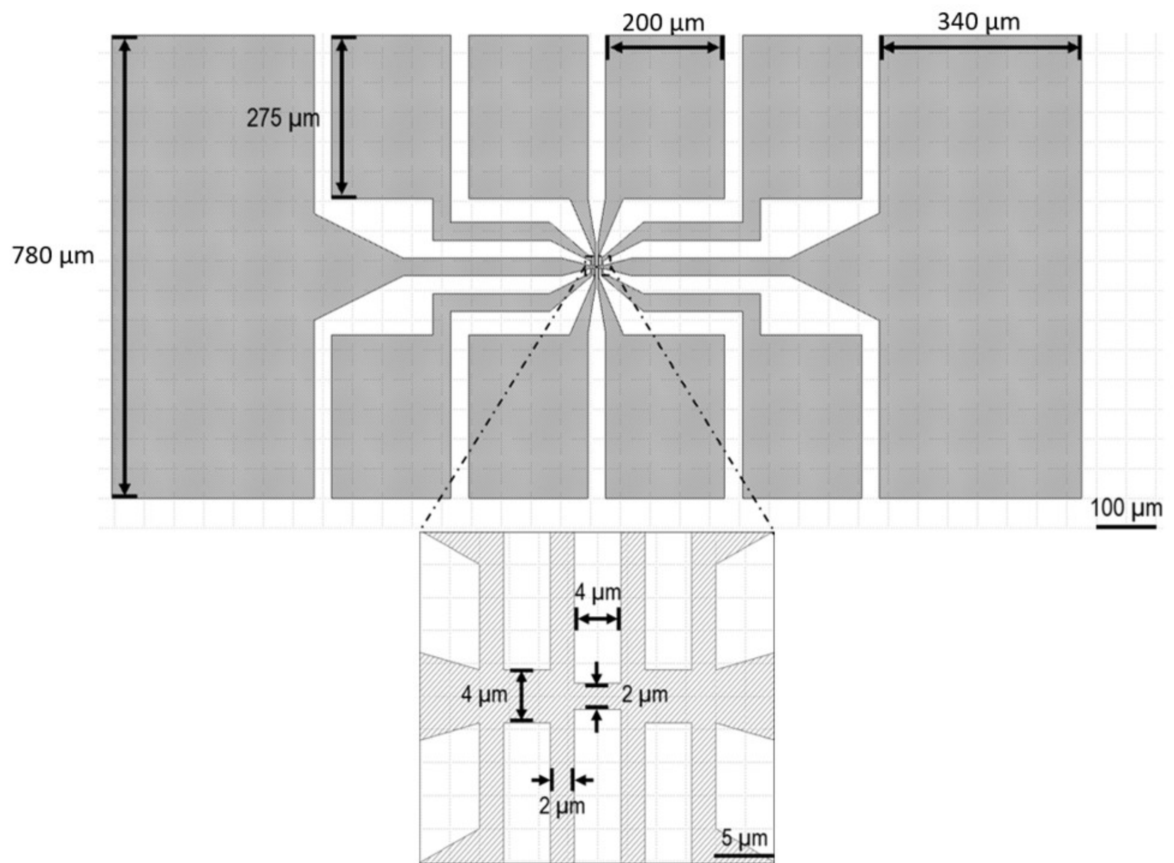

Figure 4.2: **Schematic of the triple constriction.** A single device is shown in the top panel and a zoomed up view the constriction is displayed in the bottom panel.

4.2 The art of lithography

Lithography is the process of imprinting a design (a pattern) onto a reactive polymer film, also known as a resist, which is then used to replicate that pattern onto an underlying thin film. Lithography is a broad term for several closely related processes such as coating, exposure, and resist development. Since there is a wealth of literature on the fundamental lithography processes, the use of lithographic techniques to produce micro- and nanoscale features is well established [83, 84]. However, a brief review will help to better illustrate the more sophisticated techniques used in this thesis.

4.2.1 Electron Beam Lithography

Electron Beam Lithography is a well-developed technique that emerged from a controllable electron beam emitted by a SEM and is one of the most important tools for making ultra-small structures with high quality and a manageable writing speed [85, 86].

High-energy electron interactions with organic materials are the foundation of the EBL. An electron beam interacts with polymeric materials primarily by inelastic scattering, which has the potential to permanently alter the polymeric chains. The sensitive polymers designed specifically for EBL are referred to as *e-beam resists*, and their purpose is to serve as a resist mask, generating structures that are then transferred to the sample. E-beam resists (and others) come in two types: positive and negative. When a positive resist is used, the e-beam permanently breaks chemical bonds and transfer the exposed polymer into fragments of lower molecular weight. Following that, an organic solvent, known as *developer*, is used to wash away the lower molecular weight fragments in a process known as *development*. These layers removed during the development process correspond to the predefined pattern, leaving the substrate exposed. When a negative resist is used, the polymer becomes cross-linked as a result of the interaction with the energetic electrons. The developer removes the unexposed resist in this case. In essence, the e-beam modifies the original structure of the sensitive polymer in both cases, and as a result, the exposed parts have different properties than the unexposed polymer [87].

4.2.2 Photolithography

Photolithography is a microfabrication process for patterning parts on a thin film or on a substrate such as silicon wafers. It transfers a geometric pattern from a photomask

to a photosensitive chemical photoresist placed on the substrate using light [87]. After that, a series of chemical treatments either etches the exposed pattern into the material or allows the deposition of a new material in the desired pattern onto the material beneath the photoresist. These patterned films typically protect selected areas of the underlying substrate during subsequent processing, such as etching or metal deposition. The ability to manipulate feature dimensions[†] with exceptional precision allows photolithography to produce patterns with features as small as a few tens of nanometers. In addition, photolithography is relatively quick and may be able to create patterns throughout an entire silicon wafer at an affordable cost.

4.3 Fabrication processes

The first part of this section discusses the method used to create the Nb multiterminal devices, while the second part demonstrates how to pattern a triple constriction on 100-nm-thick SiO_2 on Si wafers via lift-off.

4.3.1 Nb multiterminal

As previously mentioned, Nb samples were fabricated at the EPNM (ULiège) facilities by EBL method employing scanning electron microscope equipped with the nanofabrication system Pioneer 2 from Raith GmbH. With the Pioneer 2, a software program is available which automates the electron beam exposure of micro- and nanostructures with the appropriate dose based on previously calibrated graphical data files. A high degree of resolution is achieved by the use of high performance laser interferometers and an in-lens detector. An integrated overlay procedure allows for the creation of patterns in several steps, for example, to create multilayered structures or planar heterojunctions.

To begin, a bare Si/SiO_2 substrate is coated with a PMMA and a coPMMA independent layers via spin coating. This is followed by a soft baking at 180°C to evaporate the solvent and fix the polymeric resist. Figure 4.3(a) depicts a schematic illustration of the double resist coating process. Next, the PMMA/coPMMA-covered substrate is placed in the chamber of the EBL platform. The regulated electron beam then exposes the resist in a specified pattern, resulting in a change in solubility for the irradiated portions (color change

[†]This is often referred to as the critical dimension (CD), which is the smallest part of the design. The CD that can be achieved relies on the lithography technique and surface topology that you are patterning on.

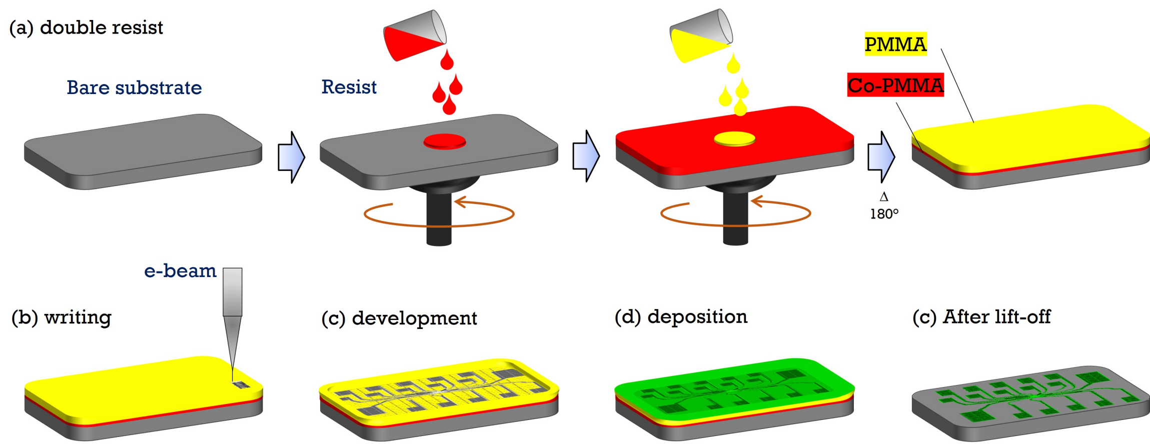

Figure 4.3: **Process flow of the e-beam lithographic procedure.** (a) A double resist layer is spin-coated on the substrate. (b) An electron beam is used to imprint the desired structures in the resist layers, inducing changes of their physical properties of the exposed area. (c) After that, it was placed in a chemical solution to remove the exposed resist (development). (d) Deposition of the material onto the resist layers and substrate. (e) Finally, the surplus material is removed chemically by removing the resist (lift-off). After the lift-off procedure, the final patterned film is reached.

in Figure 4.3(b)) due to polymeric chain breaking. In the following step, the weakened sections of the resist are removed (positive resist) by immersing it in methyl isobutyl ketone (MIBK) diluted in isopropyl alcohol (IPA). This development phase is illustrated in Figure 4.3(c). The obtained resist mask is placed, ready for metallisation, in an evaporation chamber. The Nb thin film ($\sim$ 50 nm) is deposited using radio-frequency magnetron sputtering in the chamber previously pumped down to 10^{-8} mbar (base pressure) with a deposition rate of 1 Å/s at an Ar pressure of 5.3 mbar (working pressure). Without breaking the vacuum, the sample was then capped with a 7-nm-thick Al layer by electron beam evaporation (Figure 4.3(d)). The thickness of the Al capping layer has been chosen to be slightly thicker than the native oxide layer of Al [88], so it acts as a protective layer for Nb. The final structure is revealed after conventional lift-off process in warm acetone. The remaining portion of resist and the Nb/Al covering it are removed, leaving only the metallic parts that were directly in contact with the substrate. This last step is referred to as the lift-off and is illustrated in Figure 4.3(e) resulting in the desired device.

4.3.2 Al and Ni constriction (plain layers)

The present section shows the procedure to pattern a triple constriction on 100-nm-thick SiO_2 on Si wafers via lift-off. Figure 4.4 summarizes the procedure carried out to pattern the constrictions based on the metals Al and Ni. Details of each process are explained ahead.

To make the desired patterns, the Si/SiO_2 substrates were firstly cleaned to remove particulate matters on the surface as well as any other traces of impurities. The substrates are treated in piranha solution (a mixture of concentrated sulfuric acid and hydrogen peroxide in a ratio of 5:2 in volume) for 10 minutes at 110°C, then a rinse with deionized water (DIW) for few times and then dried in N_2. After cleaning, the substrates were treated with hexamethyldisilazane (HMDS) at low pressure, followed by spin-coating a layer of negative photoresist (nLOF 5510, MicroChemicals) at 3000 rpm for 30 seconds. The photoresist-coated substrate was then *prebaked* on a hot plate at 90°C for 60 s before being used. The photoresist was exposed through the photomask using standard contact mode optical photolithography under ultraviolet light for 30 seconds. A brief post-exposure bake was performed using a hot plate at 110°C for 60 seconds before developing. Then the baked substrates are developed manually by soaking in the developer solution (AZ 726 MIF, MicroChemicals) for 20 seconds, then rinsing with DIW and drying with N_2 blow. The substrates were loaded with patterned side facing down, being metalized via e-beam vapor deposition with an E-gun Vacotec, and were organized into two batches. For the first batch, 30-nm-thick Al layers were deposited with a deposition rate of 1 Å/s and base pressure in the chamber of 1.8×10^{-7} mbar. In the second one, a 5-nm-thick Cr layer was used as an adhesion layer prior to 25-nm-thick Ni deposition (deposition rate: 1 Å/s). The deposition was followed by a lift-off process. The samples are soaked vertically in 800 ml of warm acetone at 60°C for 2 h. Upon the metal layer is delaminated, the samples are taken out and rinsed with a constant flow of acetone and IPA to remove the macro residues of metal. After, the samples are soaked in hot 1-Methyl-2-pyrrolidone (NMP) at 140°C for 10 minutes and rinsed with IPA. Then the samples are dried using nitrogen gas blow.

Contact pads fabrication

A positive photoresist (AZ MIR 701, Micro Chemicals) was spin-coated at 3000 rpm and baked for 60 seconds at 100°C. Prior to this, the batch underwent HMDS treatment at low pressure (this improves the photoresist). The photoresist layer was brought into contact with a photomask containing the patterns of contact pads and subjected to ultraviolet light for 20 seconds. The photoresist and wafer was then baked at 110°C for 60 seconds. Following that, the baked Si wafer is manually developed by soaking in developer solution (AZ 726 MIF, MicroChemicals) for 20 seconds, followed by rinsing with DIW and drying

with N_2 blow. Following the photolithography procedures, 200-nm-thick Al was deposited on the patterned resist using e-beam at a deposition rate of 1 Å/s with a chamber pressure of 1.8×10^{-7} mbar. Finally, the samples are soaked in 50 ml NMP at 160°C for 10 minutes (3 times), and then, rinsed with IPA and dried with N_2 blow. These steps were also depicted in Figure 4.4.

4.3.3 Al constriction fabricated on nanoholey layers

This section demonstrates how to pattern a triple constriction on 100-nm-thick SiO_2 on Si wafers via dry etching process to obtain samples decorated with arrays of nanoholes. The EM results about these devices are presented in Appendix A.

Nanoholey layer

A summary of the steps taken to create a nanoholey metal layer is shown in Figure 4.5. Al has been employed in this instance as the metallic layer of interest to electromigration studies.

To begin with, a SiO_2/Si wafer was cleaned using piranha solution for 10 minutes at 110°C, followed by DIW rinsing for 5 times and dried with nitrogen gas blow. The edges of the SiO_2/Si wafer (polished side) are then covered with blue tape‡, leaving a square of 4×4 cm^2 at the center (active zone). In order to make the surface of the Si wafers hydrophilic,

‡With the blue tape, the self-assembled layer can remain stable during the drying, otherwise, the layer breaks.

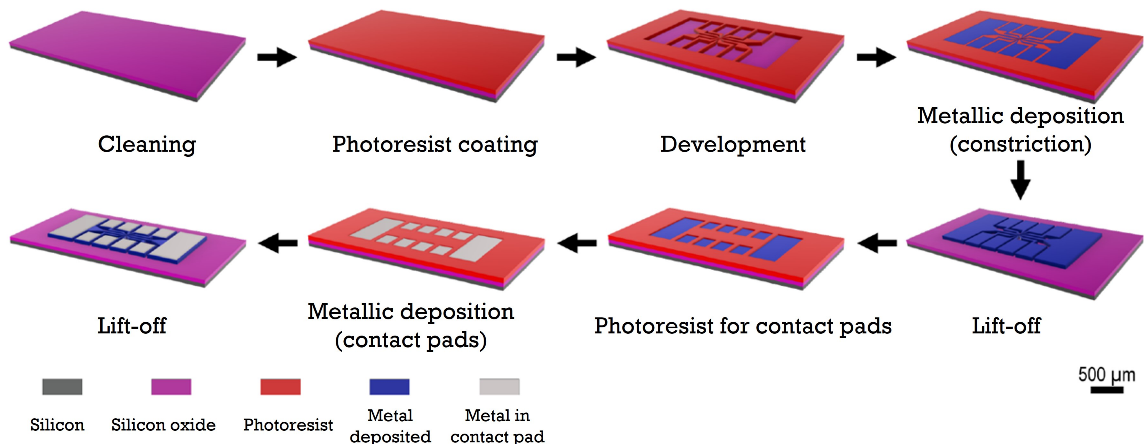

Figure 4.4: **Process flow for the fabrication of Al and Ni constrictions.** Scalable fabrication of constrictions based on regular metal layer (lift-off) and by stepping-up contacts for wire bonding via lift-off. Scale bar: 500 μm.

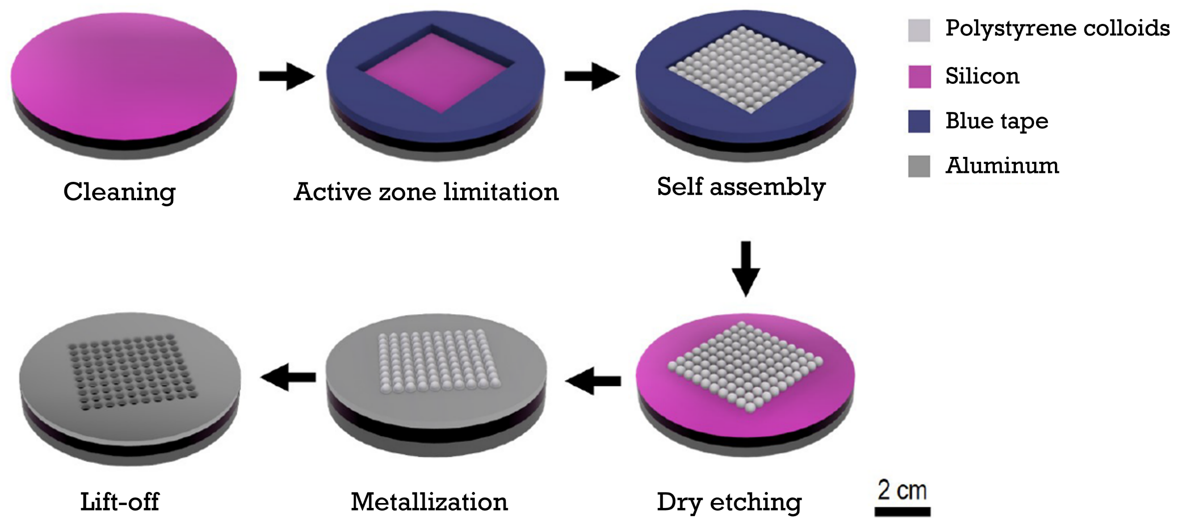

Figure 4.5: **Scalable fabrication of constrictions decorated with nanoholey arrays.** Schematic of the nanoporous material fabrication procedure to be electromigrated.

the wafers are then treated with oxygen plasma in plasma asher (K1050X,Emitech) for 120 seconds. In a small glass, a mixture of styrene (90 μl), Polystyrene (PS) colloids (30 μl) and 30 μl H_2SO_4 solution was ultrasonicated at room temperature for 5 seconds. A glass pipette is then used to prepare the PS self-assembly on the water/air interface in a glass Petri dish by employing the protocol developed by Jian-Tao Zhang, presented in Ref.[89]. Using Triton X-100 in DIW as surfactant, it was possible to compact the colloids in a floating monolayer. The floating colloidal monolayer is then transferred onto the 16 cm^2 at the SiO_2 side by first placing the Si wafer underneath it and then lifting it up. The substrate is then placed on a wipe for 4 hours to dry at room temperature. Following the removal of the blue tape, the wafer is treated with oxygen plasma dry etching to reduce the size of PS colloids (Plasmalab 100, Oxford). Subsequently, a 30-nm-thick Al film was deposited utilizing e-beam evaporation at a deposition rate of 2 Å/s and a chamber pressure of less than 10^{-7} mbar. Following the deposition, the colloidal PS spheres were removed by pressing a tape on the samples. It is then rinsed with IPA and dried with N_2 flow. After lift-off of PS colloids, a nanoholey layer is formed.

Nanoholey layer patterning

The patterning process for the previously constructed nanoholey layer is shown in this section. Both wet and dry etching can be used in this situation to remove the metal. Figure 4.6 shows the many stages of this process.

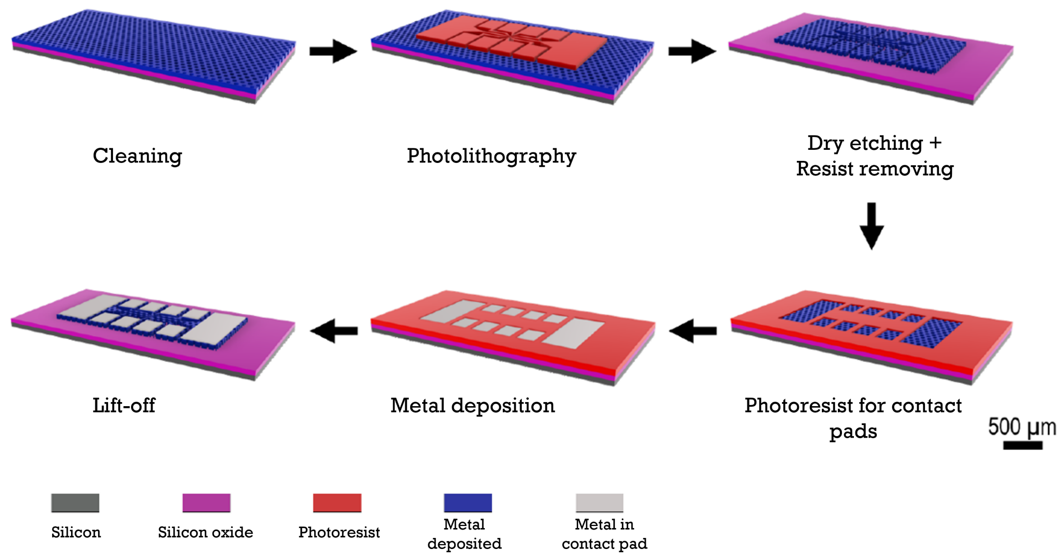

Figure 4.6: **Process flow for the fabrication of Al layers by dry etching.** Scalable fabrication of constrictions based on nanoholey Al layers by dry etching followed by photolithography and lift-off to step up the contacts for wire bonding.

A positive photoresist (AZ MIR 701, MicroChemicals) was spin coated on the Si wafers at 3000 rpm. In order to improve the photoresist, the batch had previously been subjected to a low-pressure HMDS treatment. A hot plate was used to bake the coated Si wafers for 60 seconds at 100°C. For 30 seconds, typical contact mode optical photolithography was used to expose the photoresist through the photomask. After that, a hot plate was used to bake the exposed Si wafers for 60 seconds at 110°C. The baked Si wafers were soaked twice in developer solution (AZ 726 MIF, MicroChemicals) for 40 seconds and 10 seconds in new solution. The step is made manually. Afterwards, using a hot plate, the developed Si wafers were baked for 120 seconds at 120°C. Then, using a chlorine-based method, plasma etching was done in an ICP-RIE (210IL, Corial). Photoresist was finally removed using plasma stripper (300E, TePla). Then, the final shape of the sample is obtained. As a final step, the contact pads are made as described in Subsection 4.3.2.

Summary of the fabrication process

This section summarizes the fabrication process. For completeness, it should be mentioned that Bismuth (Bi) samples were created and investigated, but the outcomes are not discussed in this thesis.

Three Si wafers were patterned with constrictions based on plain Al with thickness of 30 nm. The constrictions goes down from (3.91 $\pm$ 0.11) μm to (1.90 $\pm$ 0.1) μm. The size for

the big contact pads was 354 μm $\times$ 780 μm and for the smaller ones was 199 μm $\times$ 275 μm. For the case of Ni, a batch was patterned with the constrictions based on plain layers with total 30 nm thickness. Here 5-nm-thick Cr was used as an adhesion layer prior to 25-nm-thick Ni deposition. The constriction goes down from 3.8 μm to 1.8 μm. Al constrictions based on nanoholey metal layers were made possible by first preparing a self-assembly PS colloids followed by dry ecthing. Following the lithography process, an Al layer of 30-nm-thick is deposited on the device. Then, a second lithography and metal deposition of 200-nm-thick Al provided the contact pads. See Table 4.1.

Table 4.1: Summary of the fabrication for triple constriction patterning.

Device	Self -assembly PS colloids	Lithography "metal" layer	Metal deposition and lift-off for constrictions	Lithography contact pads	Metal deposition and lift-off for contact pads
Al		X	X	X	X
Ni		X	X	X	X
Bi		X	X	X	X
Al nanoholey	X	X	X	X	X

4.4 Imaging and sample characterization

A variety of imaging techniques, such as scanning electron, atomic force, and Kelvin-probe force microscopies, were used to evaluate sample quality and electromigration effects. A brief description of these techniques will be presented in the following.

4.4.1 Scanning Electron Microscopy

Scanning electron microscopy (SEM) is used before and after electromigration to obtain high resolution information about the investigated devices. To that purpose, the measurements were performed at the EPNM group's Raith Pioneer Two Electron Beam Lithography System. It is equipped with multiple detector lenses, an electron gun with acceleration voltages of up to 30 kV that can be used to apply probing currents ranging from 3 pA to 20 nA.

In this technique, an electron beam is accelerated by a potential difference of some dozens of kilovolts using a gun equipped with an electron source of tungsten. This beam is focused by electromagnetic lenses and scans the sample surface with the aid of deflecting coils [90]. The acquisition of signals produced by primary beam electrons and specimen interactions is required for image generation in the SEM. These interactions are classified into two types: elastic and inelastic interactions. Elastic scattering is caused by

the incident electron being deflected by the specimen's atomic nucleus or by outer shell electrons of similar energy. This type of interaction is distinguished by little energy loss and a wide-angle directional change of the scattered electron. Backscattered electrons (BSE) are incident electrons that are elastically dispersed via an angle greater than 90°

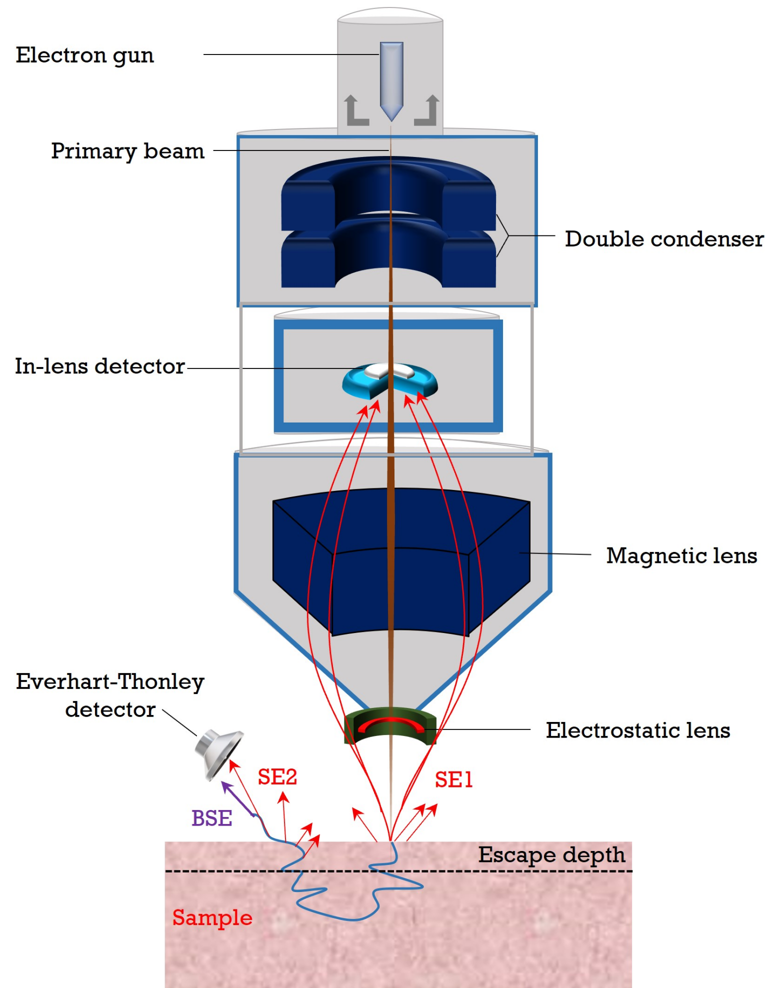

Figure 4.7: **Diagram showing the major components of the SEM as well as an illustration of the sample-electron beam interaction during SEM experiment.** Secondary electrons (SE) are generated by beam electrons entering the sample surface in a droplet shaped volume whose cross section defines the footprint of the beam and whose height defines the escape depth of the SE. Due to the shallow scale of their origin, these entrance surface SE, designated the SE1 class, retain the lateral spatial resolution information defined by the dimensions of the focused beam. They are similarly sensitive to the properties of the near surface region. SE1 have relatively high energy and are detected with the in-lens detector. During the course of moving deeper into the sample, the primary electron beams continue to generate SE, but these SE rapidly lose their small initial kinetic energy and are completely reabsorbed within a very short period of time. Those electrons that undergo enough scattering to return to the entrance surface and emerge as backscattered electrons will continue to produce SE as they approach the surface region, thus increasing the total production of SE. They are classified as SE2. Everhart-Thornley detector is used to collect the lower energy SE2 emitted after scattering of a backscattered electrons on its way out of the sample.

and produce a useful signal for imaging the material. Inelastic scattering happens as a result of a number of interactions between incident electrons and sample electrons and atoms, resulting in the transfer of a significant amount of energy from the primary electron beam. The quantity of energy lost depends on whether the specimen electrons are excited singly or collectively, as well as the electron's binding energy to the atom. As a result of the excitation of the specimen electrons during the ionization of the specimen atoms, SE are generated, which are typically described as having energies less than 50 eV and can be used to scan or study the sample. Images can be created by collecting secondary electrons from each small area on the specimen that has been scanned. The intensity of each point is determined by the number of electrons arriving at the detector [87].

The microscope Pioneer Two comes with two SE detectors. In-lens is a primary detector that is placed within the lens with the primary electron beam and captures secondary electrons that are emitted with relatively high energy (SE1) from initial forward scattering events. Despite its limited volumetric depth, the in-lens detector is well suited for imaging the surface of samples. An additional detector, so-called Everhart-Thornley (ET) is located outside the in-lens for the collection of secondary electrons of lower energy (SE2) [87]. These are electrons released near the surface as a result of the scattering of a backscattered primary electron (BSE). The volumetric information about the sample can be retrieved using the ET detector. Figure 4.7 provides a simplified illustration of the scanning electron working principle of a scanning microscope.

4.4.2 Atomic Force Microscopy

Atomic Force Microscopy (AFM) investigations were carried out at the EPNM laboratory. The equipment employed was a Bruker Nanoscope V Multimode SPM, which included three major elements, as shown in Figure 4.8 and described ahead.

- **Bruker Nanoscope V** composed of a tip, the tip holder, the laser, the cantilever, the photodiode;
- **Optical microscope** that takes image of the cantilever. This part serves for the tuning of the laser position and can also be used to provide a rough estimation of the distance between the tip and the sample;
- **Computer** running the control softwares.

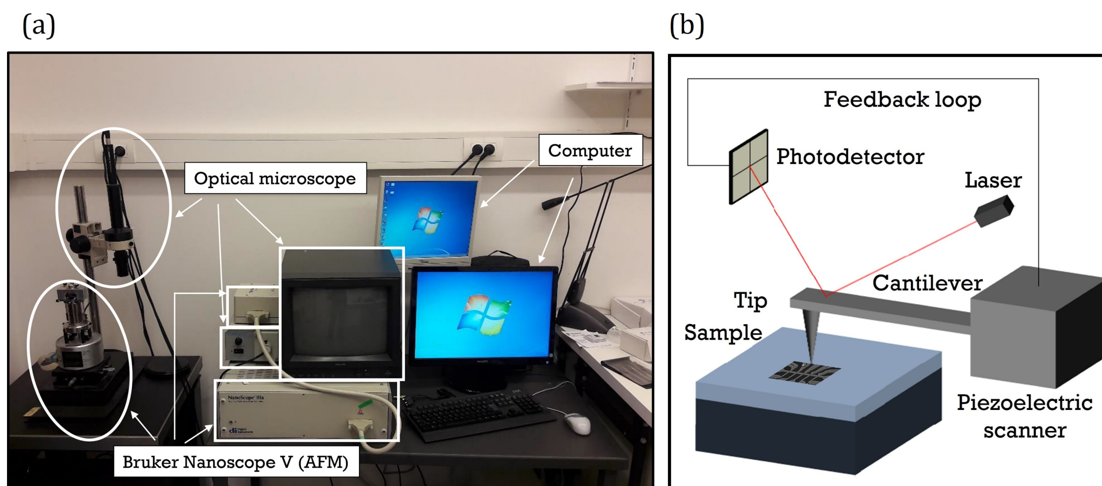

Figure 4.8: **Overview of the main parts of the system of the EPNM facility at ULiège.** (a) Photograph of the bench containing the three principal parts of the AFM. (b) A schematic illustration of the main components of the Bruker Nanoscope V.

AFM is a scanning probe microscopy (SPM) which allows the analysis of a sample by probing the force of interaction between a nanometric tip and the surface of the sample. For basic AFM, Van der Waals interaction are probed to image the surface of the sample. It allows one to obtain information on the topography of the surface, its roughness, the grain size, etc. The system is composed of a tip, fixed at the extremity of a cantilever. The position is controlled by electronics via a piezoelectric scanner. To maintain a constant distance between the tip and the surface, the position of the cantilever is monitored using a laser and photodetector. The laser is focused on the cantilever and reflected towards a 4-quadrant photodetector via a mirror. When the cantilever is moving, the intensity of light detected by the four photodetectors will change. The information is transmitted to the electronics that will adapt the position of the scanner and so the cantilever and the tip. In the the tapping mode, the tip taps at high frequency on the surface of the sample while scanning the surface. Variations in amplitude and phase of the oscillation will be probed and this results in a topographical image of the sample.

This microscope was also used to do MFM measurements. It is possible to make the same technique magneto-sensitive by coating the probes with a magnetic layer in order to achieve MFM and recording the magnetic force between the tip and the sample.

4.4.3 Kelvin Probe Force Microscopy

Kelvin-probe force microscopy (KPFM), also called scanning Kelvin probe microscopy is another example of a SPM technique. It has been introduced as a tool to measure the

local contact potential difference between a conducting AFM tip and the sample, thereby mapping the work function or surface potential of the sample with high spatial resolution [91]. Over the last two decades, KPFM has been adapted to two basic scanning modes, single-pass scan and dual-pass lift-up scan. When operating in ambient conditions, the single-pass scan KPFM has a few advantages over the dual-pass lift-up scan KPFM. For instance, the topographical inaccuracies brought on by electrostatic forces are minimized during the simultaneous topographical and KPFM measurement because electrostatic forces are actively suppressed. Additionally, a greater spatial resolution is anticipated, allowing us to map the work function in regions of some micrometers to improve the comprehension about eletromigration process in constrictions.

At the facility of KULeuven, Belgium, single-pass Kelvin probe force microscopy observations were made under ambient conditions on an Agilent Technologies 5500 Scanning Probe Microscope. The apparatus included a conductive platinum silicide tip from NANOSENSORS for force modulation microscopy (PtSi-FM).

4.5 Experimental Electromigration Set-up

In order to measure the resistance of the constriction, all electrical measurements were performed employing a technique similar to the four point probe measuring scheme, as illustrated in Figure 4.9(a) and (b). A voltage source is used to apply a current through the constriction (across the outer wires). The resistance of the constriction is monitored during the experiment and the measured data are stored by the computer. Because there is practically no current flowing through the inner wires, very low absolute resistances may be measured easily due to the low noise and overall circuit impedance. In this work, as illustrated by Figure 4.9(c), the main experimental setup for EM comprised of three main parts:

1. A probe station: Cascade MPS15 is used for the EM measurements. The probe station is made up of a coaxial chuck, probe arms with probe needles to touch the sample, and an optical microscope to position the probe needles on the contact pads.

2. A source meter for electrical measurements: the voltage source, the voltage meter, and the current meter are all provided by a single device: the KEITHLEY 2612B. These configurations can be independently selected for two channels. Channel A is used to source a DC current, while channel B serves as a voltmeter.

3. A controlling and monitoring software: EM was controlled by a computer using a special programmable Python code. The algorithm was designed with several desirable characteristics in mind, including real-time monitoring of the constrictions' resistance and data storage from the trials which will be better described ahead.

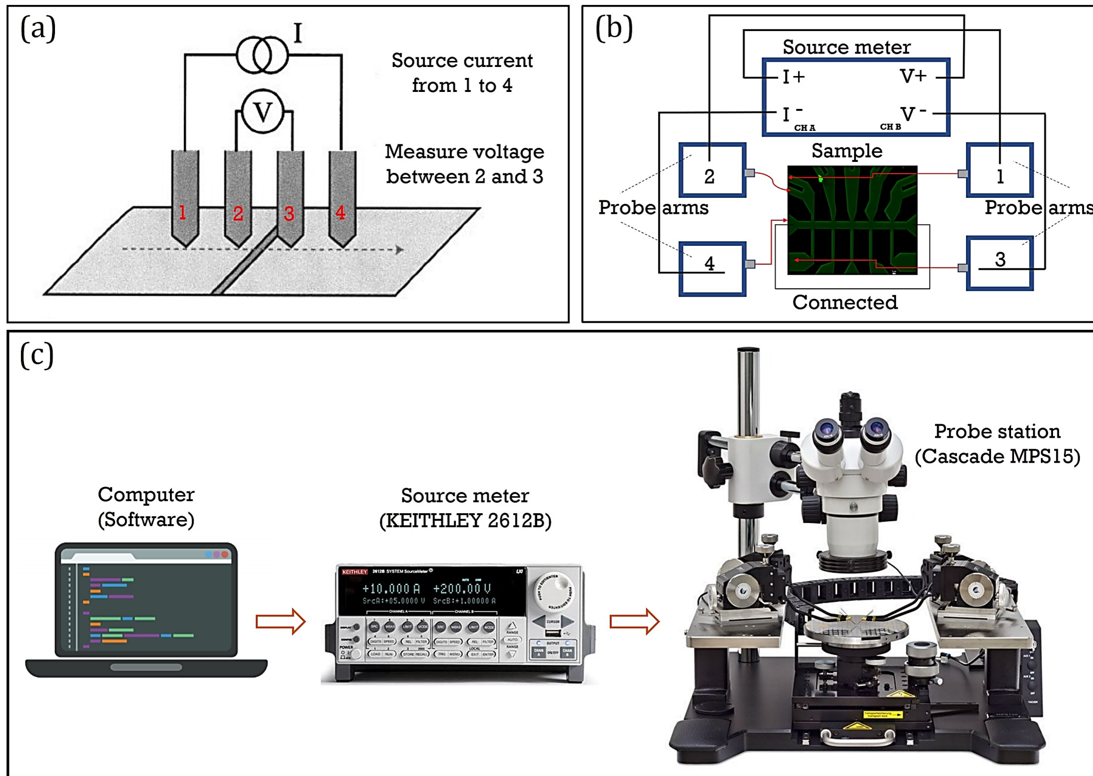

Figure 4.9: **Overview of the main parts of the experimental setup for EM.** (a) Schematic of Four-Point Probe measurement. (b-c) To bias our samples we use a probe station to connect to the sample. We employ the biasing circuit illustrated in (b) and a programmable software to regulate the current supply via computer control. (c) The probe station consists of chuck, probe arms with probe needles to contact the sample, and optical microscope to position the probe needles on the contact pads of the sample.

4.5.1 Sample Handling

Bonding Al wires to the contact pads may be required to complete the indicated measurements. To that goal, the sample is put on a sample holder and electrically attached *via* a procedure known as wirebonding. Because thin film constrictions are designed to be (gradually) broken down by current, they are very vulnerable to electrostatic discharge (ESD). While handling the samples, necessary precautions were taken to avoid uncontrolled electromigration (*i.e.,* breakage). An example of the sample holder is shown in Figure 4.10, which consists of a gold-plated square receptacle mounted on a printed circuit board (PCB). The PCB mount has been designed to fit the bonding platform shown in Figure

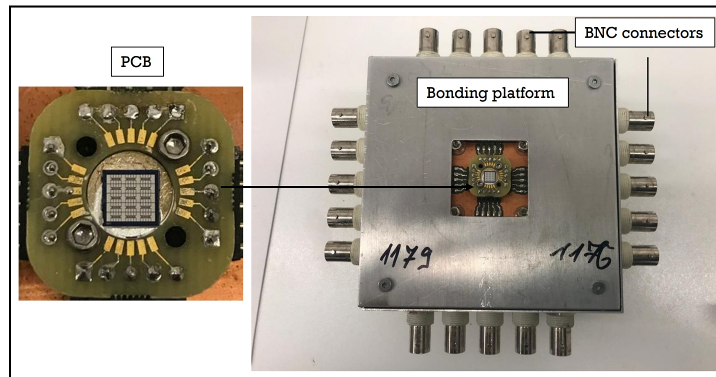

Figure 4.10: **Sample holder and bonding platform.** Sample pasted on the homemade PCB as well as the top view of the bonding platform showing the central area in which the PCB holder is designed to receive the sample.

4.10, which also serves as a storage stage for the sample after bonding. The wirebonder used is an iBond5000 Series from Kulicke and Soffa. It is an innovative graphical user interface mechanical wedge bonder. It can perform wedge bonding on a range of materials using various wire kinds beyond Al, such as Au, Cu, and ribbon, for instance, to better adapt to different materials or contact pads.

4.5.2 Controlled Electromigration Software

It is the EM software, firstly developed in Labview by Zharinov [40] and later adapted and improved by Stefan Marinković [82], which is at the core of the controlled electromigration process. It is written in the Python programming language and is capable of controlling and interacting with devices such as the Keithley 2612B when connected via a GPIB (General Purpose Interface Bus) port.

As we discussed in the previous chapter regarding electromigration, the rate at which this process occurs is dependent upon the temperature and the current density. Simply applying a voltage or current over the junction will result in uncontrolled electromigration due to a continuous positive feedback process, resulting in an exponentially increasing rate of electromigration. Therefore the need for an advanced control algorithm to gradually induce electromigration is prioritized. To that goal, a simple electropulsing mechanism is used to accomplish controlled electromigration, as presented in Figure 4.11. This method entails administering a train of Direct Current (DC) current pulses with linearly increasing amplitudes until a resistance change of 5% is achieved. As a way of extracting the resistance of the sample during EM we apply between the big pulses, small probe pulses of 100 μA which are always of the same amplitude, regardless of their polarity. Keeping this

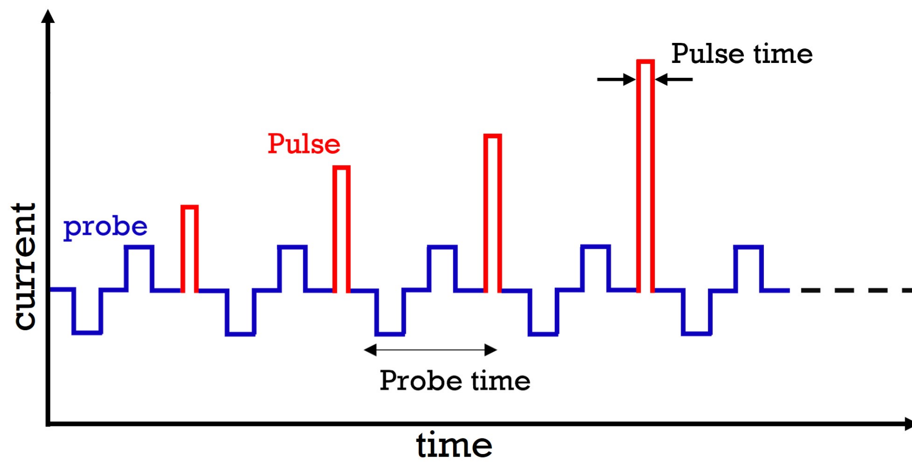

Figure 4.11: **Measurement protocol for controlled electromigration.** A train of current pulses with increasing amplitude is used to electrically excite the sample, and its resistance is measured. Following each pulse, a resistance measurement is taken with a probe current of 100 μA for 10 s in both polarities.

in mind, the software is programmed in such a manner that the prospect of achieving efficient controlled electromigration by electropulsing is made simple, allowing it to be implemented without the need for sophisticated software controlled feedback loops. Python

Figure 4.12: **Graphical User Interface for EM experiments.**

is being widely used to create scripts which cover different necessities in computational scenario. The Python script developed for the electromigration was made successful via GUI (Graphical User Interface) creation using Tkinter§. Tkinter manages the event loop

§Tkinter, or "Tk interface", is a module of Python that provides an interface to Tk GUI toolkit, developed in TCL (Tool Command Language) and multiplatform, with support for Linux, MAC OS and MS Windows.

that receives user actions over the window components, controlled by operating system, like button presses, keystrokes, mouse movement, and window resizing. The primary goals of the interfaces are to accept parameters and regulate the flow of experimental procedures. Parameters can be those required to setup devices, such as a power supplier's current/voltage, parameters to specify the beginning and ending circumstances of each electromigration process, and parameters to monitor the resistance of the constriction in real time. Flow operations involve activities such as starting, pausing, or stopping the experiment. Figure 4.12 is an example of the interface used.

Chapter 5

Current-induced modifications of superconducting Nb multiterminal transport bridges

This chapter is largely based on the publication:

S. Marinković, E. A. Abbey, D. A. D. Chave, S. Collienne, E. Fourneau, L. Jiang, C. Xue, Y. H. Zhou, W. A. Ortiz, M. Motta, N. D. Nguyen, A. Volodin, J. Van de Vondel, A. V. Silhanek. *Effect of moderated electropulsing on Nb multiterminal transport bridges*, Physical Review Applied, **19** 054009 (2023).

5.1 Introduction

Niobium is a material of choice for a variety of superconducting applications, including radio-frequency (RF) accelerator cavities [92–94], quantum interference devices [95–97], Josephson tunnel junctions and weak links [98, 99], superconducting resonators and filters [100–102], quantum bits [103–105], and flexible superconducting transmission lines [106, 107]. The reason behind this privileged position is manifold: it is the single element with the highest superconducting critical temperature, develops stable dielectric oxide coatings (NbO, NbO_2, Nb_2O_5) which protect the superconducting phase, exhibits long-term stability under repeated thermal cycling, can be nanostructured by additive or subtractive lithography, is malleable, ductile, and has low toxicity.

More importantly, the possibility to introduce surface treatments such as thermal etching, electropolishing, annealing in controlled atmosphere, and buffered chemical polishing, allows for further optimization of the properties of Nb, such as low microwave surface resistance desired for boosting the efficiency of RF cavities [108]. Naturally, these procedures are homogeneously applied to the entire sample or device and do not allow for spatial selectivity. An elegant approach able to overcome this limitation has been recently proposed based on local annealing of the sample by combined effects of Joule heating and electromigration [109]. This technique has been successfully implemented to tune the properties of Nb-based superconducting weak links [79], SQUIDs [110], multiterminal junctions [111], and for the fabrication of nanoheaters [112]. In the applications listed above, substantial resistance increase, even beyond the quantum of resistance of 25.8 kΩ, was achieved by severe electromigration and the resulting structural modification as well as possible alloying were amply illustrated and discussed. In contrast to that, the consequences of mild electromigration on Nb has remained largely unexplored so far.

In this work, we provide experimental evidence on the origin of the material properties' modifications induced by electropulsing on Nb/Al. We focus particularly on the low stress regime corresponding to currents slightly above the onset of electroannealing and giving rise to a few percent increase in resistance. The subtle induced change consists in a reduction of the work function in a targeted region likely associated to a local oxidation triggered by thermal effects, although no microstructural modifications are revealed. Comparing the spread and shape of the affected area with thermal maps computed through finite element modelling we are able to conclude that temperatures above ~ 435 K are needed to induce sizable modifications in the material. Several funnel shaped constrictions with

different angles were fabricated to demonstrate the possibility to control the extension of the affected area via geometry. The identification of the key parameters permitting to master the local modifications of Nb constrictions together with the understanding of the material's properties affected by electropulsing are relevant steps needed to achieve in situ superconducting weak links and normal leads, both individually tuned at will.

5.2 Sample and experimental details

Nb multiterminal transport bridges were prepared as described in subsection 4.3.1. Figure 5.1 shows the sample layout in which a 2-μm-wide central transport bridge is connected by ten terminals symmetrically placed with respect to the central axis of the bridge. All ten terminals are (1.25 ± 0.05) μm wide at the point of contact (junction) with the bridge. In order to investigate the possible influence of the junction geometry on the properties of the zone affected by electropulsing, the upper row of junctions labelled from 1 to 5 form different angles (respectively $\theta = 90°$ to $50°$ in steps of $-10°$) from the central axis of the bridge. We consider the complement of this angle to be the funnel angle $90° - \theta$. Junctions in the lower row are intended for the sole purpose of measuring the electric potential drop and will remain unaffected by the electropulsing process.

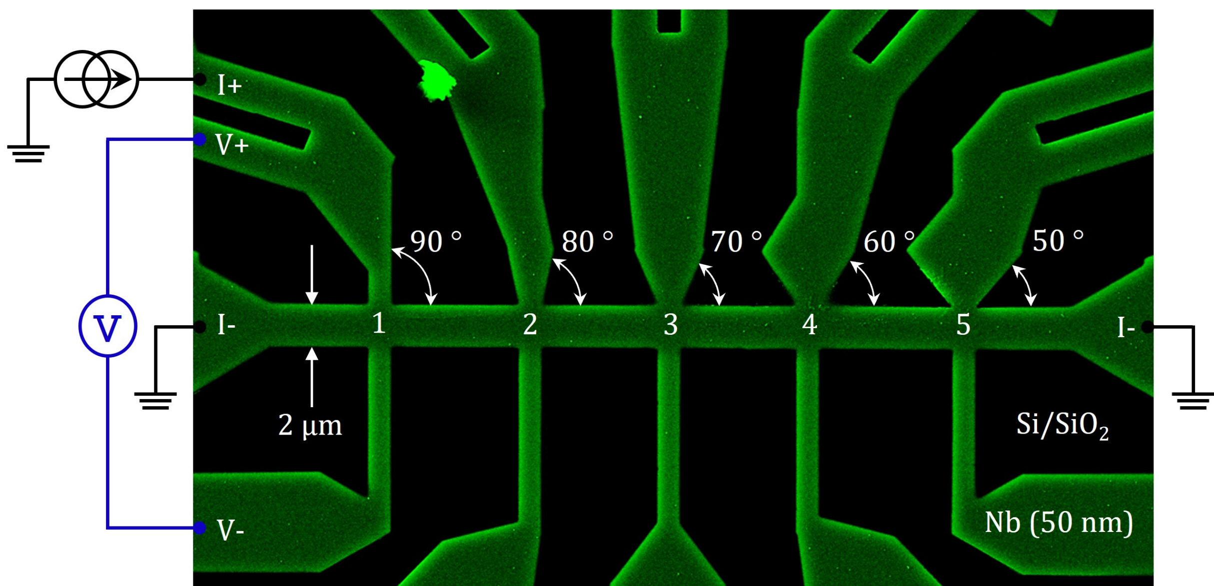

Figure 5.1: **SEM image of a Nb multiterminal transport bridges.** False colored scanning electron microscopy image of one of the Nb multiterminal transport bridges. The circuitry and polarity of the current source are indicated for the case of electropulsing junction 1.

AFM imaging provides a topographic characterization of the specimen surface and allows us to define the dimensions of nanostructures. Thus, a line profile along the white

dashed line of junction 1 obtained by AFM is given by the blue curve in Figure 5.2. From this measurement we can extract a height $h_{Nb} \sim 62\,\text{nm}$ which includes the 7-nm-thick Al capping layer. The red dashed line shows the profile used in the simulations in which the width L_{Nb} has been determined from the SEM image. The numerical simulations will be presented in subsection 5.5. Note that the AFM profile does not show vertical walls. This could in part be attributed to the tip-sample convolution effect [113].

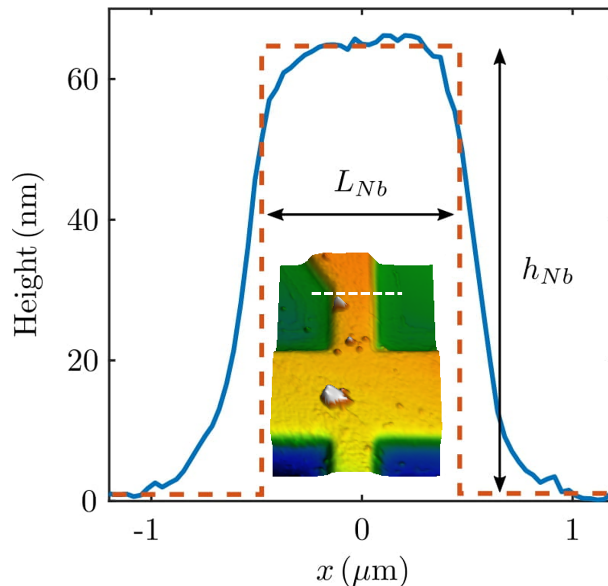

Figure 5.2: **AFM image showing cross-sectional profile of junction 1.** Profile of the cross section of the junction 1 obtained by AFM imaging. The insert shows the junction seen from the top. The profile in the main panel is that of the segment indicated by the white dotted line.

In order to address a particular junction without affecting the neighboring junctions, the current is fed through the upper contact corresponding to that particular junction and the current sink is connected to the left and right extremes of the transport bridge. The voltage drop through the junction is measured between the upper and the opposing lower contact. For the sake of clarity, Figure 5.1 shows the polarity of current source and voltmeter for experiments with junction 1. This strategy has been recently discussed by Collienne *et al.* for the case of strongly modified Nb trijunctions [111]. The samples are contacted by needle probes while excited and probed by a dual-channel source-meter Keithley 2612B. The findings reported in this work were reproduced in five different samples.

5.3 Electropulsing protocol and methodology

As already discussed in previous sections, the electropulsing protocol consists of applying current pulses during 1 s with linearly increasing amplitude. The resistance of the sample is probed during the pulse (R_{max}) as well as in between the pulses (R_{min}) which is the resistance average for applying two opposite pulses of 100 μA. The time between two consecutive electropulses is 25 s. This experiment is performed under ambient conditions. Figure 5.3 shows the resulting evolution of R_{max} (red symbols) and R_{min} (blue symbols) as a function of the pulsed current amplitude for each of the five junctions. The resistance $R_{max}(I)$ initially increases quadratically as a result of Joule heating and a finite temperature coefficient of resistance. At high current amplitudes, a sudden upturn indicates the onset of irreversible changes in the sample due to electropulsing. A more convenient parameter able to separate the irreversible changes operating on the sample from the reversible Joule heating contribution, is R_{min}. Indeed, pulses of small amplitude lead to no modification of R_{min} as manifested by a nearly current independent resistance. Beyond a certain threshold current density, a slight decrease of resistivity is systematically observed. This effect can be linked to structural stress relieved during a mild Joule annealing process. This initial improvement of the sample is followed by a rapid increase of the resistance likely associated to irreversible oxidation of the Nb at the addressed junction. We have limited the excess resistance produced by this process to less than 10 % in each junction.

Note that even though the narrowest constriction of each junction has the same width (~ 1.25 μm), the electropulsing curve is not identical for different junctions. This observation may suggest that the modifications produced on the junctions are not solely dictated by the current crowding at the constriction but its funnel angle plays a role as well. It is also interesting to observe that the maximum current amplitude I_{max} needed to induce the desired resistance increase varies non-monotonically with the funnel angle, maximizing around $60-70°$. This result has been reproduced in three different samples as shown in the inset of Figure 5.3. A plausible explanation for this fact could be the unwanted residual Nb which tends to round the sharp corners in the junctions and which is apparent at intermediate funnel angles, as shown in the AFM images of Figure 5.4. Indeed, it is expected that current crowding in sharp bends [114] will tend to reduce the threshold applied current to trigger the electromigration process.

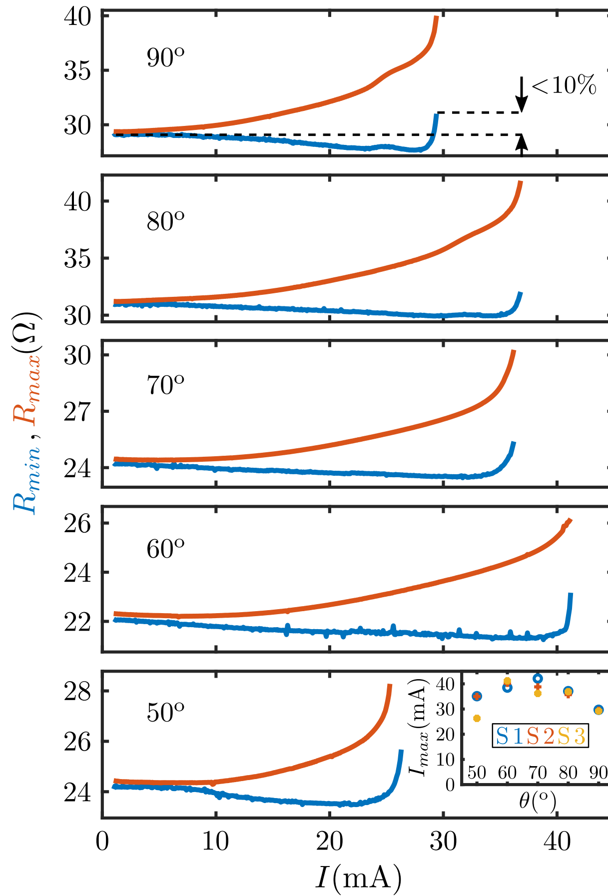

Figure 5.3: **Resistance measured during and after current pulses.** Resistance probed during (R_{max}) and after (R_{min}) a current pulse of amplitude I for the five junction shown in Figure 5.1. The maximum current amplitude is set such that the initial resistance R_{min} increases by less than 10 %. Electropulsing is performed at ambient conditions and reproduced in three different devices, labelled S1, S2, and S3. The inset shows the maximum current I_{max} needed to attain 10 % increase in resistance for the three tested devices.

Following electropulsing, AFM analysis was conducted on all junctions. It is evident from Figure 5.4 that there have been no significant structural modifications. The spikes observed in the AFM images result from residual resist traces after lift-off. Thus, no changes are observed in the nanobridges using this technique.

5.4 Visualization of the induced junction's modification

Let us now analyse the induced modifications at each junction after the electropulsing process described above. To that end we resort to several microscopy inspection techniques including AFM, SEM, and KPFM. AFM measurements (shown in Figure 5.4) do not reveal any structural change after electropulsing. Consistently, no hint of modifications

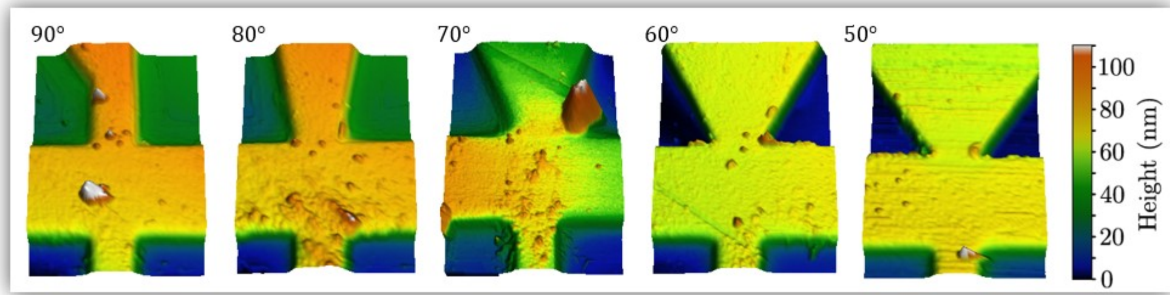

Figure 5.4: **AFM inspection carried out after electropulsing.** After electropulsing, AFM inspection is performed on all junctions. As evidenced by the images obtained, there has been no structural change following electropulsing.

are observed in the SEM images collected by an Everhart-Thornley (ET) detector shown in Figure 5.5(a). This detector collects mainly spatially spread type-2 secondary electrons (SE2) and should be able to reveal nanoscale morphological changes close to the sample's surface. In contrast to that, the in-lens image shown in Figure 5.5(b) evidences a clear change of contrast in the electropulsed junctions. The in-lens detector collects mainly SE1 electrons generated near the upper region of the beam-sample interaction volume and therefore provides direct information on the sample's surface. These images have been acquired with an accelerating voltage of 2 kV which, according to Ref.[115], implies a penetration depth $\sim$ 35 nm of the primary electrons into the Nb/Al bilayer. However, the primary factor determining the emission of secondary electrons (so-called electron yield) is essentially the surface potential (i.e., the work function). Indeed, the fact that the affected regions appear brighter than unaffected parts of the sample, implies a higher electron yield, associated to a lower work function in the affected area. In order to verify this hypothesis, we carried out KPFM measurements shown in Figure 5.5(c). In this image, red (blue) color indicates high (low) work function. There is a close correlation between the areas with high electron yield and those where the work function has been suppressed.

A possible explanation for the observed modification of the sample's surface after electropulsing is local oxidation of the Al capping layer. Indeed, it has been recently shown that the SE emission is directly influenced by the oxidation of the aluminum surface [116]. In particular, for oxide layers thicker than 0.4 nm, the electron emission has been shown to increase (and therefore the work function to decrease). The work function of the oxide layer is also expected to be lower than that of the metallic aluminum [117]. More interestingly, in addition to oxidation, it has been shown that physi- and chemisorption of O and C strongly influence the work function and the secondary electron emission [118,

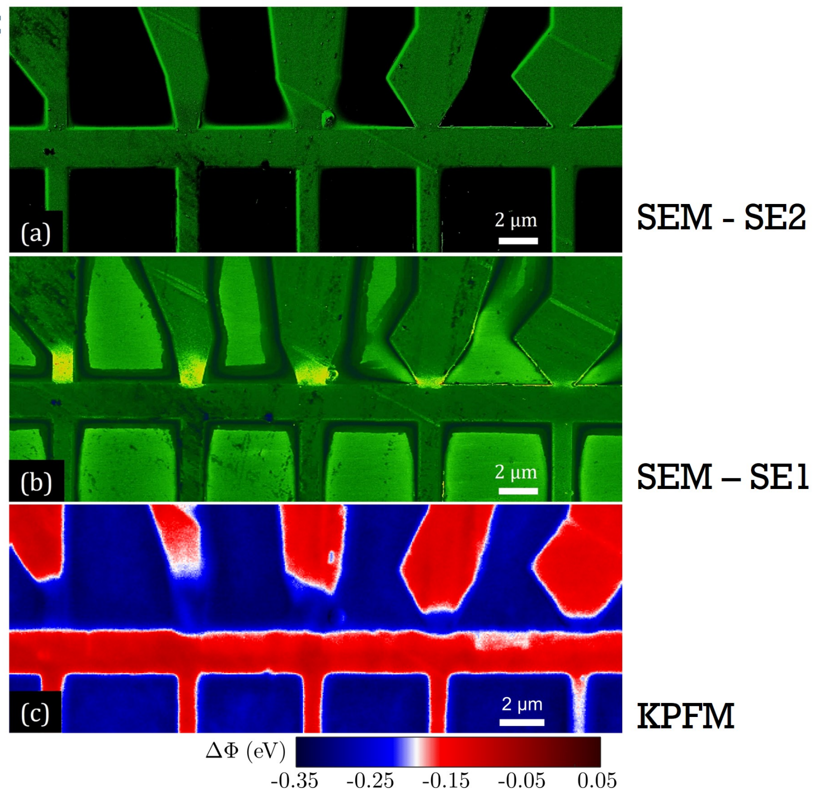

Figure 5.5: **Microscopy inspection of a Nb/Al device after the electropulsing procedure shown in Figure 5.3.** (a) SEM images obtained by ET detector do not reveal any change that could be attributed to the electropulsing process. (b) in-lens SEM image obtained at 2 kV demonstrates higher contrast in the junctions that have been electropulsed. (c) KPFM images of all junctions reveal a lower work function (in blue) in the regions that have been electropulsed.

119]. These experimental findings have been lately confirmed by first-principle studies [120]. This phenomenon may also account for the observed decrease of the work function in the investigated Nb/Al junctions. Another possible explanation would be some alloying at the interface, since a finite solubility (8 at.%Al) exists in the Nb-Al phase diagram. However, according to simulations which will be presented ahead in this thesis, the temperatures achieved during electromigration are much lower than the melting line (>1000°C), being thus unlikely that alloying could occur in a substantial portion of the device.

5.5 Finite element modelling

The oxygen diffusion is assisted by the local increase in temperature during the electropulsing process and therefore, estimating the temperature profile in the junctions is of paramount importance to identify the extension of the affected area. An interesting feature observed in Figure 5.5 is the fact that the affected region shrinks as the funnel angle

increases. In order to understand the origin of this effect, we performed finite-element modelling (FEM) to take into account the exact geometry of the samples from the SEM image analysis. The thickness of the Nb/Al sample of $h = 62$ nm, obtained from AFM imaging (see Figure 5.2), is assumed uniform. Simulations considering a pure 62-nm-thick Nb film or a bilayer Nb(55 nm)/Al(7 nm) give very similar results. The simulation solves the stationary heat equation:

$$\nabla \cdot \mathbf{q} = Q_e, \tag{5.1}$$

where $\mathbf{q} = -k\nabla T$ is the heat flux density in W/m^2 and $Q_e = \rho J^2$ is the local Joule heating, $\mathbf{J} = (1/\rho)\mathbf{E}$ being the current density in A/m^2 and $\mathbf{E} = -\nabla V$ the electric field in V/m. The average thermal conductivity for Nb/Al and Si were assigned to 54 W/(Km) and 130 W/(Km) [121, 122], respectively. The normal-state resistivity $\rho(T)$ of the sample exhibits an approximately linear temperature dependence $\rho(T) = \rho_0(1 + \alpha(T - 300))$, where $\alpha = 2.5 \times 10^{-3}\,\mathrm{K}^{-1}$ is the thermal coefficient and ρ_0 is the resistivity at 300 K. The electric potential distribution for the Nb layer is obtained by solving Poisson's equation

$$\nabla^2 V = 0. \tag{5.2}$$

A boundary condition for Equation 5.1 sets the temperature at the bottom of the substrate to room temperature (see inset of Figure 5.6) while three conditions are needed for Equation 5.2: one for the current input and two for the current output (as an example, see Figure 5.1 for junction 1). The two Equations 5.1 and 5.2 are coupled by the Joule heating term Q_e. The imperfect contact between Nb and Si imposes a thermal resistance R_{therm} which reduces the heat removal towards the substrate:

$$q_{int} = (T_{Nb} - T_{Si})/R_{therm}, \tag{5.3}$$

where q_{int} is the heat flux density to the substrate, R_{therm} is the thermal resistance in Km^2/W, T_{Nb} and T_{Si} the temperatures of the sample and the substrate, respectively. As an example, the junction 3 subjected to a succession of current pulses exhibits a resistance evolution represented by the blue curve in Figure 5.6. Simulations without taking into account thermal resistance ($R_{therm} = 0$) are given by the yellow dots and show that the heating is insufficient to account for the experimentally observed resistance increase. The thermal resistance $R_{therm} = 2.61 \times 10^{-8}\,\mathrm{Km}^2/\mathrm{W}$ is determined by iteration until the early states of electropulsing ($I < 20$ mA) are satisfactorily fitted (red circles). This value

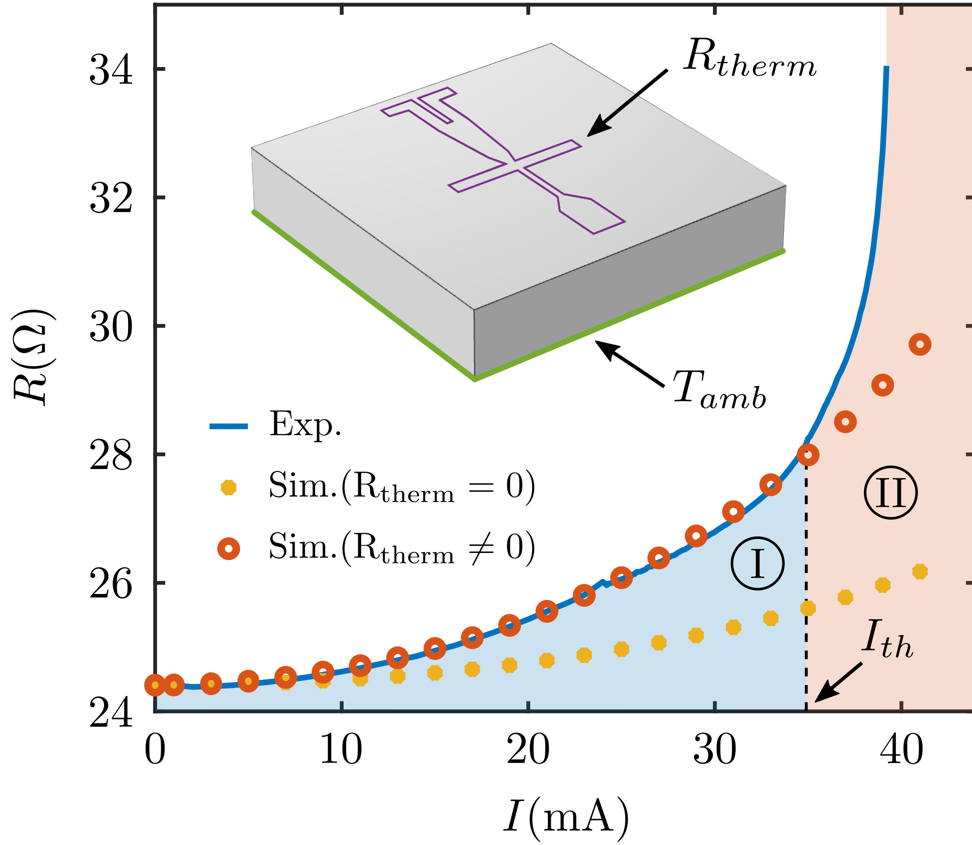

Figure 5.6: **Comparison between measured resistance during electropulsing and simulation with and without thermal resistance.** Typical current resistance (blue curve) observed during an experiment of electropulsing together with simulations without (yellow dots) and with (red circle) thermal resistance. The blue curve corresponds to $R_{max}(I)$ in Figure 5.3. The simulations highlight the existence of zones I and II whose transition at the threshold current I_{th} means the appearance of irreversible alterations in the transport properties of the sample.

of R_{therm} is unique and the same for all junctions. The threshold current I_{th}, beyond which irreversible changes operate onto the junction, is defined as the current for which the modelling underestimates the experimental value of the resistance, which leads to the distinction between two zones. Zone I, for currents lower than the threshold current ($I < I_{th}$), presents a reversible parabolic profile characteristic of the Joule effect without structural modifications. The second zone ($I > I_{th}$), is characterized by a sudden increase of the resistance due to irreversible alterations of the material's properties.

The electropulsing curves as well as simulations of the five junctions of the same sample are shown in the upper row of Figure 5.7. An average resistivity $\rho_0 = (37 \pm 3)\mu\Omega$cm has been determined to fit the value of the resistance at low current. The middle row of Figure 5.7 shows the current density profiles for the applied current I_{th}. Independently of the total injected current, we observe that the current density becomes more inhomogeneous as the funnel angle increases, leading to a maximum current crowding in junction 5. The

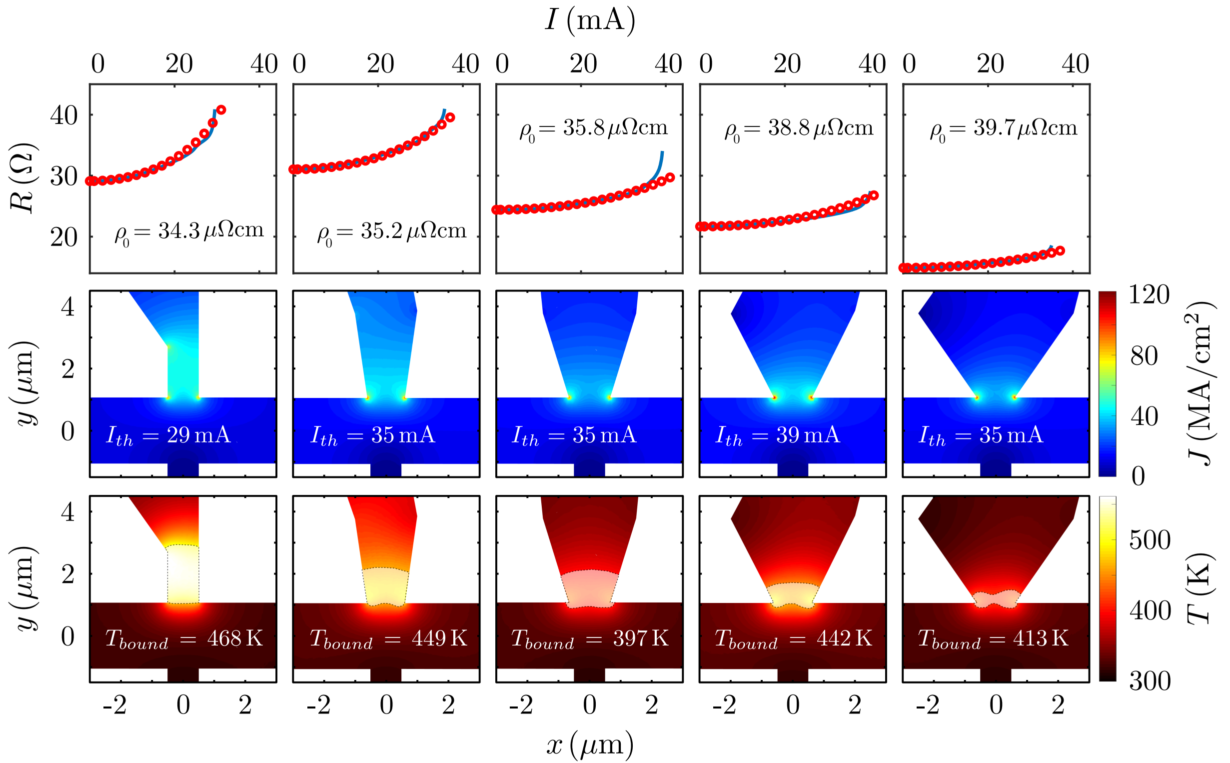

Figure 5.7: **Simulation results for the five junctions of the same sample.** The electropulsing measurements (blue curve) are given along with simulations (red circles) in the first row. The current density maps corresponding to the current I_{th} are shown in the second row. The images of the third row illustrate the temperature distributions, with the dashed curve denoting the isothermal curve $T = T_{bound}$ surrounding the modified region of the work function.

temperature maps, given in the bottom row, were compared to the affected areas of Figure 5.5(b,c) to determine the temperature T_{bound} at the boundary of the affected area for which the work function is modified. These isothermal contours are plotted in dotted lines together with the corresponding threshold temperature, which can be estimated as $T_{bound} \sim (435 \pm 35)$K. This temperature is to be compared with the results reported in Ref. [123] concerning the growth kinetics of thin aluminum-oxide films formed by the dry thermal oxidation of a bare Al (431) substrate at a partial oxygen pressure of 1.33×10^{-4} Pa. These authors identified a threshold temperature of 573 K below which an amorphous Al oxide film develops that attains a limiting thickness, whereas above this threshold the growth of the Al oxide layer is not impeded at a limiting thickness. In our results, the partial oxygen pressure at atmospheric conditions is substantially higher thus likely reducing the threshold temperature needed for steady growing of the Al oxide layer.

In addition to the oxidation of the Al capping layer, there is a simultaneous process of Nb oxidation taking place at the vertical walls of the Nb structure which are not protected by the Al capping. Indeed, it is known that Nb and Nb_2O_5 exhibit low diffusivity below

400 K yielding good long-term stability including thermal cycling up to 400 K [124]. In other words, it is not surprising that the resistivity increases at the loci where the local temperature exceeds 400 K. The numerical simulations also show a highly inhomogeneous local temperature rise with a hot core reaching above 550 K. The fact that above 570 K the oxidation of Nb consists mainly in a exponential growth of diffusion-controlled oxygen uptake [124], suggests that the hottest part of the junction may undergo bulk modifications as well. This is indeed consistent with the development of a double step superconducting transition after electropulsing as shown in Section 5.6.

5.6 Superconducting properties after electropulsing

As Nb is a superconductor, we performed measurements at low temperatures to observe the superconducting transition and the behavior of the weak-links formed in the junctions. The resistance vs temperature curves obtained for the addressed junctions (labelled as indicate in Figure 5.1) after electropulsing, are shown in Figure 5.8. In most cases the electropulsing leads to a two-step superconducting transition: as the temperature decreases, the first resistance drop occurs at about $T_c^0 = 5.8$ K, corresponding to the superconducting transition in part of the Nb bridge in between the voltage probes that remains unaffected by the electropulsing. This is followed by a second drop to zero resistance at lower temperatures which corresponds to the area affected by the electropulsing process. Note that the extension of the affected area is larger for junction 1 which explains the larger decrease of the superconducting critical temperature.

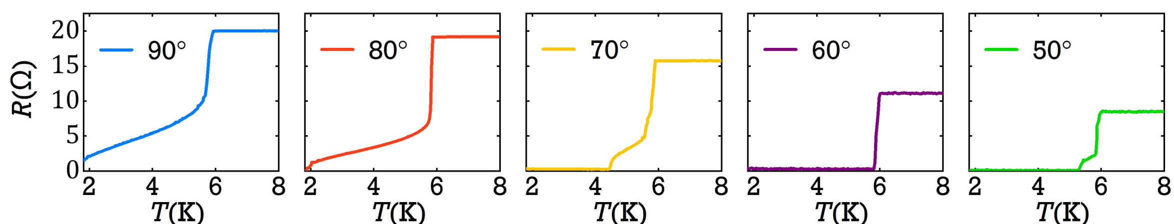

Figure 5.8: **R(T) curves for the addressed junctions.** The corresponding R(T) curves for all the junctions measured with an applied current $I = 1$ μA after electropulsing processes.

The fact that the critical temperature of unaffected material is substantially reduced with respect to the bulk value (9.25 K) is a well-known consequence of the fabrication method implying a lift-off procedure. Indeed, since Nb is a refractive material requiring

high target temperatures, significant heating and outgassing of the resist leads to reduced critical temperatures [125].

Besides that, I_c(B) characteristics for the 60° junction at 1.8 K are shown in Figure 5.9. Clearly, the modulation deviates significantly from the Fraunhofer form, failing to go to zero no matter what the applied field is and exhibiting asymmetry with respect to the applied current. It appears that the critical current density is nonuniformly distributed across the junction width. All five junctions exhibit this behavior.

Several factors can alter the plot of I versus B from a simple Fraunhofer pattern, so it is important to keep in mind how large these effects can be. As previously discussed in Section 2.3.2, the magnetic field inside a junction is influenced by the field associated with the current flowing it. As the temperature drops, the critical current, and therefore, the self-field, becomes larger. This self-field can then become large enough to promote a nonuniform current distribution at the junction. A situation such as this occurs when the Josephson penetration depth λ_J becomes comparable to or less than the width of the junction, and in this regime Equation 2.18 is no longer valid. When this effect is combined with that of an external magnetic field, the current distribution across the junction becomes asymmetric. According to Ref [126], samples with an aspect ratio W/L $\approx$ 1 and in the long-junction limit deviate from the Fraunhofer pattern. It has also been shown previously that SNS junctions also exhibit deviations from Fraunhofer-like I_c(B) dependence, both

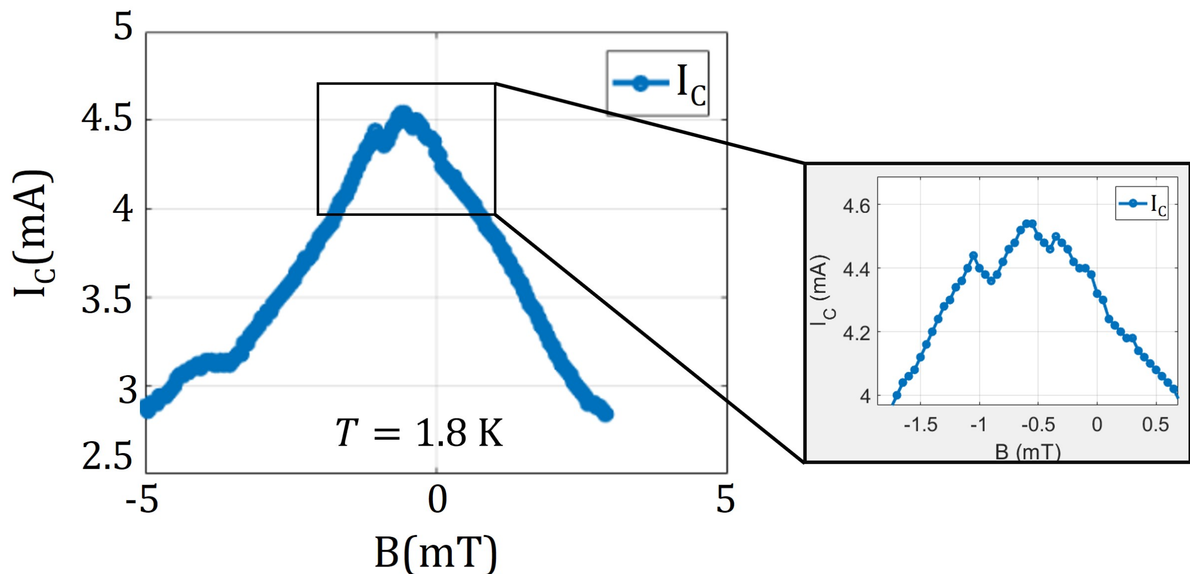

Figure 5.9: **Magnetic field dependence of the critical current for the 60° junction after electropulsing.** Critical current versus magnetic field applied perpendicular to the plane of the film at a temperature of 1.8 K.

in the diffusive limit [127] and in the quasiballistic limit [128]. In subsequent work, the quasiclassical Green's function approach has been used to elucidate how the junction geometry plays a role [129]]. In conclusion, we do not observed the Josephson signature for these weak links created by electromigration in Nb devices with different angles.

5.7 Reproducibility: KPFM and SEM

The observations described so far were corroborated by KPFM measurements in similar devices, one of which is presented in Figure 5.10. Although one constriction was damaged during electropulsing, the comparison between in-lens SEM and KPFM images in panels (a) and (b) once more reveals a close correlation of the regions affected by the process. Furthermore, the work function variation ($\Delta\Phi$) profiles displayed in panel (c) unmistakably reveal that these regions experience a drop in work function.

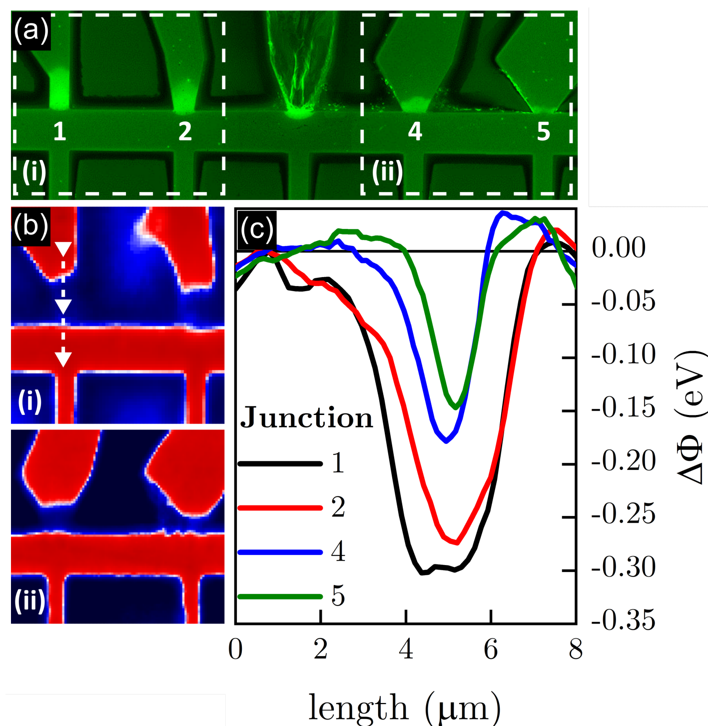

Figure 5.10: **SEM and KPFM images for Device B.** (a) SEM in-lens image for Device B exhibiting a higher contrast close to the electropulsed constrictions. During the experiment, the middle junction was damaged and therefore is not considered in the analysis. (b) KPFM images are shown for junctions 1 and 2 – region highlighted by dashed rectangle (i) in panel (a) – and junctions 4 and 5 – rectangle (ii). As in the main text, red coloured regions are associated to higher values of the work function than blue coloured ones. This is explicitly shown in the profiles of panel (c), where the work function variation ($\Delta\Phi$) is plotted around each junction following the direction indicated by the white arrow across junction 1.

Therefore, we can conclude that these results are reproducible for Nb in junctions prepared with different angles.

5.8 Conclusions

In summary, we have demonstrated the possibility to change the properties of selected individual Nb junctions in a device with an arbitrary number of terminals through electropulsing. This is an appealing approach by virtue of simplicity which permits nanofabrication without complex overlay processing and extra deposition steps. In addition, a large degree of selectivity is observed: unaddressed junctions remain intact and those targeted can be, to some extent, tuned by combining purposely predefined geometries and/or controlling the amplitude of the electropulsed current. As an illustration, this technique would allow us to transform a series of Nb contacts in Superconductor-Normal-Superconductor junctions or just normal contacts. The current work focuses on minor modifications of the material properties (low current amplitude) for which no abrupt structural change is revealed. In this limit, the affected area becomes apparent through in-lens imaging in a scanning electron microscope and as a contrast in Kelvin-probe force microscopy. Both characterization techniques point to a reduction of the work function and an enhancement of the secondary electrons yield in the affected area. This phenomenon has been investigated in the past and can also be attributed to physi- and chemisorption of O and C atoms. Complementary finite-element modelling using the exact geometry of the experimentally investigated samples suggests that the affected area is hotter than 435 K. The current blooming of Niobium-based superconducting devices together with the continuous progress on Nb thin films employed in transmon qubit architectures and the critical role played by oxygen vacancies as a decoherence mechanism, make the findings of this report timely by unveiling the severe implications of applying moderate currents in those devices.

Chapter 6

Structural modifications of Al and Ni multiterminal bridges

In Ni, EM process takes place in a very well defined location, as expected by current crowding and local heating. In contrast to that, EM in Al seems to proceed more randomly, perhaps due to less transparent grain boundaries.

6.1 Introduction

In recent years, it has become increasingly clear that EM is a multiphysics process that involves electrical, thermal, and mechanical effects at the nano- and microscales and is largely governed by crystalline structure, punctual defects, grain boundaries, and other imperfections. Therefore, determining the root causes is complex and difficult. However, it has long been known that grain boundaries are typically crucial for regulating the movement of atoms in a material [130, 131]. A grain boundary triple point, such as the one depicted in Figure 3.5, is an optimal site for void nucleation because mass may enter by diffusion along one boundary but exit more quickly along the other two. Contrarily, material can pile up to form a hillock if there are two incoming boundaries and only a single outgoing. Because of the importance of grain boundary diffusion, the precise microstructure of the grains is extremely important in EM in microscale interconnects. In order to comprehend this process, numerous theoretical models have been proposed to describe the influence of various combinations of electromigration, temperature and stress gradients, and hillock formation on the mass transport of atoms impacted by grain boundaries. An excellent resource dealing with this topic is the review paper by Ho and Kwok [43]. Additionally, Sethian, Wilkening, and Borucki [132, 133] investigated the effect of EM and mechanical stress on grain boundaries.

Clearly, polycrystalline structure and grain boundaries play an important role in the explanation of EM [46]. It has been demonstrated that, under identical stress conditions, electromigrating Al single crystals is far more challenging than electromigrating polycrystalline Al [134]. There have been a number of reports on EM of microscale Al bridges [56, 135, 136], but little is known about EM of microscale Ni bridges. Possibly, this scarcity of research involving Ni-based devices is related to the fact that the greatest motivation for such studies stems from the interest in increasing the reliability of circuits with a great deal of work being directed towards extending the lifespan of conductors. Typically, conductor lines are made of pure metals (most notably Al and, more recently, Cu) or dilute alloys [137]. However, in recent years, nickel nanowires or nanorods have attracted a lot of interest due to their wide variety of potential applications in sensors and other fields [138–140]. In addition, high-density current flow through ferromagnetic nanowires has lately received a lot of attention [141–143].

In this work we investigate the structural modifications of Al and Ni microconstrictions induced by elecropulsing by monitoring their resistance during EM. We apply current

pulses to locally change the physical properties of the constrictions. Scanning electron microscope inspection showed that the voids and hillocks found in EM of Al are noticeably missing in EM of Ni. Thus, the effect grain-boundary diffusion, stress gradients and void formation is replaced by gentle electroannealing. In Ni, the EM process takes place in a very well defined location as expected by current crowding and local heating. In contrast to that, EM in Al seems to proceed more randomly, perhaps due to less transparent grain boundaries.

6.2 Experimental details

As previously described in Chapter 4, Aluminum and Nickel samples were fabricated in two steps. The initial step involves patterning the constrictions. Photolithography was used to shape Al and Ni samples on a Si/SiO_2 substrate (381 $\pm$ 20 μm Si, 100 nm SiO_2) covered by a photoresist mask. Following that, an Al single layer ($\sim$ 30 nm) or Cr ($\sim$ 5 nm)/Ni ($\sim$ 25 nm) bilayer thin film was deposited using e-beam vapor deposition at a deposition rate of 1 Å/s and a pressure in the chamber of 1.8 $\times$ 10^{-7} mbar. The deposition was followed by a lift-off process. The second step involves creating Al contact pads for both samples. After completing the photolithography steps, 200-nm-thick Al was deposited on the patterned resist using an e-beam at a deposition rate of 1 Å/s at a chamber pressure of 1.8 $\times$ 10^{-7} mbar. The final step was a lift-off procedure.

To address the central bridge, all electrical measurements were taken in the Kelvin 4-terminal configuration, as shown in Figure 6.1(a). In this configuration, the current is applied across the outer contact pads and the voltage drop is measured across the contact pads corresponding to the bridge. In this approach, just the portion of the sample between the inner contact pads produces a signal, and the resistance of the circuit and the majority of the sample is not recorded. Due to the low noise and overall circuit impedance, very low absolute resistances may be measured with ease because essentially no current flows through the inner contact pads. The electropulsing protocol is the same applied in the study of Nb bridges discussed in the previous chapter. The current profile is that presented in Figure 6.1(b). Several iterations of this process were carried out until the normal state resistance of the sample had increased significantly. The experiment is conducted in ambient conditions.

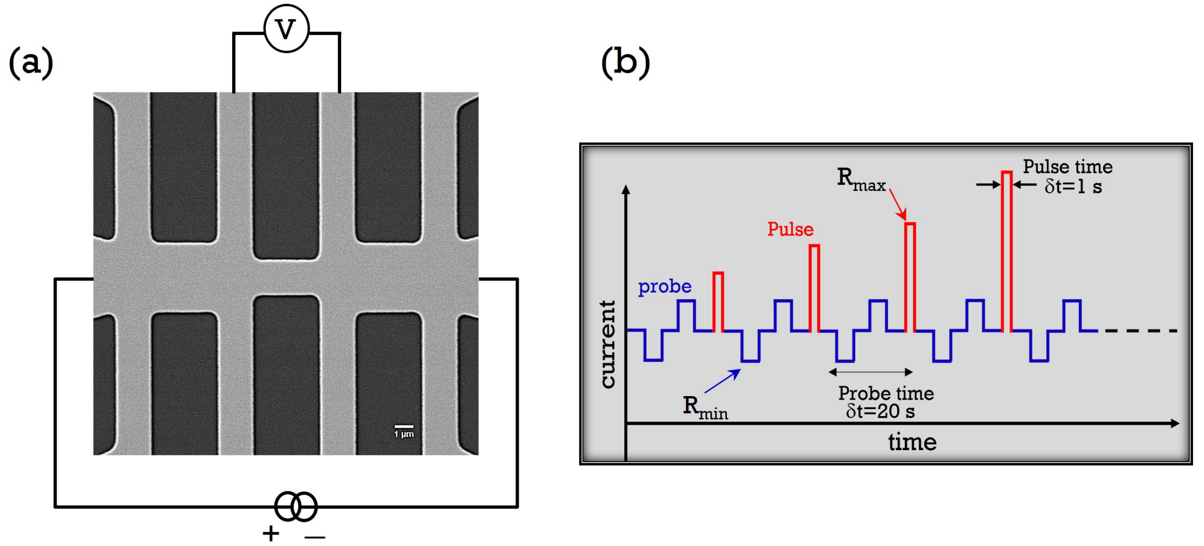

Figure 6.1: **Sample layout and measurement protocol.** A dual-channel source-meter Keithley 2612B is used to excite and probe the samples. (a) Kelvin 4-terminal setup with current supplied across the the outer contact pads and voltage drop measured across the bridge contact pads. (b) The electropulsing protocol used, with the probe and pulse time shown. Electromigration takes place at ambient temperature.

6.3 Electromigration properties

In this chapter, we present results obtained with bridges of Al and Ni that have been subjected to seven EM runs each, followed by microstructural characterizations. EM1 and higher represent the data measured after the first and subsequent runs of EM, respectively. Figure 6.2 illustrates the evolution of resistance as a function of current pulses (I_{PLS}). As observed in both devices, when I_{PLS} is low, the resistance does not depend on the intensity of the applied current, i.e. $R_{max} \approx R_{min}$ (heating regime). The steady value of R_{min} evidences that EM does not begin immediately as I_{PLS} is increased. Continuing the process of rising the current - and J in the constriction - gives rise to the electromigration regime. A sudden upturn at high current amplitudes signifies the commencement of irreversible alterations in the sample caused by electropulsing. It is expected that when I_{PLS} increases, R_{max} surpasses R_{min} as a result of Joule heating and the finite resistance temperature coefficient. The parabolic increase in R_{max} with increasing I_{max} arises from the local increase in temperature due to Joule heating. A rough estimation of the local temperature at the constriction can be obtained from the expression in Equation 3.15,

$$T = T_{ref} + \frac{1}{\alpha}\left(\frac{R}{R_{ref}} - 1\right) \tag{6.1}$$

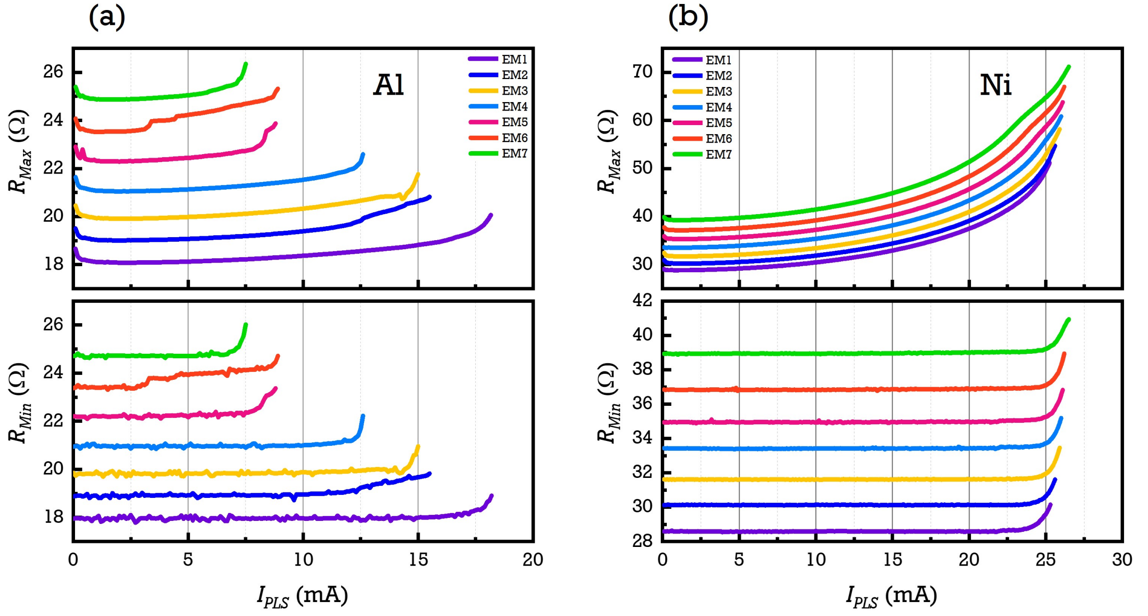

Figure 6.2: **Evolution of R_{max} and R_{min} as function of I_{PLS}.** Each EM run is represented by a different color. Every successive EM run was initiated at 0 mA and the current progressively increased until R_{min} increased by 5%.

where R is the resistance at temperature T, R_{ref} is the resistance at a reference temperature (T_{ref}), and α is the temperature coefficient of resistance for the material. This expression holds as long as the resistance exhibits a linear temperature dependence and the structure of the system does not change. As such, this model describes the general trend of resistance increasing due to Joule heating effects for currents below the onset of EM (I_{EM}), which we defined as the point at which R_{min} changed by 1% compared to its initial value as depicted in Figure 6.3. To that purpose, the EM1 (in both devices) is used for estimating the temperature at the constriction for which $\alpha = 3.48 \times 10^{-3}$ K^{-1} for Al and $\alpha = 1.28 \times 10^{-3}$ K^{-1} for Ni [144]. Based on this expression, the local temperature before the onset of EM for Al is 390 K and for Ni it is 710 K. In a study of microstrip samples of Al, Lombardo *et al.* [31] estimated the temperature to be 420 K before the onset of EM. A study by Yamaguchi *et al.* [145] obtained temperatures of 750 K for NiFe samples after the application of high current densities. It is important to note that the resistance measurement plotted in Figure 6.2 results from the potential difference between the inner voltage contacts which is 4 micrometers wide, and therefore, for a given applied current, the temperature distribution is not uniform throughout the bridge. In this case, using Equation 6.1, which was derived under the premise of equal temperature distribution, is uncertain. For proper resolution of this problem, numerical simulations of the coupled electric and thermal equations are essential. We will be able to obtain the temperature

distribution at the constriction thanks to the simulations which will be shown in subsection 6.4.1. Furthermore, when the 5% resistance increase is achieved, it is projected that the local temperature rise would be substantially higher. See subsection 6.4.1.

It is worth noting that the maximum current amplitude I_{max} required to generate the requisite resistance increase varies greatly depending on the device. In the case of Al, this decreases dramatically with subsequent EM runs due to the mechanical stress, but in the case of Ni, the I_{max} grows somewhat with each subsequent EM run as shown in the inset of Figure 6.3(a). It would not be surprising if Cr contributed to the EM process. The formation of an alloy between Ni and Cr could be conceivable, particularly if the temperatures during the EM are sufficiently high. Considering that Ni-Cr is quite resistant to wear, it may raise the threshold of EM. The J may be estimated using

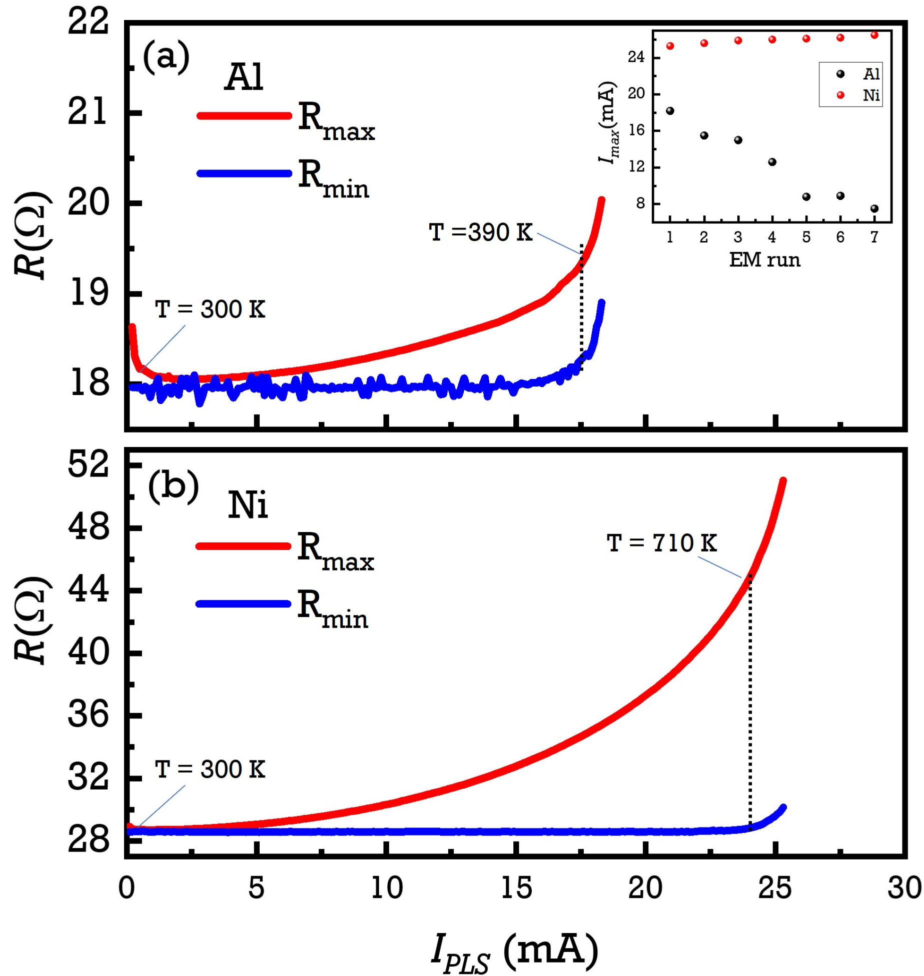

Figure 6.3: **Estimation of the temperature at the constriction.** R_{min} of the first EM run obtained at $I_{min} = 100$ μA after the current I_{max} pulse. The dashed lines represent the threshold used to designate the onset of EM, which corresponds to a 1% rise in the original resistance value. The temperatures are the maximum values that could be achieved at the constriction prior to any structural changes to the system. The inset of panel (a) shows I_{max} as a function EM run.

I_{max} and the fabricated geometry of the constriction for EM1 (J_{Al}= 300 MA/cm^2 and J_{Ni}= 450 MA/cm^2). It is unclear about J for Al and Ni in the case of EM2 and the successive ones, since the thickness varies as a result of EM, and the exact geometry is not known. Nonetheless, it is predicted that J will rise with increasing I_{max} and decrease with decreasing I_{max} if the sample geometry remains constant. A significant increase in resistance in Al is typically the result of both a reduction in cross section due to the generation of voids at the constriction, as well as a relief of internal stress. In such a case, mechanical stress may significantly reduce the current required to trigger EM.

6.4 Microstructural effects due to EM

In this section, we will examine the effects of electropulsing on each of the devices, focusing on the central bridge. This is accomplished through the use of SEM, AFM and MFM images.

Al constriction

Figure 6.4 presents close-up SEM images of the device constriction before and after electropulsing. Material transport in Al occurs primarily along grain boundaries, as a result of immobilized atoms at the surface due to oxidation. Dislocations and grain boundaries are sources of vacancies. At ambient temperature, when aluminum is exposed to air, a thin oxide coating forms on the surface. The thickness of the oxidation layer is typically between 1 and 10 nm, however the growth of thickness is highly dependent

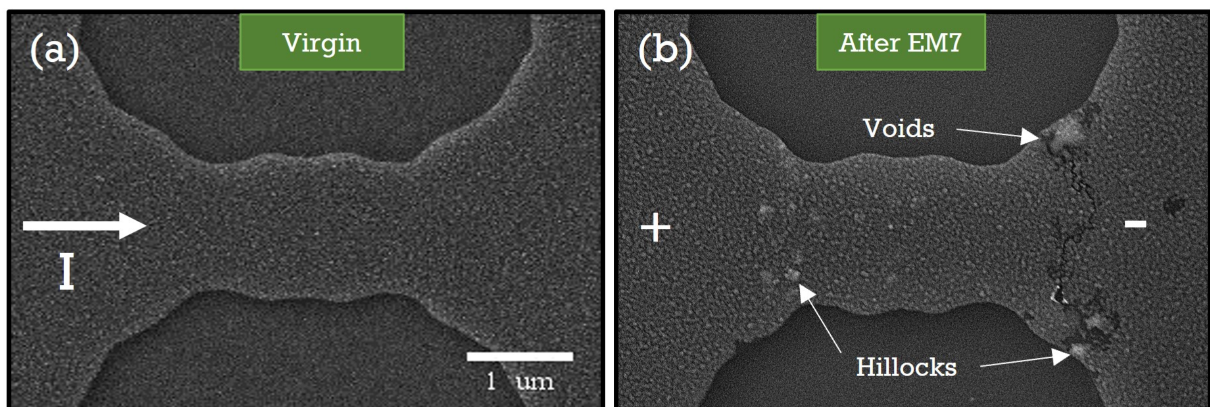

Figure 6.4: **High-resolution SEM images of electropulsed sample.** (a) The left panel displays the SEM image of the constriction in its virgin state, while the right panel (b) depicts the constriction after the 7th EM run. The constriction has undergone structural alteration, since both voids (dark) and hillocks (bright) are now visible. The voids and hillocks are mainly concentrated near the cathode and anode, respectively.

on temperature and environment. Because the native aluminum oxide is protective, the contact between the metal and its oxide is not a suitable source or sink of vacancies [137]. Therefore, in Al, these grain boundaries introduce a more stochastic removal of material. As previously noted by Pierce and Brusius [46], gradients in grain size, in material dimension, in temperature, and triple connections of grain boundaries, can all contribute to flux divergences. The movement of atoms in Al causes strains normal to the grain boundaries due to grain confinement. As a result, EM causes lateral compressive stresses at the anode and tensile strains at the cathode end of the aluminum device. It follows then that an electromigration-driven flux of Al atoms to the anode necessitates an opposite-direction flux of vacancies to the cathode. The SEM image in Figure 6.4(b) clearly illustrates the formation of voids (dark) on the cathode side of the bridge and hillocks (bright) at the ends of the bridge as well as in the vicinity of certain voids. It is common for grain boundaries, defects, or impurity sites to have less favorable coordination and lower potential energy minima, which enables atomic motion to occur more readily [146, 147]. It is also likely that regions of higher steady-state temperatures will be more conducive to atomic migration when a structure exhibits nonuniform Joule heating or heat dissipation. Temperature gradients are very significant in this part of the bridge. In this context, it can be explained by the fact that the temperature rise is not uniform between the voltage contacts. Due to the influence of temperature gradients, atoms diffuse from relatively high temperatures to lower temperatures, which results in mass transfer in the direction of the anode. It can be argued that the current density increases the temperature through Joule heating, and that this change in temperature goes on to modify mechanical stress through variations in expansion coefficients. As a result, the diffusion coefficient (Equation 3.12) is influenced by temperature and mechanical stress.

It is important to mention that a second set of Al samples was studied. These samples were decorated with a lattice of nanoholeys and more details are presented in Appendix A.

Ni constriction

SEM images reveal some typical features of the surface modification of the Ni device taking place in the middle of the junction. Based on our analysis, we have described that the temperatures at the middle of the device is much higher than those near the pads, since heat is released more readily at the ends, where the pads have a relatively large surface area. Figure 6.5(a) displays a SEM image of the virgin state sample, (b) is the SEM image

taken after the 5th EM run for a sister sample, whereas panel (c) indicates an alteration in the central bridge after the seventh EM session. In comparison to the virgin condition and to neighboring parts of the bridge, this modification is seen as two substantial brightness contrasts: the most central area shows a darker region (almost square), delimited by two thinner stripes on each side. The three SEM images shown in Figure 6.5 reveal that the modification evolves gradually. The observed modification in the central bridge (Figure 6.2(c)) is associated to an increase of the overall resistance of the device. Furthermore, the SEM image do not show the usual hallmarks of electromigration, which is the transport of material, such as voids, and hillocks. Ni films have been shown in numerous studies to exhibit agglomeration, which is the tendency for the film to form clusters or islands on the surface rather than remaining a continuous film. The degree of agglomeration can vary depending on various factors, such as the thickness of the film, the substrate material, the deposition technique used, and the annealing conditions [148–150]. The majority of nickel films are polycrystalline [151, 152] in structure and have embedded agglomerations measuring between 30 and 40 nm in thickness. Although the film is agglomerated in this thickness range, it remains continuous in appearance with aggregate boundaries.

It is evident from Figure 6.5 that we have succeeded in inducing modifications due to the electromigration process. In order to study the morphology and domain structure of the device, AFM and MFM measurements were conducted using a two-pass scan. The first pass is performed in tapping mode to obtain from, a single line, a unidimensional scan of the surface morphology. Subsequently, the probe follows the topography taken in the first scan keeping a constant height (non-contact or lift mode), recording only the magnetic interactions. Measurements were conducted using a magnetic tip (Multi-75G) and a lift height of 40 nm. These measurements are shown in Figure 6.6 and were obtained after the 7th EM run. In panel (a), there seems to be no change along the middle part of the bridge. However, zooming up the image at the region of the bridge allows us to verify that, in reality, there is a variation in the thickness. Two channels with depths of 1.5 nm on the left and 1.0 nm on the right delimit a maximum in the central region of the bridge, whose thickness is around 3 nm above the baseline, presented in Figure 6.6(c). Therefore, these changes are similar to the SEM image and the grayscale profile along the bridge presented in Figure 6.5(c) in the main panel and inset, respectively .

Figure 6.6(b) is a map of the magnetic phases of the same region of the device. In this case, the unaffected area of the sample displayed in-plane magnetic domains, and the modified region showed domains with an additional out-of-plane component in the

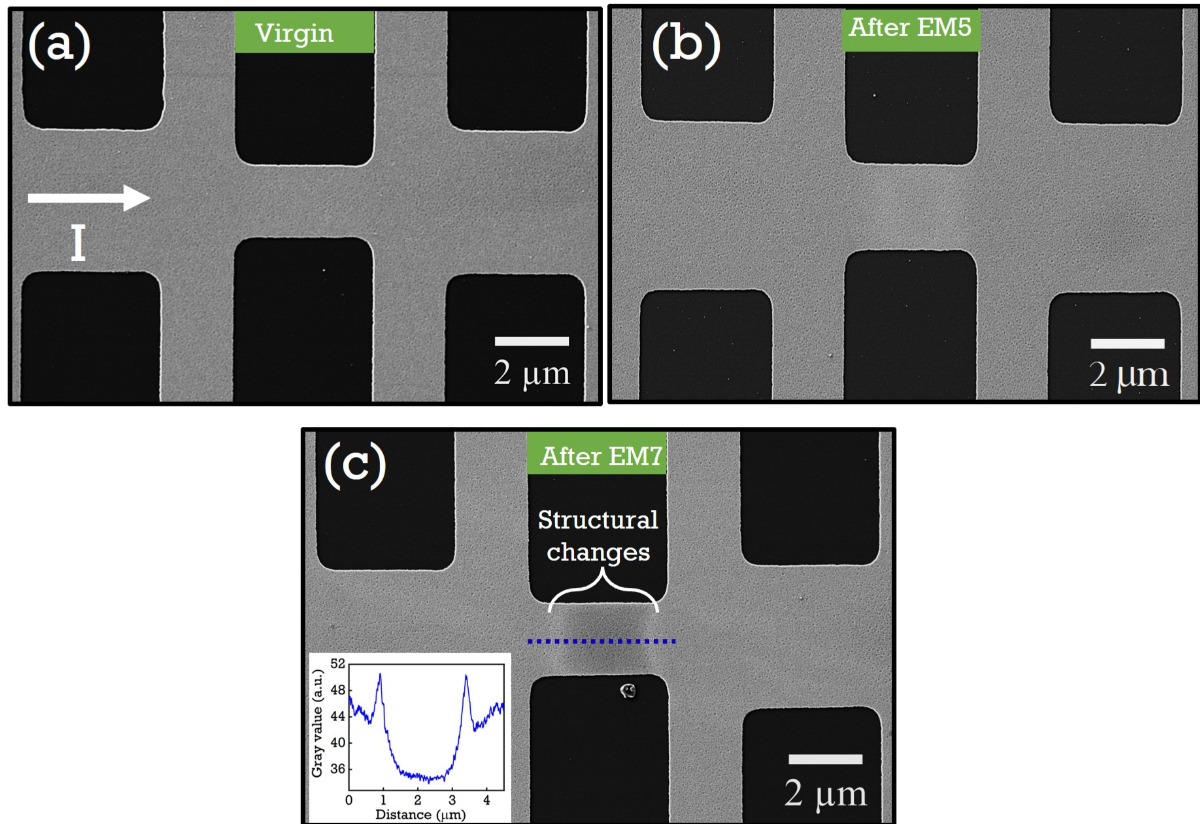

Figure 6.5: **SEM images of the Ni sample investigated.** (a) Virgin sample. (b) Taken after EM5 (sister sample). (c) Very last state of the first device taken after EM7. The inset of (c) shows the profile plot in the constriction.

magnetization since the MFM image shows a change in the phase along the central bridge. Besides that, this change in the spontaneous magnetization matches with the thickness-variation region in the AFM profile, as depicted in Figure 6.6(c). Therefore, the EM induces a variation in the magnetic properties of the Ni/Cr bilayer. Let us consider both materials separately: Cr presents a magnetic transition between a paramagnetic phase and an antiferromagnetic phase at the Néel temperature of approximately 311 K. In contrast, Ni is a ferromagnetic substance with a Curie temperature (T_{Curie}) of around 628 K [153, 154]. For thin film geometry, T_{Curie} for Ni decreases systematically with the thickness and reaches approximately 617 K for a 30-nm-thick Ni film [136]. Therefore, the origin of the in-plane magnetic domains in the unaffected region is due to the 25-nm-thick nickel layer, which presents a strong in-plane magnetic anisotropy at room temperature [155]. It is essential to mention that Cr often serves as a buffer layer to improve adhesion of the Ni film to the substrate [156].

Based on our analytical calculations and numerical simulations, shown in the next section, we may conclude that the temperature at the constriction is higher than the Curie temperature of Ni, implying that there is probably a phase transition between

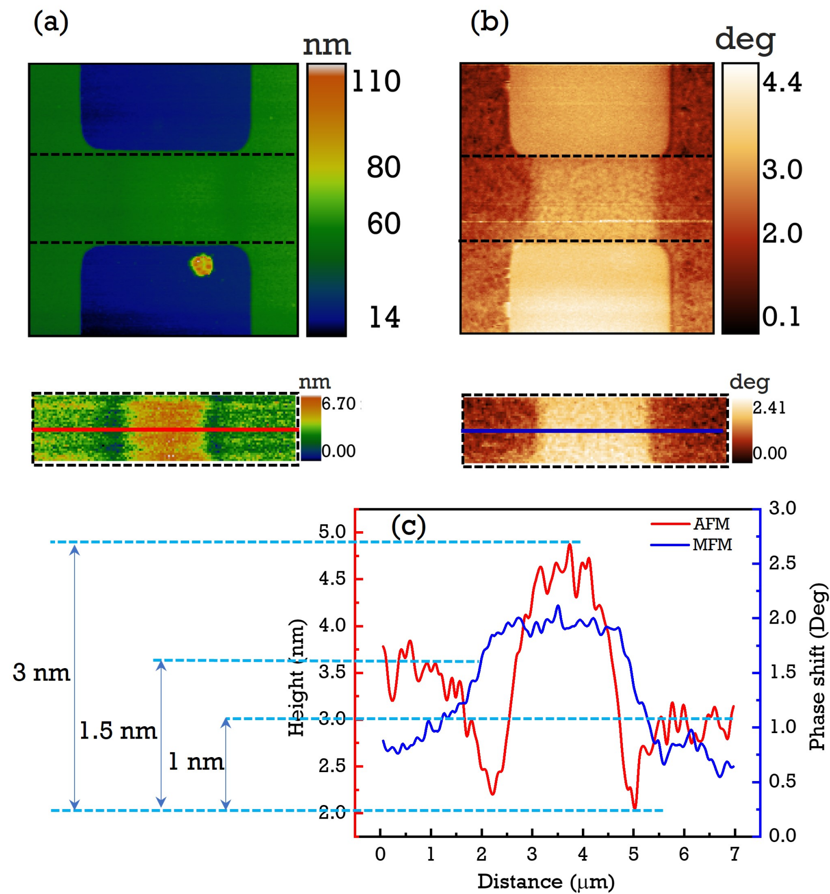

Figure 6.6: **AFM and MFM imaging of the Ni device after EM.** AFM (a) and MFM (b) images of the Ni sample post EM. The images are scaled down to the bottom images in order to get a better glimpse of the modified constriction. (c) Profiles taken from the central bridge for AFM and MFM measurements.

ferromagnetism and paramagnetism. It means that, although Ni has no net magnetic moment above the Curie temperature, a net magnetization, with an out-of-plane component, appears when the device cools down.

Considering all these evidences, there are at least two hypotheses to explain the appearance of an out-of-plane component in the Ni/Cr bilayer: (i) the oxidation of the nickel layer, which was exposed to air; (ii) the formation of a Ni-Cr alloy at the interface. The first one would be related to the oxygenation of the Ni film due to high temperatures reached during the EM process (above 700°C). The oxygenation of Ni films in air was studied for intermediate temperatures (up to 500°C) [157, 158] and higher temperatures [159, 160], showing that they oxidize to a chemically stable NiO phase, which behaves antiferromagnetically below T_N = 523 K, being a p-type semiconductor with a band gap of 4.0 – 4.3 eV [161]. In 2014, Valladares *et al.* [157] studied the oxidation evolution and its effects on the structural and magnetic properties of 50-nm-thick Ni films by changing

the annealing temperature. For annealing temperatures above 350°C for *three hours*, the NiO peaks in X-ray diffractograms appear gradually due to oxide formation, accompanied by a progressive decrease in the pure Ni peaks. At 700°C for *three hours*, only NiO peaks are revealed, indicating the complete oxidation at the surface of Ni film. Magnetization loops are reported for the in-plane and out-of-plane directions at 50 K. For the samples annealed below 500°C, the hysteresis loops show the presence of ferromagnetic nickel domains, revealing the preferred in-plane direction of the magnetization, even with the antiferromagnetic NiO phase. At higher annealing temperatures (700°C), $M(H)$ curves are reversible, exhibiting no hysteresis. Thus, the disappearance of the ferromagnetic signal means that the Ni film is completely oxidized. It does not seem to be the case in the MFM image in Figure 6.6(b), in which an out-of-plane component appears after the EM process. Despite this, it is still important to emphasize two points: (i) the duration of the annealing treatment, which is 3 h and therefore much longer than the time that the EM process lasts ($\sim$ 1h 40 min*); (ii) if the central region of the bridge is antiferromagnetic due to NiO, the stray magnetic field of in-plane magnetization of the unaffected areas could lead to the result obtained via MFM. However, this does not seem to explain all features presented by the $R(I)$ curves presented earlier.

Concerning the second hypothesis, chromium is usually added to Ni-based alloys to protect against corrosion [162]. Thus, the diffusion of Cr in Ni is extensively studied. The diffusion coefficient is faster for temperatures of the window 600°C-900°C, when compared to lower temperatures [162]. Therefore, the interdiffusion between Ni and Cr under high annealing temperatures may result in an alloy according to the phase diagram of Ni–Cr [163] – possibly a solid solution [156] or even metastable Ni-Cr phases [164, 165]. Recently, Ohgai *et al.* [166] prepared Ni and Ni-Cr films using electrodeposition from electrolytic aqueous solutions. As in our case, pure Ni films were easily magnetized along the in-plane direction. However, when 9.5%Cr was added to the composition of the Ni-Cr films, forming an alloy, the magnetization loops presented a quasi-isotropic magnetization behavior, i.e., an out-of-plane magnetization component emerged. The authors attributed that to the typical structure with columnar nanocrystalline grains isolated by the amorphous phase, indicating that in-plane internal stresses induce magnetoelastic anisotropy, also found in Ni-W alloy films [167]. Therefore, the out-of-plane component of magnetization, which appears in the MFM measurements, is probably due to the alloying between Cr and Ni in

*This total time relates to how long the entire EM procedure takes. The duration of the current pulses in this instance is 1 s, with intervals of 20 s between them.

the vicinity of the interface, where the temperature reaches higher values due to Joule heating along the bridge.

Besides that, the possible formation of Ni-Cr alloys at and around the interface could also increase the electron scattering, thus causing the higher resistivity as in the $R(I)$ measurements after each EM run, presented in Figure 6.2(b). Since the films are thin, the effect of this scattering along the film thickness in the central region was large enough to be captured by the resistance measurements. Another important point is the maximum current needed to reach the maximum allowed increase of 5% in the resistance, at which the experiment is halted (shutoff resistance), which unexpectedly increases for Ni as opposed to the aluminum bridge. Considering that Ni–Cr films are used for the fabrication of thin film resistors in integrated circuits, one of the most important properties is related to its near-zero temperature coefficient of resistance [164], i.e., increasing the temperature slightly alters the resistance of Ni-Cr films. Surprisingly, the temperature coefficient of resistance is negative for films with high Cr content [144]. In contrast, this coefficient is always positive for pure Ni and orders of magnitude larger than for any Ni-Cr alloy composition. When a Ni-Cr alloy is possibly formed in the affected region of the bridge due to the first EM run, for instance, the overall resistance of the device increases, as captured in the second run and depicted in Figure 6.2(b). However, the local resistance of this region almost does not increase as a consequence of the Joule heating, even being that the most sensitive part of the bridge. Therefore, a higher current must be applied to reach the shutoff resistance since its local resistance keeps almost constant during the EM process.

Moreover, the AFM profile shows a quasi-symmetric thickness effect with respect to the middle of the bridge, i.e., an increase of thickness in the central area and two lateral grooves surrounding it. If oxygenation occurs, the thickness variation would probably gradually follow the temperature distribution. If Ni-Cr is being formed, EM may affect the central bridge by moving Cr toward its center and excavating the first lateral channel. Then, it triggers the stress migration and other mechanisms related to atomic diffusion, excavating the second lateral channel. On the other hand, the increase in temperature provokes the interdiffusion between Ni and Cr toward the central part of the bridge, moving atoms from the region with a temperature high enough to allow atomic diffusion and probably the formation of a specific Ni-Cr phase in the core of the device. It is also important to mention that one explanation does not necessarily exclude the other, since both effects – oxygenation, and Ni-Cr alloying – may occur simultaneously.

To verify these hypotheses, structural characterizations very localized should be employed. These might include electron diffraction using Transmission Electron Microscopy (TEM), high-resolution TEM, Micro-Raman Spectrometry, Extended X-ray absorption fine structure (EXAFS), and other focused X-ray techniques available in synchrotron facilities. A possible way to eliminate the oxygenation of nickel would be to run the EM process under a controlled atmosphere without oxygen.

6.4.1 Finite element modelling of the temperature distribution

After evaluating the experimental data, we used finite element modeling (FEM) to ascertain the origin of the observed modifications in the Ni constriction, taking into consideration the exact shape of the samples acquired from the SEM image analysis. The mesh and boundary conditions for the Ni device are shown in Figure 6.7. In the present case, the current is applied on the left (red) terminal and flows towards the right (blue) terminal, where a ground boundary condition is imposed. The spatial temperature distribution in the system is calculated using the FEM-based modeling program COMSOL multiphysics [168].

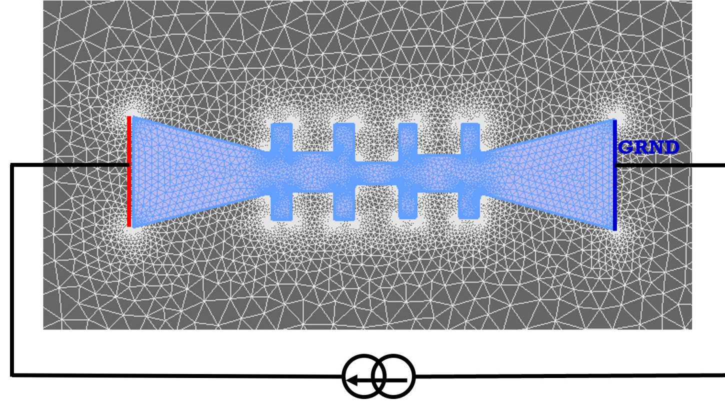

Figure 6.7: **Mesh and current boundary conditions used for FEM modelling.** The dimensions of the simulated sample were based on those acquired from the SEM images of the real sample. The electrical current is introduced into the right side and flows towards the left side, where a ground boundary condition is enforced.

We can estimate the resistivity to be ρ_0= 42.8 $\mu\Omega$cm based on the exact geometry of our sample and the resistance at low current. The thermal conductivity for Si and Ni were assigned 130 W m^{-1} K^{-1}[121] and 97.5 W m^{-1} K^{-1} [169] respectively. The simulated Ni sample has a temperature dependent resistivity given by the $\rho(T) = \rho_0(1 + \alpha(T - T_{ref}))$, where T_{ref} = 300 K. All surfaces of the system are considered thermally and electrically

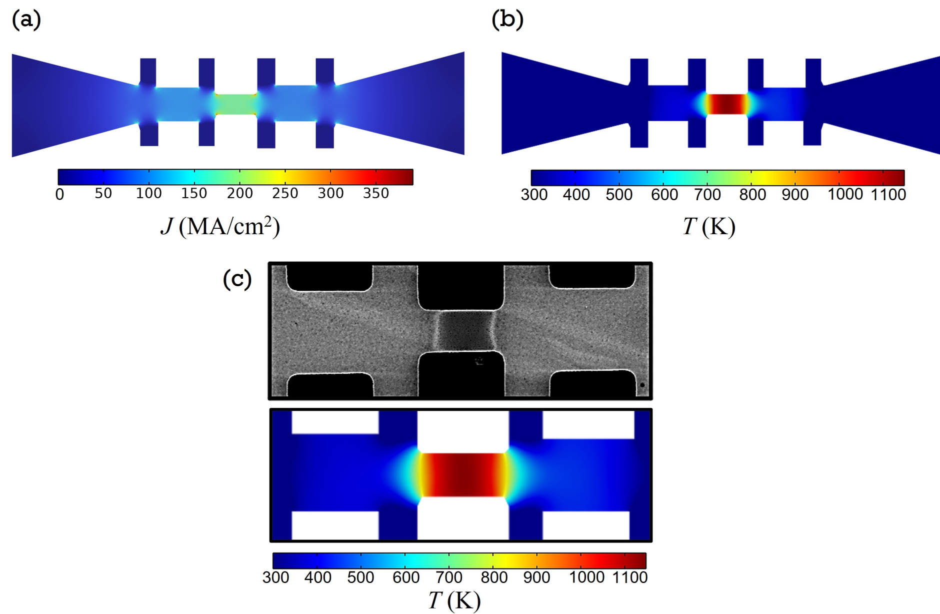

Figure 6.8: **Simulated current density and temperature distribution of Ni sample for an applied field 26 mA.** (a) The inhomogeneous current density (b) Simulated temperature distribution of Ni sample for an applied current of 26 mA. (c) Comparison between SEM image (after EM) and FEM simulations.

insulating, except the ground and terminal. Constant ambient temperature boundary condition is imposed at the bottom surface of the substrate.

Figure 6.8(a) shows the inhomogeneous current density profile of the system. The current distribution is predominantly concentrated in the constriction, notably in the corners, where the current density is approximately 400 MA/cm^2. The temperature distribution map in Figure 6.8(b) reveals that the "hottest" area is the middle of the constriction. As a result of Joule heating, the temperature at this point is dramatically enhanced. The formation of a gap was observed in a sister sample (see Figure 6.9), indicating thermal runaway in this location. This is consistent with the FEM results, which show that the area is prone to thermal runaway as a result of greater currents. A recent study conducted by Sun *et al.* has examined the thermal cycling fatigue caused by Joule heating in 35-nm-thick, and 0.1-5 μm wide Au interconnects [170]. The experiments are performed under different current densities and interconnects widths which discovered that narrower interconnects are more reliable under a given current density. Their SEM data demonstrate that failure occurs mostly in the core (the hottest location) and that there is no indication of surface morphological changes associated with EM, such as hillocks. Finally, they determine that the failure mechanism is caused by thermally-assisted grain growth and reorientation, which raises local resistance and results in Joule-assisted melting.

Figure 6.8(c) depicts a comparison between the SEM image of the affected area and the temperature map.

6.5 Nanogap formation

We discussed above the effects of the eletromigration before the rupture of the material. As the regime at the constriction changes from heating to electromigration, atomic rearrangements seem to be triggered at relatively high current densities. Fundamentally, a high current density applied across the constriction causes metal atoms to migrate, driven by momentum transfer from the electrons. As seen in Figure 6.9, the final phase of migration of atoms results in nanogap.

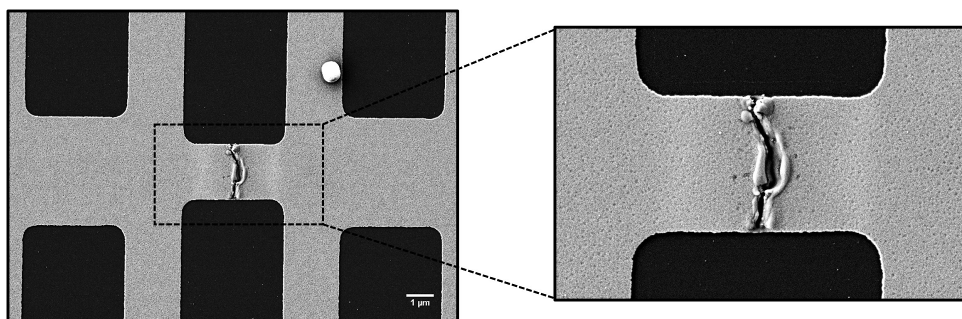

Figure 6.9: **Formation of nanogap.** By performing a total of eight EM runs on a separate device, we discovered that the final phase of the modification is characterized by the emergence of a gap on the order of nanometers.

Due to the movement taking place at the constriction region, the loss or gain of a single atom will produce a significant change in resistance. As a result of this process, the resistance of this constriction rises suddenly and randomly, and its final resistance is huge, indicating that a gap has formed. In this example, one additional EM run was added to the previous seven (see Figure 6.10). Indeed, rather than creating nanogaps, our primary goal was to double the usual resistance of our sample. Nonetheless, if controlled nanogap creation is necessary, our software and measurement technique have proved to be effective. Previously, electromigrated nanogaps had been captured by scanning electron microscopy [40], tunneling electron microscopy [171], and atomic force microscopy [42] on nanowires of Al [172], Cu [173], Pt [174], and Au [175].

Nanogap is a crucial device in the field of nanotechnology. In recent years, electrical nanogap devices have gained popularity because of their potential applications of optical devices [176], electronic devices [30] and biodevices [177, 178]. There are now different procedures for creating nanogaps [179–182], but among these potential approaches, elec-

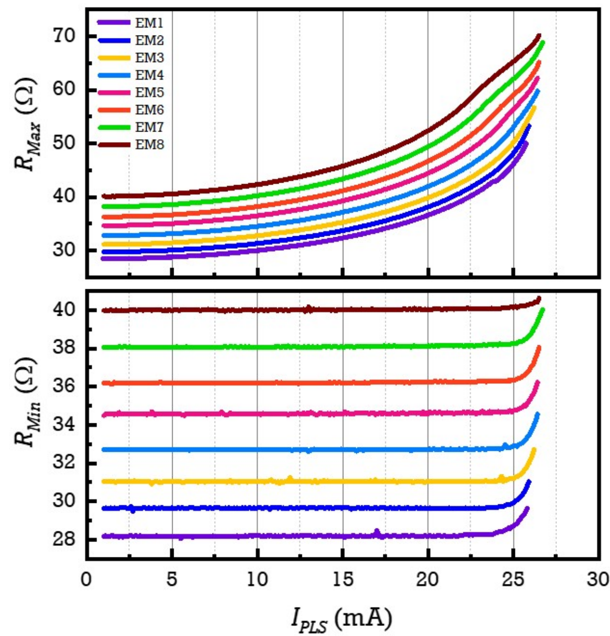

Figure 6.10: **The resistance-current characteristic curves for SEM image depicted in Figure 6.9.** It is evident that the characteristics of these curves resemble those observed in the previous device, thereby validating the reproducibility of our findings.

tromigrated nanogaps stand out due to their ease in small-scale creation, stability in constriction, and viability in the Si process. In the field of molecular electronics, electromigrated nanogaps have been widely used to create metal-molecule-metal junctions [183, 184].

6.6 Conclusions

In conclusion, we demonstrated how Al and Ni samples react differently to similar electromigration conditions. That is, instead of the voids and hillock formation seen in Al, we have gradual local annealing at the constriction of Ni due to Joule heating. The FEM findings of Ni suggested that the temperature at the constriction during electromigration is significantly high indicating that the temperature at the constriction is higher than the Curie temperature of Ni, implying that there is probably a phase transition from ferromagnetism to paramagnetism. We attribute this effect to the oxidation of the nickel layer, which was exposed to the air and/or the formation of a Ni-Cr alloy in their interface. It is worth mentioning that the affected region revealed in SEM examination is consistent in three other Ni devices electropulsed under the same conditions. Even though electromigration is a stochastic phenomenon, the findings obtained for Ni are remarkably consistent, as evidenced by the fact that an approximately similar current is required to

electromigrate all three devices to the desired state. These results open up the gate for further investigations into ferromagnetic materials using TEM, micro-Raman, EXAFS and other focused X-ray techniques to verify this hypothesis.

Chapter 7

Conclusions and perspectives

In the present work, we have demonstrated the potential of using high current densities to modify the properties of metals. The proposed approach of using electropulses complements the effective technique of controlled electromigration, which can be directly implemented with no need for expensive analog feedback systems or intricate software-controlled feedback loops.

Two study cases were dealt here, in the first case where this technique has been applied to Nb multiterminal transport bridges, we highlight the influence of the junctions geometry on the extension of the affected area. We demonstrated that the otherwise imperceptible structural changes can also be revealed by KPFM in addition to SEM in-lens detector. The study shed some light on the possible mechanisms leading to a reduction of the work-function. Additionally, a finite-element model based on the exact geometry of the experimentally investigated sample indicates that the affected area is hotter than 435 K.

The first of these findings is rather universal and should indeed apply to other materials. As for its use, it adds another knob to the control of junctions and weak links generated by electropulsing. In a nutshell, we have demonstrated that electropulsing can be used to modify the properties of targeted individual Nb junctions in a device with any number of terminals. This strategy is intriguing because of its simplicity, which enables nanofabrication without demanding overlay processing or additional deposition steps. A significant amount of selectivity is also seen: unaddressed junctions are left intact, and those that are targeted can be somewhat tuned by combining predefined geometries on purpose and/or by controlling the amplitude of the electropulsing current. Due to the current proliferation of Niobium-based superconducting devices, continuous progress in the development of Nb thin films for use in transmon qubit architectures, and the critical role

oxygen vacancies play in decoherence, this report provides timely information by revealing the serious consequences of applying moderate currents in these devices.

Our second study demonstrated that the application of current pulses resulted in structural modifications of Al and Ni microconstrictions. SEM images of Al after electropulsing demonstrated that voids had formed on the cathode side of the constriction. Additionally, hillocks were also formed at the end of the bridge and near certain voids. This portion of the bridge is very significant with respect to the temperature gradient. This is supported by the observation that the temperature rise is not uniform between the voltage contacts. SEM images of Ni, however, showed that an annealing effect is observed, which differs from the classical effect of EM, i.e., grain-boundary diffusion, stress gradients, and void formation. The EM process in Ni occurs in a fairly well defined area, as could be predicted considering the occurrence of current crowding and local heating. EM in Al, on the other hand, appears to occur more randomly, possibly due to less visible grain boundaries.

This paves the way for further research into different ferromagnetic materials and how electropulsing impacts domain walls and other magnetic properties. As far as we know, this technique is not available in any Brazilian institution, so that its implementation in Brazil will be innovative. GSM and UFSCar provide all of the necessary and favourable conditions for the implementation of the technique, which will be started in the very near future.

Bibliography

1. Yao, C. & Ma, Y. Superconducting materials: Challenges and opportunities for large-scale applications. *Iscience* **24,** 102541 (2021).

2. Bray, J. Superconducting applications: present and future. *Journal of superconductivity and novel magnetism* **21,** 335–341 (2008).

3. Onnes, H. K. research notebooks 56, 57. *Kamerlingh Onnes Archive, Boerhaave Museum, Leiden, the Netherlands* (1911).

4. Van Delft, D. *Freezing Physics: Hieke Kamerlingh Onnes and the Quest for Cold* (Koninklijke Nederlandse Akademie van Wetenschappen, 2007).

5. Meissner, W. & Ochsenfeld, R. Ein neuer effekt bei eintritt der supraleitfähigkeit. *Naturwissenschaften* **21,** 787–788 (1933).

6. Forrest, A. M. Meissner and Ochsenfeld revisited. *European Journal of Physics* **4,** 117 (1983).

7. London, F. & London, H. The electromagnetic equations of the supraconductor. *Proceedings of the Royal Society of London. Series A-Mathematical and Physical Sciences* **149,** 71–88 (1935).

8. Abrikosov, A. A. On the magnetic properties of superconductors of the second group. *Soviet Physics-JETP* **5,** 1174–1182 (1957).

9. Bardeen, J., Cooper, L. N. & Schrieffer, J. R. Theory of superconductivity. *Physical review* **108,** 1175 (1957).

10. Moshchalkov, V. V. & Fritzsche, J. *Nanostructured superconductors* (World Scientific, 2011).

11. Landau, L. D. & Ginzburg, V. On the theory of superconductivity. *Zh. Eksp. Teor. Fiz.* **20,** 1064 (1950).

12. Poole, C. P., Farach, H. A. & Creswick, R. J. *Superconductivity* (The Netherlands: Academic press, 2007).

13. Josephson, B. D. Possible new effects in superconductive tunnelling. *Physics letters* **1,** 251–253 (1962).

14. Anderson, P. W. & Rowell, J. M. Probable observation of the Josephson superconducting tunneling effect. *Physical Review Letters* **10,** 230 (1963).

15. Zimmerman, J. E. & Silver, A. Quantum effects in type II superconductors. *Phys. Letters* **10** (1964).

16. Anderson, P. & Dayem, A. Radio-frequency effects in superconducting thin film bridges. *Physical Review Letters* **13,** 195 (1964).

17. Clarke, J. Supercurrents in lead—copper—-lead sandwiches. *Proceedings of the Royal Society of London. Series A. Mathematical and Physical Sciences* **308,** 447–471 (1969).

18. Clarke, J. Finite-voltage behavior of lead-copper-lead junctions. *Physical Review B* **4,** 2963 (1971).

19. Gubankov, V., Koshelets, V. & Ovsyannikov, G. Coherent effects in superconducting bridges of variable thickness. *Sov. Phys. JEPT* **44,** 181–186 (1976).

20. Chaudhari, P. *et al.* Direct measurement of the superconducting properties of single grain boundaries in Y 1 Ba 2 Cu 3 O 7- δ. *Physical review letters* **60,** 1653 (1988).

21. Likharev, K. Superconducting weak links. *Reviews of Modern Physics* **51,** 101 (1979).

22. Giovanazzi, S., Smerzi, A. & Fantoni, S. Josephson effects in dilute Bose-Einstein condensates. *Physical review letters* **84,** 4521 (2000).

23. Davis, J. & Packard, R. Superfluid 3 He Josephson weak links. *Reviews of Modern Physics* **74,** 741 (2002).

24. Cataliotti, F. *et al.* Josephson junction arrays with Bose-Einstein condensates. *Science* **293,** 843–846 (2001).

25. Passos, W. *et al.* Granularity in superconductors: intrinsic properties and processing-dependent effects. *Physica C: Superconductivity* **354,** 189–196 (2001).

26. Feynman, R. P., Leighton, R. B. & Sands, M. *Lectures on physics, Volume III, quantum mechanics* 1965.

27. Owen, C. & Scalapino, D. Vortex structure and critical currents in Josephson junctions. *Physical Review* **164,** 538 (1967).

28. Lloyd, J. Electromigration for designers: An introduction for the non-specialist. *TechOnLine.* `https://www.eetimes.com/document.asp?doc_id=1275855` (Assesed on 19/12/2022).

29. Johnson, S., Sundararajan, A., Hunley, D. & Strachan, D. Memristive switching of single-component metallic nanowires. *Nanotechnology* **21,** 125204 (2010).

30. Naitoh, Y., Horikawa, M., Abe, H. & Shimizu, T. Resistance switch employing a simple metal nanogap junction. *Nanotechnology* **17,** 5669 (2006).

31. Lombardo, J. *et al.* Electromigration-induced resistance switching in indented Al microstrips. *New Journal of Physics* **21,** 113015 (2019).

32. Blanco Alvarez, S., Brisbois, J., Melinte, S., Kramer, R. B. & Silhanek, A. Statistics of thermomagnetic breakdown in Nb superconducting films. *Scientific reports* **9,** 1–9 (2019).

33. Gurunarayanan, S. P. *et al.* Electrically driven unidirectional optical nanoantennas. *Nano letters* **17,** 7433–7439 (2017).

34. Ilyas, A. *et al.* Electrical detection of cancer biomarker using aptamers with nanogap break-junctions. *Nanotechnology* **23,** 275502 (2012).

35. Liang, W., Shores, M. P., Bockrath, M., Long, J. R. & Park, H. Kondo resonance in a single-molecule transistor. *Nature* **417,** 725–729 (2002).

36. Esen, G. & Fuhrer, M. Temperature control of electromigration to form gold nanogap junctions. *Applied Physics Letters* **87,** 263101 (2005).

37. Strachan, D. *et al.* Controlled fabrication of nanogaps in ambient environment for molecular electronics. *Applied Physics Letters* **86,** 043109 (2005).

38. Trouwborst, M., Van Der Molen, S. & Van Wees, B. The role of Joule heating in the formation of nanogaps by electromigration. *Journal of Applied Physics* **99,** 114316 (2006).

39. Song, H. *et al.* Observation of molecular orbital gating. *Nature* **462,** 1039–1043 (2009).

40. Zharinov, V. S., Baumans, X. D., Silhanek, A. V., Janssens, E. & Van de Vondel, J. Controlled electromigration protocol revised. *Review of Scientific Instruments* **89,** 043904 (2018).

41. Wu, Z. M. *et al.* Feedback controlled electromigration in four-terminal nanojunctions. *Applied Physics Letters* **91,** 053118 (2007).

42. Heersche, H. B., Lientschnig, G., O'Neill, K., van der Zant, H. S. & Zandbergen, H. W. In situ imaging of electromigration-induced nanogap formation by transmission electron microscopy. *Applied Physics Letters* **91,** 072107 (2007).

43. Ho, P. S. & Kwok, T. Electromigration in metals. *Reports on Progress in Physics* **52,** 301 (1989).

44. Saka, M. *Metallic micro and nano materials: fabrication with atomic diffusion* (Springer Science & Business Media, 2011).

45. Lloyd, J. Electromigration in integrated circuit conductors. *Journal of Physics D: Applied Physics* **32,** R109 (1999).

46. Pierce, D. & Brusius, P. Electromigration: A review. *Microelectronics Reliability* **37,** 1053–1072 (1997).

47. Malone, D. & Hummel, R. Electromigration in integrated circuits. *Critical Reviews in Solid State and Material Sciences* **22,** 199–238 (1997).

48. Fiks, V. On the mechanism of the mobility of ions in metals. *Soviet Physics-Solid State* **1,** 14–28 (1959).

49. Huntington, H. & Grone, A. Current-induced marker motion in gold wires. *Journal of Physics and Chemistry of Solids* **20,** 76–87 (1961).

50. Bosvieux, C. & Friedel, J. Sur l'electrolyse des alliages metalliques. *Journal of Physics and Chemistry of Solids* **23,** 123–136 (1962).

51. Landauer, R. & Woo, J. W. Driving force in electromigration. *Physical Review B* **10,** 1266 (1974).

52. Sham, L. Microscopic theory of the driving force in electromigration. *Physical Review B* **12,** 3142 (1975).

53. Verbruggen, A. & Griessen, R. Experimental evidence for nonintegral direct-force valence in electromigration. *Physical Review B* **32,** 1426 (1985).

54. Sorbello, R. S. Theory of electromigration. *Solid state physics (New York. 1955)* **51,** 159–231 (1997).

55. Gupta, R. P., Serruys, Y., Brebec, G. & Adda, Y. Calculation of the effective valence for electromigration in niobium. *Physical Review B* **27,** 672 (1983).

56. Black, J. R. Electromigration failure modes in aluminum metallization for semiconductor devices. *Proceedings of the IEEE* **57,** 1587–1594 (1969).

57. Liew, B.-K., Cheung, N. W. & Hu, C. Projecting interconnect electromigration lifetime for arbitrary current waveforms. *IEEE Transactions on Electron Devices* **37,** 1343–1351 (1990).

58. Shatzkes, M. & Lloyd, J. A model for conductor failure considering diffusion concurrently with electromigration resulting in a current exponent of 2. *Journal of applied physics* **59,** 3890–3893 (1986).

59. Lloyd, J. & Kitchin, J. The electromigration failure distribution: The fine-line case. *Journal of applied physics* **69,** 2117–2127 (1991).

60. Kirchheim, R. & Kaeber, U. Atomistic and computer modeling of metallization failure of integrated circuits by electromigration. *Journal of applied physics* **70,** 172–181 (1991).

61. Korhonen, M., Bo/Rgesen, P., Tu, K.-N. & Li, C.-Y. Stress evolution due to electromigration in confined metal lines. *Journal of Applied Physics* **73,** 3790–3799 (1993).

62. Korhonen, 5. A., Bo/rgesen, P., Brown, D. & Li, C.-Y. Microstructure based statistical model of electromigration damage in confined line metallizations in the presence of thermally induced stresses. *Journal of applied physics* **74,** 4995–5004 (1993).

63. Lloyd, J. Reliability modelling for electromigration failure. *Quality and Reliability Engineering International* **10,** 303–308 (1994).

64. Oates, A. Current density dependence of electromigration failure of submicron width, multilayer Al alloy conductors. *Applied physics letters* **66,** 1475–1477 (1995).

65. Lombardo, J. Tailoring weak links by electromigration (2019).

66. Blech, I. & Herring, C. Stress generation by electromigration. *Applied Physics Letters* **29,** 131–133 (1976).

67. Blech, I. A. Electromigration in thin aluminum films on titanium nitride. *Journal of applied physics* **47,** 1203–1208 (1976).

68. Blech, I. & Meieran, E. Electromigration in thin Al films. *Journal of Applied Physics* **40,** 485–491 (1969).

69. Lloyd, J. Electromigration in thin film conductors. *Semiconductor science and technology* **12,** 1177 (1997).

70. Ye, H., Hopkins, D. C. & Basaran, C. Measurement of high electrical current density effects in solder joints. *Microelectronics Reliability* **43,** 2021–2029 (2003).

71. Jeong, W., Kim, K., Kim, Y., Lee, W. & Reddy, P. Characterization of nanoscale temperature fields during electromigration of nanowires. *Scientific Reports* **4,** 1–6 (2014).

72. Fangohr, H., Chernyshenko, D. S., Franchin, M., Fischbacher, T. & Meier, G. Joule heating in nanowires. *Physical Review B* **84,** 054437 (2011).

73. De Orio, R., Ceric, H. & Selberherr, S. Physically based models of electromigration: From Black's equation to modern TCAD models. *Microelectronics Reliability* **50,** 775–789 (2010).

74. Arzt, E. & Nix, W. D. A model for the effect of line width and mechanical strength on electromigration failure of interconnects with "near-bamboo" grain structures. *Journal of materials research* **6,** 731–736 (1991).

75. Dreyer, M., Fu, K. & Varker, C. An electromigration model that includes the effects of microstructure and temperature on mass transport. *Journal of applied physics* **73,** 4894–4902 (1993).

76. Cho, J. & Thompson, C. Grain size dependence of electromigration-induced failures in narrow interconnects. *Applied Physics Letters* **54,** 2577–2579 (1989).

77. Campbell, J. & Knobel, R. Feedback-controlled electromigration for the fabrication of point contacts. *Applied Physics Letters* **102,** 023105 (2013).

78. Xiang, C., Kim, J. Y. & Penner, R. M. Reconnectable sub-5 nm nanogaps in ultralong gold nanowires. *Nano letters* **9,** 2133–2138 (2009).

79. Lombardo, J. *et al.* In situ tailoring of superconducting junctions via electro-annealing. *Nanoscale* **10,** 1987–1996. ISSN: 20403372 (4 Jan. 2018).

80. Baumans, X. D. *et al.* Healing Effect of Controlled Anti-Electromigration on Conventional and High-Tc Superconducting Nanowires. *Small* **13,** 1700384 (2017).

81. Marinković, S. *et al.* Direct visualization of current-stimulated oxygen migration in YBa2Cu3O7- δ thin films. *ACS nano* **14,** 11765–11774 (2020).

82. Collienne, S. *et al.* Electrically-Driven Oxygen Vacancy Aggregation and Displacement in YBa2Cu3O7- δ Films. *Advanced Electronic Materials,* 2101290 (2022).

83. Elliott, D. *Microlithography: process technology for IC fabrication* (McGraw-Hill, Inc., 1986).

84. Stepanova, M. & Dew, S. *Nanofabrication: techniques and principles* (Springer Science & Business Media, 2011).

85. Vieu, C. *et al.* Electron beam lithography: resolution limits and applications. *Applied surface science* **164,** 111–117 (2000).

86. Martın, J., Nogues, J., Liu, K., Vicent, J. & Schuller, I. K. Ordered magnetic nanostructures: fabrication and properties. *Journal of magnetism and magnetic materials* **256,** 449–501 (2003).

87. Egerton, R. F. *et al. Physical principles of electron microscopy* (Springer, 2005).

88. Evertsson, J. & et al. The thickness of native oxides on aluminum alloys and single crystals. *Appl. Surf. Sci.* **349,** 826–832 (2015).

89. Zhang, J.-T., Wang, L., Lamont, D. N., Velankar, S. S. & Asher, S. A. Fabrication of large-area two-dimensional colloidal crystals. *Angewandte Chemie* **124,** 6221–6224 (2012).

90. Goldstein, J. I. *et al. Scanning electron microscopy and X-ray microanalysis* (Springer, 2017).

91. Nonnenmacher, M., o'Boyle, M. & Wickramasinghe, H. K. Kelvin probe force microscopy. *Applied physics letters* **58,** 2921–2923 (1991).

92. Padamsee, H., Knobloch, J. & Hays, T. *RF superconductivity for Accelerators* ISBN: 978-3-527-40842-9 (Wiley-VCH, 2008).

93. Bernard, P. *et al. Superconducting niobium sputter-coated copper cavities at 1500 Mhz* in (Aug. 1991).

94. Proch, D. *Reduction of multipacting in superconducting accelerator structures* in (eds McCarthy, J. & Whitney, R.) (Jan. 1979), N1–N17.

95. Lam, S. K. & Tilbrook, D. L. Development of a niobium nanosuperconducting quantum interference device for the detection of small spin populations. *Appl. Phys. Lett.* **82,** 1078. ISSN: 00036951 (7 Feb. 2003).

96. Kleiner, R., Koelle, D., Ludwig, F. & Clarke, J. Superconducting quantum interference devices: State of the art and applications. *Proc. IEEE* **92,** 1534–1548. ISSN: 00189219 (10 2004).

97. Mück, M., André, M. O., Clarke, J., Gail, J. & Heiden, C. Radio-frequency amplifier based on a niobium dc superconducting quantum interference device with microstrip input coupling. *Appl. Phys. Lett.* **72,** 2885–2887 (22 1998).

98. Bouchiat, V. *et al.* Josephson junctions and superconducting quantum interference devices made by local oxidation of niobium ultrathin films. *Appl. Phys. Lett.* **79,** 123. ISSN: 00036951 (1 July 2001).

99. Muller, C. J., Ruitenbeek, J. M. V. & Jongh, L. J. D. Experimental observation of the transition from weak link to tunnel junction. *Physica C* **191,** 485–504. ISSN: 0921-4534 (3-4 1992).

100. Oates, D. E. & Dionne, G. F. Magnetically tunable superconducting resonators and filters. *IEEE Trans. Appl. Supercond.* **9,** 4170–4175. ISSN: 10518223 (2 1999).

101. Attar, S. S., Setoodeh, S., Laforge, P. D., Bakri-Kassem, M. & Mansour, R. R. Low temperature superconducting tunable bandstop resonator and filter using superconducting RF MEMS varactors. *IEEE Trans. Appl. Supercond.* **24,** 150709. ISSN: 10518223 (4 2014).

102. Talisa, S. H. *et al.* Low- and high-temperature superconducting microwave filters. *IEEE Trans. Microw. Theory Tech.* **39,** 1448–1454. ISSN: 15579670 (9 1991).

103. Tanaka, M. *et al.* 100-GHz single-flux-quantum bit-serial adder based on 10-kA/cm^2 niobium process. *IEEE Trans. Appl. Supercond.* **21,** 792–796. ISSN: 10518223 (3 June 2011).

104. Reagor, M. *et al.* Quantum memory with millisecond coherence in circuit QED. *Phys. Rev. B* **94,** 014506. ISSN: 24699969 (July 2016).

105. Murthy, A. A. *et al.* Developing a chemical and structural understanding of the surface oxide in a niobium superconducting qubit. *ACS Nano* **16,** 17257–17262. ISSN: 1936-0851. https://pubs.acs.org/doi/10.1021/acsnano.2c07913 (10 Sept. 2022).

106. Hernandez, G. A. *et al.* Microwave performance of niobium/kapton superconducting flexible cables. *IEEE Trans. Appl. Supercond.* **27,** 1200104. ISSN: 10518223 (4 June 2017).

107. Gupta, V. *et al.* Thin-film Nb/Polyimide superconducting stripline flexible cables. *IEEE Trans Appl. Supercond.* **29,** 1501605. ISSN: 15582515 (5 Aug. 2019).

108. Tyagi, P. V. *et al.* Improving the work function of the niobium surface of SRF cavities by plasma processing. *Appl. Surf. Sci.* **369,** 29–35. ISSN: 01694332 (Apr. 2016).

109. Keijers, W. *et al.* Nano-SQUIDs with controllable weak links created: Via current-induced atom migration. *Nanoscale* **10,** 21475–21482. ISSN: 20403372 (45 Dec. 2018).

110. Collienne, S. *et al.* Nb-based nanoscale superconducting quantum interference devices tuned by electroannealing. *Phys. Rev. Appl.* **15,** 034016. ISSN: 23317019 (3 Mar. 2021).

111. Collienne, S., Majidi, D., Van de Vondel, J., Winkelmann, C. B. & Silhanek, A. V. Targeted modifications of monolithic multiterminal superconducting weak-links. *Nanoscale* **14,** 5425–5429 (2022).

112. Alvarez, S. B., Brisbois, J., Melinte, S., Kramer, R. B. & Silhanek, A. V. Statistics of thermomagnetic breakdown in Nb superconducting films. *Sci. Rep.* **9,** 3659. ISSN: 20452322 (Dec. 2019).

113. Canet-Ferrer, J., Coronado, E., Forment-Aliaga, A. & Pinilla-Cienfuegos, E. Correction of the tip convolution effects in the imaging of nanostructures studied through scanning force microscopy. *Nanotechnology* **25,** 395703. ISSN: 13616528 (Oct. 2014).

114. Hagedorn, F. B. & Hall, P. M. Right-angle bends in thin strip conductors. *J. Appl. Phys.* **34,** 128. ISSN: 00218979 (1 1963).

115. Kanaya, K. & Okayama, S. Penetration and energy-loss theory of electrons insolid targets. *J. Phys. D: Appl. Phys* **5,** 43 (1972).

116. Li, J., Hoekstra, B., Wang, Z.-B., Qiu, J. & Pu, Y.-K. Secondary electron emission influenced by oxidation on the aluminum surface: the roles of the chemisorbed oxygen and the oxide layer. *Plasma Sources Sci. Technol.* **27,** 044002 (2018).

117. Magkoev, T. T. & Vladimirov, G. G. Aluminium oxide ultrathin-film growth on the Mo(110) surface: a work-function study. *J. Phys.: Condens. Matter* **13,** L655–L661 (2001).

118. Grundner, M. & Halbritter, J. XPS and AES studies on oxide growth and oxide coatings on niobium. *J. Appl. Phys.* **51,** 397–405. ISSN: 00218979 (1 1980).

119. Halas, S. & Durakiewicz, T. Is work function a surface or a bulk property? *Vacuum* **85,** 486–488 (2010).

120. Wang, Q. G. & Shang, J. X. First-principles study on the incipient oxidization of Nb(110). *J. Phys. Cond. Mat.* **24,** 225005. ISSN: 09538984 (June 2012).

121. Morris, R. G. & Hust, J. G. Thermal conductivity measurements of silicon from 30° to 425° C. *Physical Review* **124,** 1426 (1961).

122. Williams, R., Butler, W., Graves, R. & Moore, J. Experimental and theoretical evaluation of the phonon thermal conductivity of niobium at intermediate temperatures. *Physical Review B* **28,** 6316 (1983).

123. Jeuregns, L. P. H., Sloof, W. G., Tichelaar, F. D. & Mittemeijer, E. J. Growth kinetics and mechanisms of aluminum-oxide films formed by thermal oxidation of aluminum. *J. Appl. Phys.* **92,** 1649 (2002).

124. Halbritter, J. On the oxidation and on the superconductivity of niobium*. *Appl. Phys. A* **43,** 1–28 (1987).

125. Ohnishi, K., Kimura, T. & Otani, Y. Improvement of superconductive properties of mesoscopic Nb wires by Ti passivation layers. *Appl. Phys. Express* **1,** 021701. ISSN: 18820778 (Feb. 2008).

126. Calado, V. E. *et al.* Ballistic Josephson junctions in edge-contacted graphene. *Nature nanotechnology* **10,** 761–764 (2015).

127. Chiodi, F. *et al.* Geometry-related magnetic interference patterns in long S N S Josephson junctions. *Physical Review B* **86,** 064510 (2012).

128. Heida, J., Van Wees, B., Klapwijk, T. & Borghs, G. Nonlocal supercurrent in mesoscopic Josephson junctions. *Physical Review B* **57,** R5618 (1998).

129. Sheehy, D. E. & Zagoskin, A. M. Theory of anomalous magnetic interference pattern in mesoscopic superconducting/normal/superconducting Josephson junctions. *Physical Review B* **68,** 144514 (2003).

130. Rosenberg, R., Mayadas, A. & Gupta, D. Grain boundary contributions to transport. *Surface Science* **31,** 566–585 (1972).

131. Peterson, N. Grain-boundary diffusion in metals. *International metals reviews* **28,** 65–91 (1983).

132. Sethian, J. A., Wilkening, J. & Borucki, L. Analysis of stress-driven grain boundary diffusion. Part I. *SIAM Journal on Applied Mathematics* **64,** 1839–1863 (2004).

133. Wilkening, J., Borucki, L. & Sethian, J. Analysis of stress-driven grain boundary diffusion. Part II: Degeneracy. *SIAM Journal on Applied Mathematics,* 1864–1886 (2004).

134. d'Heurle, F. & Ames, I. Electromigration in single-crystal aluminum films. *Applied Physics Letters* **16,** 80–81 (1970).

135. Li, Z., Bauer, C., Mahajan, S. & Milnes, A. Degradation and subsequent healing by electromigration in Al-1 wt% Si thin films. *Journal of applied physics* **72,** 1821–1832 (1992).

136. Hong, C.-F., Togo, M. & Hoh, K. Repair of electromigration-induced voids in aluminum interconnection by current reversal. *Japanese journal of applied physics* **32,** L624 (1993).

137. Tu, K.-N. Recent advances on electromigration in very-large-scale-integration of interconnects. *Journal of applied physics* **94,** 5451–5473 (2003).

138. Prinz, G. A. Magnetoelectronics. *Science* **282,** 1660–1663 (1998).

139. Schmid, G. & Chi, L. F. Metal clusters and colloids. *Advanced Materials* **10,** 515–526 (1998).

140. Cobden, D. H. Nanowires begin to shine. *Nature* **409,** 32–33 (2001).

141. Yamaguchi, A. *et al.* Effect of Joule heating in current-driven domain wall motion. *Applied Physics Letters* **86,** 012511 (2005).

142. Kläui, M. *et al.* Direct observation of domain-wall configurations transformed by spin currents. *Physical review letters* **95,** 026601 (2005).

143. Meier, G. *et al.* Direct imaging of stochastic domain-wall motion driven by nanosecond current pulses. *Physical review letters* **98,** 187202 (2007).

144. Campbell, D. & Hendry, B. The effect of composition on the temperature coefficient of resistance of NiCr films. *British Journal of Applied Physics* **16,** 1719 (1965).

145. Yamaguchi, A., Hirohata, A., Ono, T. & Miyajima, H. Temperature estimation in a ferromagnetic Fe–Ni nanowire involving a current-driven domain wall motion. *Journal of Physics: Condensed Matter* **24,** 024201 (2011).

146. Cao, L. *et al.* Grain structure analysis and effect on electromigration reliability in nanoscale Cu interconnects. *Applied Physics Letters* **102,** 131907 (2013).

147. Ho, P. & Howard, J. Grain-boundary solute electromigration in polycrystalline films. *Journal of Applied Physics* **45,** 3229–3233 (1974).

148. Boragno, C., De Mongeot, F. B., Felici, R. & Robinson, I. Critical thickness for the agglomeration of thin metal films. *Physical Review B* **79,** 155443 (2009).

149. Noh, H.-S. *et al.* Suppression of Ni agglomeration in PLD fabricated Ni-YSZ composite for surface modification of SOFC anode. *Journal of the European Ceramic Society* **30,** 3415–3423 (2010).

150. Zhao, F. *et al.* Thermal stability study of NiSi and NiSi2 thin films. *Microelectronic engineering* **71,** 104–111 (2004).

151. Crittenden Jr, E. & Hoffman, R. Thin films of ferromagnetic materials. *Reviews of Modern Physics* **25,** 310 (1953).

152. Chaudhuri, S., Pal, A. K. & Barua, A. Effects of agglomeration and magnetic boundary scattering on the electrical resistivity of nickel films. *Journal of Applied Physics* **46,** 3465–3467 (1975).

153. Fawcett, E. Spin-density-wave antiferromagnetism in chromium. *Reviews of Modern Physics* **60,** 209 (1988).

154. Coey, J. M. *Magnetism and magnetic materials* (Cambridge university press, 2010).

155. Hemmous, M. *et al.* Magnetic properties of evaporated Ni thin films: effect of substrates, thickness, and Cu underlayer. *Metallurgical and Materials Transactions A* **46,** 4143–4149 (2015).

156. Xu, J., Shao, T. & Jin, G. Effect of processing conditions on microstructure and electrical characteristics of Ni thin films. *Vacuum* **84,** 478–482 (2009).

157. De Los Santos Valladares, L. *et al.* Characterization of Ni thin films following thermal oxidation in air. *Journal of Vacuum Science & Technology B, Nanotechnology and Microelectronics: Materials, Processing, Measurement, and Phenomena* **32,** 051808 (2014).

158. Mohanty, P., Rath, C., Mallick, P., Biswal, R. & Mishra, N. UV–visible studies of nickel oxide thin film grown by thermal oxidation of nickel. *Physica B: Condensed Matter* **405,** 2711–2714 (2010).

159. Fueki, K. & Wagner, J. B. Studies of the Oxidation of Nickel in the Temperature Range of 900 to 1400 C. *Journal of the Electrochemical Society* **112,** 384 (1965).

160. Goebel, J. & Pettit, F. Na 2 SO 4-induced accelerated oxidation (hot corrosion) of nickel. *Metallurgical Transactions* **1,** 1943–1954 (1970).

161. Adler, D. & Feinleib, J. Electrical and optical properties of narrow-band materials. *Physical Review B* **2,** 3112 (1970).

162. Murarka, S., Anand, M. & Agarwala, R. Diffusion of chromium in nickel. *Journal of Applied Physics* **35,** 1339–1341 (1964).

163. Petley, V., Sathishkumar, S., Raman, K. T., Rao, G. M. & Chandrasekhar, U. Microstructural and mechanical characteristics of Ni–Cr thin films. *Materials Research Bulletin* **66,** 59–64 (2015).

164. Vinayak, S., Vyas, H. & Vankar, V. Microstructure and electrical characteristics of Ni–Cr thin films. *Thin Solid Films* **515,** 7109–7116 (2007).

165. Miller, C., Field, R. & Kaufman, M. Phase stability of γ-Ni2Cr and α-Cr in the Ni-Cr binary. *Acta Materialia* **157,** 1–10 (2018).

166. Ohgai, T., Tanaka, Y. & Fujimaru, T. Soft magnetic properties of Ni–Cr and Co–Cr alloy thin films electrodeposited from aqueous solutions containing trivalent chromium ions and glycine. *Journal of Applied Electrochemistry* **42,** 893–899 (2012).

167. Sulitanu, N. Structural origin of perpendicular magnetic anisotropy in Ni–W thin films. *Journal of magnetism and magnetic materials* **231,** 85–93 (2001).

168. Pryor, R. W. *Multiphysics modeling using COMSOL®: a first principles approach* (Jones & Bartlett Publishers, 2009).

169. Terada, Y., Ohkubo, K., Mohri, T. & Suzuki, T. Thermal conductivity in nickel solid solutions. *Journal of applied physics* **81,** 2263–2268 (1997).

170. Sun, L., Ling, X. & Li, X. Alternating-current induced thermal fatigue of gold interconnects with nanometer-scale thickness and width. *Review of Scientific Instruments* **82,** 103903 (2011).

171. Girod, S. *et al.* Real time atomic force microscopy imaging during nanogap formation by electromigration. *Nanotechnology* **23,** 365302 (2012).

172. Baumans, X. D. *et al.* Thermal and quantum depletion of superconductivity in narrow junctions created by controlled electromigration. *Nature communications* **7,** 1–8 (2016).

173. Huang, Q., Lilley, C. M. & Divan, R. An in situ investigation of electromigration in Cu nanowires. *Nanotechnology* **20,** 075706 (2009).

174. Suga, H. *et al.* Single-crystalline nanogap electrodes: Enhancing the nanowire-breakdown process with a gaseous environment. *ACS Applied Materials & Interfaces* **4,** 5542–5546 (2012).

175. Suga, H. *et al.* Feedback electromigration assisted by alternative voltage operation for the fabrication of facet-edge nanogap electrodes. *ACS Applied Nano Materials* **3,** 4077–4083 (2020).

176. Ueno, K. *et al.* Nanogap-assisted surface plasmon nanolithography. *The Journal of Physical Chemistry Letters* **1,** 657–662 (2010).

177. Chen, X. *et al.* Electrical nanogap devices for biosensing. *Materials Today* **13,** 28–41 (2010).

178. Chang, T.-L. *et al.* Ultrasensitive electrical detection of protein using nanogap electrodes and nanoparticle-based DNA amplification. *Biosensors and Bioelectronics* **22,** 3139–3145 (2007).

179. Quek, S. Y. *et al.* Mechanically controlled binary conductance switching of a single-molecule junction. *Nature nanotechnology* **4,** 230–234 (2009).

180. Kim, Y. *et al.* Conductance and vibrational states of single-molecule junctions controlled by mechanical stretching and material variation. *Physical review letters* **106,** 196804 (2011).

181. Song, H., Lee, H. & Lee, T. Intermolecular chain-to-chain tunneling in metal-alkanethiol- metal junctions. *Journal of the American Chemical Society* **129,** 3806–3807 (2007).

182. Dubois, V. *et al.* Massively parallel fabrication of crack-defined gold break junctions featuring sub-3 nm gaps for molecular devices. *Nature communications* **9,** 3433 (2018).

183. Song, H., Reed, M. A. & Lee, T. Single molecule electronic devices. *Advanced Materials* **23,** 1583–1608 (2011).

184. Gehring, P., Thijssen, J. M. & van der Zant, H. S. Single-molecule quantum-transport phenomena in break junctions. *Nature Reviews Physics* **1,** 381–396 (2019).

Appendix A

A.1 Modification of nanoholey Al films by electropulsing

The interaction of holes and electromigration may be utilized to alter atom positions, allowing for mass manufacturing of nanoscale structures. Classical electromigration generally results in atom buildup with protrusions at the anode and atomic depletion with voids at the cathode. We show that by using a nanoholey pattern, the depletion can be adjusted such that atomic accumulation occurs throughout the whole surface in the region of the holes rather than only at the anode. Figure A.1 illustrates the sample fabricated using a procedure discussed in subsection 4.3.3.

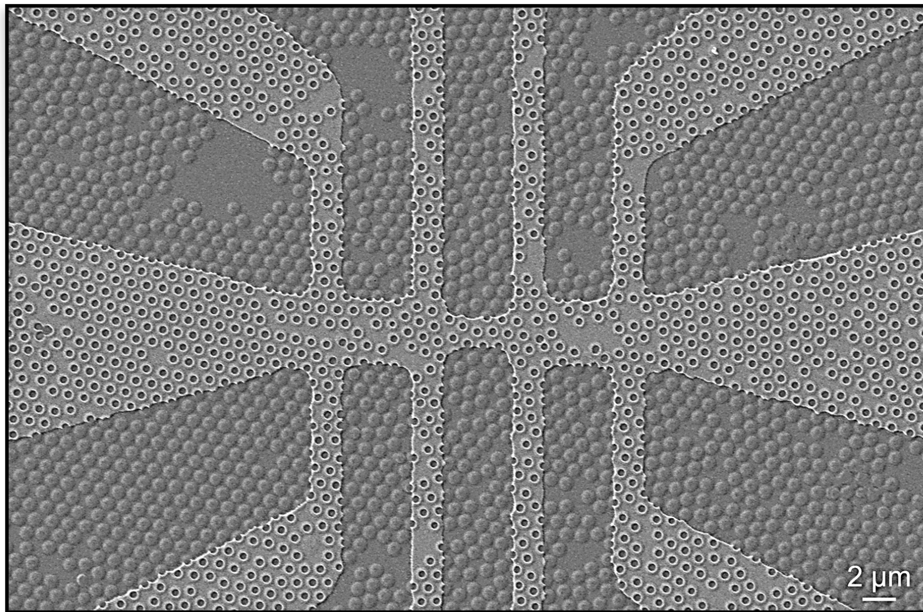

Figure A.1: SEM images of constrictions based on Nanoholey Al layer generated by photolithography and wet etching.

A.2 Post electropulsing

SEM images taken before and after EM reveal voids and hillocks, as shown in Figure A.2. In this scenario, it appears that the hillocks cluster around the holes rather than developing at the end of the bridge. This is most likely related to a certain temperature pattern, however this definitely requires additional investigation. Nonetheless, the voids

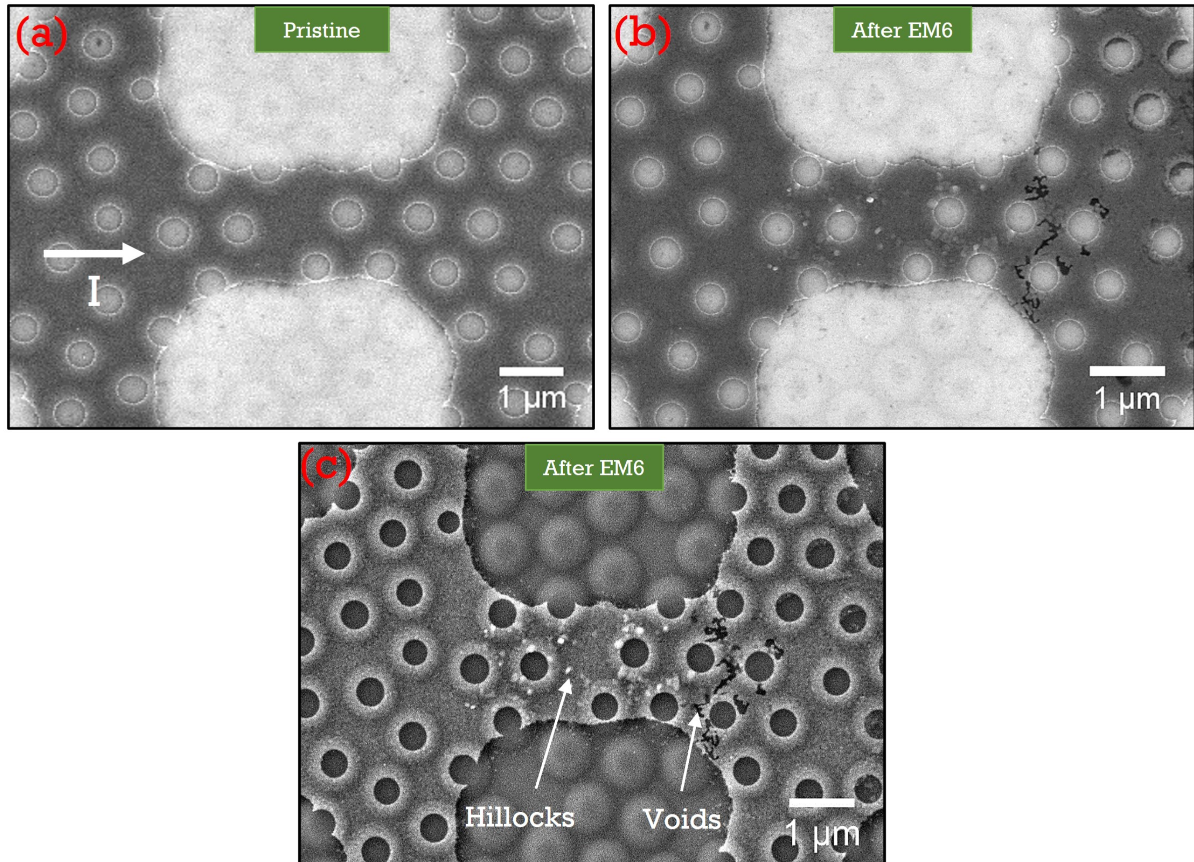

Figure A.2: SEM images of before (a) and after electromigration captured with inlens (b) and Everhart-Thonley (c) lens.

are visible on the cathode side of the constriction, with no preference as to where they were formed.

The evolution of the resistance as a function of the applied current is plotted in Figure A.3.

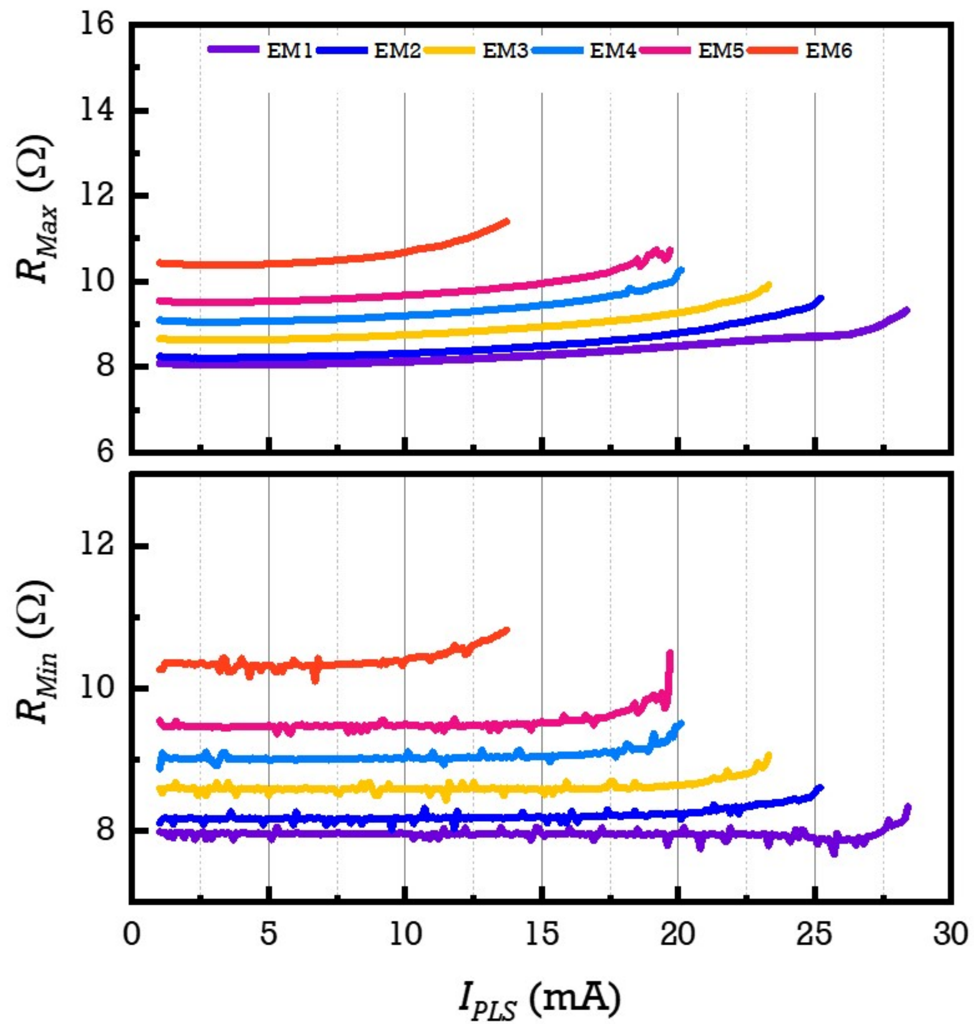

Figure A.3: The evolution of resistance as a function of current during the electromigration process is recorded for all EM runs.